Design and Development of Strong and Ductile Single BCC Refractory High-entropy Alloys for High-temperature Applications

A Dissertation Presented for the
Doctor of Philosophy
Degree
The University of Tennessee, Knoxville

Chanho Lee
August 2020

Copyright © 2020 by Chanho Lee.
All rights reserved.

ACKNOWLEDGEMENTS

I would like to pay sincere gratitude to all those who kindly helped and supported me greatly complete the Ph. D. in Department of Materials Science and Engineering at The University of Tennessee Knoxville. First of all, I would like to thank my advisor Prof. Peter. K Liaw for his excellent guidance on my scientific researches. I greatly appreciate to my committee members, Prof. Hahn Choo, Prof. Yanfei Gao, and Prof. Hairong Qi for their kind discussions, outstanding suggestions and thought-provoking guidance on my Ph. D studies. I am grateful to my master degree advisor Prof. Ki-Beum Kim for his infinite supports and guidance on my researches. I greatly appreciate the theoretical modeling of lattice distortion by DFT calculation from Prof. Wei Chen at Illinois Institute Technology. I'd like to thank Dr. Jonathan Poplawsky for helping me characterize the atomic distribution of HEAs by atom-probe tomography (APT) through the Center for Nanophase Materials Sciences (CNMS) program at the Oak Ridge National Laboratory (ORNL). The completion of this work would not be possible without the help from Dr. Ke An at the VULCAN, SNS, Oak Ridge National Laboratory (ORNL) for the in-situ neutron studies.

This research is supported by the U.S. Army Office Project (W911NF-13-1-0438 and W911NF-19-2-0049) with the program managers, Michael P. Bakas, David M. Stepp, and S. Mathaudhu, and the material was developed. Peter K. Liaw also thanks the support from the National Science Foundation (DMR-1611180 and 1809640) with the program director, Gary Shiflet and Diana Farkas, and the

neutron work was conducted. I would like to acknowledge the partial support from the Center of Materials Processing with Prof. Claudia Rawn as the director, a Tennessee Higher Education Commission (THEC) Center of Excellence located at The University of Tennessee, Knoxville. A portion of research at the ORNL's Spallation Neutron Source was sponsored by the Scientific User Facilities Division, Office of Basic Energy Sciences, U.S. Department of Energy. Reference herein to any specific commercial product, process, or service by the trade name, trademark, manufacturer, or otherwise, does not necessarily constitute or imply its endorsement, recommendation, or favoring by the United States Government or any agency thereof.

I appreciate the support of the US Department of Energy's Fossil Energy Cross-Cutting Technologies Program at the National Energy Technology Laboratory (NETL) under the RSS contract, 89243318CFE000003. Furthermore, the present work was supported by the National Research Foundation of Korea (NRF) grant funded by the Korea government (MSIT) (No. 2018R1C1B5083044).

Lastly and most importantly, I would like to dedicate my thesis to my parents, Dong-hwan Lee and Soo-yeon Kim, and my sister, Seoyun Lee, and my wife Seyi Oh, and my lovely daughters, Krystal Lee and Jessica Lee for their love, encouragement, and support in all my pursuits.

ABSTRACT

The objectives of this proposed study are to (1) design and develop single BCC phase refractory high-entropy alloys (HEAs) for the high-temperature applications, (2) investigate the deformation mechanisms of refractory HEAs, (3) improve an integrated approach, coupling focused experiments and theoretical modeling, to design, discover, and develop HEAs, and (4) understand the alloy design-microstructure-property-performance links underlying the mechanical behavior of refractory HEA systems for gas-turbine applications

A traditional alloy system generally includes one or two principal elements that form the matrix with other additional elements, e.g., iron or aluminum alloys, to strengthen some specific properties, such as strength and corrosion resistance. As a novel class of multicomponent materials, HEAs have recently stimulated the intensive study because of their large composition space and great properties. The definition of HEAs could be based on their chemical compositions or configurational entropy. According to their compositions, HEAs are typically composed of four or more principal elements in an equal or near-equal atomic percent between 5 to 35 atomic percent (at. %), which can crystallize as a single phase. According to their entropies, HEAs are defined as alloys that have configurational entropies larger or equal to 1.5R, where R is the ideal gas constant, no matter whether they are a single phase or multi-phases. A majority of HEAs reported so far have multiple phases (second phases, nanoparticles, element segregations and etc.), rather than a single solid-solution phase. However,

specially-designed HEAs can possess single-phase structures, such as body-centered-cubic (BCC), face-centered-cubic (FCC), and hexagonal-close-packed (HCP) structures These single-phase and multiple-phase HEAs have desirable materials properties, such as high strength, reasonable ductility, high hardness, good fatigue and corrosion resistance, high thermal conductivity, low coefficient of thermal expansion, and great toughness for gas turbines. Thus, it is of critical importance to develop a fundamental knowledge and understanding of the mechanical characteristics at elevated temperatures. The microstructure, and elastic/plastic deformation behavior of the refractory HEAs will be investigated, using the integrated experimental (transmission-electron microscopy/scanning-transmission-electron microscopy, in-situ neutron diffraction, and atom-probe tomography) and theoretical (first-principles calculations, and crystal-plasticity finite-element modeling) approaches.

TABLE OF CONTENTS

Chapter One Introduction....1
1.1 Objectives and Motivation....1
1.2 Framework....3
Chapter Two Background: Literature Reviews....6
2.1 Target Applications....6
2.2 High-entropy Alloys....8
2.3 Refractory High-entropy Alloys....14
2.4 Research Tasks....21
Chapter Three Lattice Distortion in a Strong and Ductile Refractory High-entropy Alloy....23
3.1 Introduction....23
3.2 Experimental Methods....25
3.2.1 Materials....25
3.2.2 Computational Methodologies....26
3.2.3 Microstructural Characterization....26
3.2.4 In-situ Neutron-diffraction Experiments....27
3.2.5 Mechanical Tests....28
3.2.6 First-principles Calculations....29
3.3 Results....29
3.3.1 Computational Prediction of Phase Formation and Evolution via CALPHAD Approach....29
3.3.2 Chemical Inhomogeneity in the As-cast Sample....32
3.3.3 Tailoring Single Phase with Homogeneous Chemistry via Thermal Treatment....37
3.3.4 Mechanical Properties at Room and Elevated Temperatures....40
3.4 Discussion....46
3.4.1 Homogenization-treatment Effects....46

3.4.2 Quantitative Measurement of Lattice Distortion via Experimental and Theoretical Calculations....48
3.4.3 Quantitative Measurement of Lattice Distortion via First-principles Calculation....56
3.4.4 Comparison of the Temperature Dependence of Yield Strengths....60
3.5 Conclusions....62
Chapter Four Temperature Dependence of Elastic and Plastic Deformation Behavior of a Ductile Refractory High-entropy Alloy....63
4.1 Introduction....63
4.2.1 Materials Preparation and Microstructural Characterization....66
4.2.2 In-situ Neutron Diffraction Experiments....67
4.2.3 First-principles Calculations....68
4.3 Results....69
4.3.1 Formation of the Single BCC Solid Solution and Its Mechanical Properties of the Homogenization-treated NbTaTiV HEA at Elevated Temperatures....69
4.3.2 Lattice-strain Evolutions of the Homogenized NbTaTiV HEA at Room and Elevated Temperatures....73
4.3.3 Quantitative Calculations of Single-crystal Elastic Moduli for NbTaTiV HEA via Kroner Model....78
4.3.4 Predictions of Elastic Moduli for the NbTaTiV Refractory HEA via First-principles Calculations....81
4.3.5 Plastic-deformation Behaviors of the NbTaTiV HEA at Elevated Temperatures....86
4.4 Discussion....89
4.4.1 Elastic Isotropy and Anisotropy Deformation Behaviors of the NbTaTiV Refractory HEA....89
4.4.2 Mechanical Stability and Ductility of the NbTaTiV Refractory HEA....93
4.4.3 Line-profile Modeling....94
4.5 Conclusion....103

Chapter Five Improvement of Lattice Distortion by Addition of Zr Element in NbTaTiV Refractory High-entropy Alloy 105
5.1 Introduction 105
5.2 Experimental Methods 106
5.2.1 Materials Preparations 106
5.2.2 CALPHAD Modeling 106
5.2.3 Synchrotron X-ray Diffractions 107
5.2.4 Scanning-electron Microscopy and Electron-backscatter Diffraction 107
5.2.5 Atom-Probe Tomography 108
5.2.6 Mechanical Tests 108
5.2.7 First-principles Calculations 109
5.2.8 Transmission-electron Microscopy 110
5.3 Results 111
5.3.1 Theoretical Prediction of Phase Formation for NbTaTiVZr HEA via CALPHAD Modeling 111
5.3.2 Phase and Microstructural Evolutions for NbTaTiVZr HEA via Systematic Thermal Treatment 114
5.3.3 Verification of Chemical Homogeneity for Homogenized NbTaTiVZr HEA 119
5.3.4 Comparison of the Mechanical Properties and Strengthening Mechanism between NbTaTiV and NbTaTiVZr HEAs 123
5.3.5 Predictions of Interatomic Distances Distribution for NbTaTiV and NbTaTiVZr HEAs via First-principles Calculations 127
5.4 Discussion 130
5.4.1 Selection of Additional Element to Induce the Severe Lattice Distortion 130
5.4.2 Comparison of Quantitatively Determined Average Lattice Distortion between NbTaTiV and NbTaTiVZr HEAs via Mathematical Calculation with Synchrotron and Neutron Diffractions 131

5.4.3 Visualization and Measurements of Average Lattice Distortion for NbTaTiV and NbTaTiVZr HEAs via HRTEM and STEM-HAADF Techniques 138
5.5 Conclusion 142
Chapter Six Conclusion 143
List of References 146
Vita 162

LIST OF TABLES

Table 3.1 SEM-EDS and APT compositions, and elemental distribution analyses of as-cast and homogenization-treated refractory NbTaTiV HEAs. Chemical composition (in atomic percent, at. %) of constitutive regions in as-cast and homogenized alloys, determined using the energy-dispersive spectroscopy (EDS) and atom-probe tomography (APT), respectively. The binomial distribution of the analyzed data in comparison to the binomial distribution of the theoretical data is provided by the parameters of χ^2 and μ for each element. 36

Table 3.2 The theoretical parameters (Å^3) of the six binary systems. A calculated volume before and after alloying for six binary systems, variation of volume, ΔV, and average of the volume difference, ΔV_{ij}, in the supercell. 54

Table 3.3 Theoretical calculations and experimental results of lattice distortions. Effective lattice constant $dieff$ of each element, lattice constant (d), and lattice-distortion parameter (μD) of theoretically-calculated results in comparison to the experimental data. Note that the experimental results are calculated, based on the chemical composition, which is obtained from the APT measurements and lattice constants that are obtained through neutron diffraction. 55

Table 4.1 The elastic moduli, E_{hkl}, of different crystallographic planes for the homogenized NbTaTiV alloy at elevated temperatures. Elastic moduli of {110}, {200}, {211}, and {310} at RT, 700 °C, and 900 °C are obtained from in-situ neutron diffractions. 77

Table 4.2 Single-crystal and macroscopic elastic constants of NbTaTiV alloy at elevated temperatures obtained from Kroner model based on in-situ neutron data (RT, 700 °C and 900 °C) and first-principles calculation (-273 °C and RT). The single-crystal elastic constants, C_{11}, C_{12}, C_{44}, macroscopic elastic (E_M), shear (G_M), bulk (K_M) moduli, and Poisson'

ratio (v) at RT, 700 °C, and 900 °C are obtained from the diffraction elastic moduli, using Kroner model and theoretical calculation. 80

Table 4.3 Elastic anisotropy factors (A_z, A_{VR} and VEC) and brittle-ductile criterion (B/G and Cauchy Pressure) for homogenized NbTaTiV alloy at RT, 700 °C and 900 °C. The calculated Zener anisotropy ratio, $A_z = [2C_{44} / (C_{11} – C_{12})]$, Vigot and Reuss bounds, $A_{VR} = (G_V – G_R) / (G_V + G_R)$, Valence electron concentration (VEC), Pugh ratio [bulk modulus (K) / shear modulus (G)], and Cauchy pressure ($C_{12} – C_{44}$) for homogenized NbTaTiV alloy at RT, 700 °C, and 900 °C. 92

Table 4.4 Substituting values ($Ch00$ and q) for the dislocation contrast factor ($Chkl$) to perform the modified Williamson-Hall plots at RT, 700 °C, and 900 °C. The $Ch00$ is obtained, using the ANIZC software, considering the single crystal elastic moduli (C_{11}, C_{12}, and C_{44}) at various temperatures, then q is mathematically calculated according to Eq. (4.15). 100

Table 4.5 R-squared coefficients, which is statistically obtained from the fitting of modified Williamson-Hall plots for the homogenized NbTaTiV alloy at various temperatures and macrostrains. The goodness of fitting of a modified Williamson-Hall plots with ≈ 0 %, 5 %, 10 % and 15 % macrostrain at RT, 700 °C, and 900 °C is quantitatively described by R-squared coefficients. The 100 % value of R-squared indicates a perfect fitting. 101

Table 4.6 The coefficient of the linear fitting in the modified Williamson-Hall plot for homogenized NbTaTiV alloy at elevated temperatures as a function of macrostrain. The second coefficient $\pi A2b2/2\rho$ of Modified Williamson-Hall plot with ≈ 0 %, 5 %, 10 % and 15 % macrostrain at RT, 700 °C, and 900 °C. 102

Table 5.1 SEM-EDS and APT compositions, and elemental distribution analyses of as-cast and homogenization-treated refractory NbTaTiVZr HEAs. Chemical composition (in atomic percent, at. %) of constitutive regions in as-cast and homogenized alloys, determined using the energy-

dispersive spectroscopy (EDS) and atom-probe tomography (APT), respectively. The binomial distribution of the analyzed data in comparison to the binomial distribution of the theoretical data is provided by the parameters of χ^2 and μ for each element. 118

Table 5.2 Theoretical calculations and experimental results of lattice distortions. Effective lattice constant ($dieff$) of each element, lattice constant (d) of theoretically-calculated results in comparison to the experimental data. Note that the experimental results are calculated, based on the chemical composition, which is obtained from the lattice constants that are obtained through synchrotron XRD, neutron diffraction, and HRTEM image 136

Table 5.3 The average lattice distortions for NbTaTiV and NbTaTiVZr alloys which are obtained from theoretical calculations, synchrotron diffractions, neutron diffractions, HRTEM image, and STEM-HAADF images. 137

LIST OF FIGURES

Figure 1.1 The framework of the present integrated experimental and modeling works. 5
Figure 2.1 (a) Schematic diagram of gas generators and turbines, (b) gas turbine, and (c) gas-turbine blades 7
Figure 2.2 The classifications of high-entropy alloys.....11
Figure 2.3 Yield strength of high-entropy alloys and superalloys at different temperatures.....12
Figure 2.4 A materials-systems chart showing the alloy design-microstructure-property-theoretical modeling-performance links. Experimental and theoretical techniques.....13
Figure 2.5 Compressive engineering stress–strain curves of NbMoTaW and VNbMoTaW HEAs at room temperature and high temperatures. 17
Figure 2.6 The temperature dependence of the specific yield-strength of the TaNbHfZrTi alloy in comparison with that for TaNbMoW, TaNbVMoW, and $CrCoCuFeNiAl_{0.5}$ alloys.....18
Figure 2.7 The engineering stress–strain compression curves of the $NbCrMo_{0.5}Ta_{0.5}TiZr$ alloy samples after HIP at 296 K, 1,073 K, 1,273 K, and 1,473 K. 19
Figure 2.8 SEM images of the fracture surface of a $NbCrMo_{0.5}Ta_{0.5}TiZr$ alloy samples after compression deformation at room temperature.....20
Figure 3.1 CALPHAD-calculation data for NbTaTiV. Calculated equilibrium phase mole fractions during solidification for Nb23.8Ta25.5Ti24.9V25.8. The inset shows the composition evolution of the BCC solid-solution phase during non-equilibrium solidification using the Scheil–Gulliver models. 31
Figure 3.2 Phase and microstructural characteristics of as-cast NbTaTiV, studied by SEM, ND, EBSD, and APT data. (a) The dendritic microstructure in SEM-BSE images of the as-cast NbTaTiV alloy (b) Neutron-diffraction patterns with the peaks indexed for a BCC structure (c) EBSD-phase

map of the as-cast NbTaTiV alloy (d) Concentration-depth profile of all alloying elements taken along the black arrow (top), three-dimensional atom maps of individual elements (middle) and frequent-distribution histograms (bottom), for the dendritic region, and (e) Interdendritic region in the as-cast NbTaTiV alloy. 35

Figure 3.3 Microstructural evolutions of the NbTaTiV alloy as a function of heat-treatment conditions, studied by SEM, ND, EBSD, and APT data. The SEM-BSE images of after-annealed samples at different temperatures and time periods: (a) 1,000 °C for 1 day, (b) 1,200 °C for 1 day, and (c) 1,200 °C for 3 days, (d) Neutron-diffraction patterns of the NbTaTiV alloy after the heat treatment at 1,200 °C for 3 days with the peaks indexed for a BCC structure. (e) EBSD-phase map of the homogenization-treated NbTaTiV alloy, and (f) A one-dimensional concentration-depth profile of all alloying elements taken along the black arrow for the homogenization-treated NbTaTiV alloy (top). Three-dimensional atom maps of individual elements (bottom) (g) FDA of constituent elements with a block size of 100 atoms for the homogenized NbTaTiV alloy. 39

Figure 3.4 Comparison of mechanical properties and in-situ neutron-diffraction data of the as-cast and homogenization-treated NbTaTiV. (a) Engineering compressive stress-strain curves of the as-cast and homogenization-treated NbTaTiV at room temperature. Evolution of lattice strains for (b) [110] (c) [200] oriented planes in as-cast (black line) and homogenization-treated (red line) alloys as a function of applied stress. Evolution of normalized peak widths as a function of macro-strain for (d) As-cast, and (e) Homogenization-treated NbTaTiV HEAs. 43

Figure 3.5 SEM and EBSD images of the deformed lateral surface. (a) SEM micrograph of the homogenization-treated alloy after 15 % deformation. (b and c) The EBSD phase and inverse pole-figure mapping images of

the 15 %-deformed homogenized NbTaTiV at room temperature. The SEM micrograph of the 15 %-deformed homogenized sample shows a large density of slip bands that were nonuniformly oriented within different grains formed during plastic deformation. Furthermore, no strain-induced phase transformation was found to occur during compression testing, i.e., the single BCC solid-solution phase is observed on the phase map, and other deformation bands, such as local twin bands, were not observed from EBSD analyses. 44

Figure 3.6 Mechanical properties for NbTaTiV at elevated temperatures. Compressive engineering stress-strain curves and a summary of compression-yield strength (σ_y) for the homogenization-treated NbTaTiV alloy obtained at room temperature, 300 °C, 500 °C, 700 °C, 800 °C, and 900 °C, respectively. 45

Figure 3.7 First-principles calculation data. (a) Distribution of the interatomic distances for the first to fifth nearest neighbors (NN) of the BCC NbTaTiV HEA calculated from the optimized SQS. The blue dashed lines show the average interatomic distances for the first to fifth NNs, and (b) Box plot presenting the distribution of interatomic distances of 1NN bonds in the SQS for the BCC NbTaTiV HEA. The box presents the first and third quartiles of the bond lengths for a type of atomic bonds. (c) Two different locally-relaxed atomic structures of the BCC NbTaTiV HEA. The shortest and longest bond lengths of the Nb-Nb and V-V pairs for the first nearest neighbors in the supercells with the SQS model. 59

Figure 3.8 Comparison of the temperature dependence of yield strengths. Yield strengths of the NbTaTiV alloy and two reported refractory HEAs (MoNbTaW and MoNbTaVW), conventional HEA ($Al_{2.0}$CoCrCuFeNi), Al-based alloy (6061 Al alloy), Ti-based alloy (Ti-6Al-4V alloy), and Ni-based superalloys (Inconel 718 and Haynes 230) as a function of temperature. 61

Figure 4.1 Microstructural, phase characteristics, and mechanical properties of the homogenized NbTaTiV alloy, studied by SEM, neutron diffraction (ND), and nominal compressive true strain-stress curves during in-situ ND experiments at elevated temperatures. (a) SEM-BSE image of the homogenization-treated NbTaTiV refractory HEA. (b) neutron-diffraction patterns with the peaks indexed for a BCC structure at RT, 700 °C, and 900 °C, respectively. (c) True stress-strain curves recorded during in-situ compression experiment at RT, 700 °C, and 900 °C with a strain rate of 1×10^{-4} s^{-1}.....72

Figure 4.2 Lattice-strain evolution in the NbTaTiV refractory HEA as a function of applied stress, obtained from the in-situ ND experiments at RT. The corresponding lattice-strains of {110}, {200}, {211}, and {310} orientation planes along the axial and transverse direction at RT as a function of applied stress during the elastic and plastic deformations. The onset of yielding is marked as the green dot line.....74

Figure 4.3 Lattice-strain evolution in the NbTaTiV refractory HEA as a function of applied stress, obtained from the in-situ ND experiments during elastic deformation and plots of elastic moduli of different oriented crystals as a function of the elastic-anisotropy factor and fitting with the Kroner model at RT, 700 °C, and 900 °C. The corresponding lattice-strains of {110}, {200}, {211}, and {310} orientation planes along the axial and transverse direction during the elastic deformation (a) RT, (b) 700 °C, and (c) 900 °C, respectively. The reciprocal diffraction elastic moduli, ($1/E_{hkl}$ and v_{hkl}/E_{hkl}), as a function of the elastic-anisotropy factor, A_{hkl}, ($h2k2 + k2l2 + l2h2h2 + k2 + l22$), which are obtained from the experimental elastic lattice-strain (symbols) and fitted by Kroner models (solid lines) at (d) RT, (e) 700 °C, and (f) 900 °C, respectively.....76

Figure 4.4 Directional dependence of first-principles calculated RT elastic properties. The magnitude with respect to direction in three dimensions for (a) Young's modulus in GPa, (b) linear compressibility in TPa^{-1}, (c)

shear modulus in GPa, and (d) Poisson's ratio respectively. Shear modulus and Poisson's ratio is represented by two surfaces for maximum and minimum values. The magnitude with respect to direction on the XY, XZ, YZ planes for (e) Young's modulus in GPa, (f) linear compressibility in TPa^{-1}, (g) shear modulus in GPa, and (h) Poisson's ratio respectively. Shear modulus and Poisson's ratio is represented by two lines for maximum and minimum values. 85

Figure 4.5 Evolution of normalized full width at half maximum ($FWHM/FWHM_0$) as a function of macrostrain for homogenized NbTaTiV alloy, obtained from in-situ neutron experiment at elevated temperatures. The evolutions of the normalized Full width at half maximum ($FWHM/FWHM_0$) of {110}, {200}, {211}, and {310} diffraction peaks as a function of macrostrain at (a) RT, (b) 700 °C, and (c) 900 °C, respectively.....88

Figure 4.6 Neutron diffraction pattern line-profile modeling for the homogenized NbTaTiV alloy during plastic deformation, using the modified Williamson-Hall plot at elevated temperatures. The peak broadening analysis, $\Delta K2$ as a function of $K2C$, for the sample compressed from 0 % to 15 %, considering the dominant type of dislocation as a pure (a) <111> screw dislocation at RT, (b) <111> {110} edge dislocation at RT, (c) <111> {110} edge dislocation at 700 °C, and (d) <111> {110} edge dislocation at 900 °C, respectively.....99

Figure 5.1 CALPHAD-calculation data for NbTaTiVZr. Calculated equilibrium phase mole fractions during solidification for $Nb_{19.8}Ta_{18.3}Ti_{20.8}V_{19.8}Zr_{20.7}$. The inset shows the composition evolution of the BCC solid-solution phase during non-equilibrium solidification using the Scheil–Gulliver models. 113

Figure 5.2 Phase and microstructural characteristics of as-cast and heat-treated NbTaTiVZr, studied by SEM, synchrotron XRD, and EBSD. The SEM-BSE images and synchrotron XRD patterns for as-cast and after-

annealed samples at different temperatures and time periods: (a) (b) as-cast, (c) (d) 1,000 °C for 1 day, and (e) (f) 1,200 °C for 12 hours, EBSD-phase map of the (g) as-cast and (h) homogenization-treated NbTaTiVZr alloy.....117

Figure 5.3 Atomic-scale elemental distribution of as-cast and homogenized NbTaTiVZr alloys alloy (a) Concentration-depth profile of all alloying elements taken along the black arrow (top), three-dimensional atom maps of individual elements (middle) and frequent-distribution histograms (bottom), for the dendritic region, Interdendritic region in the as-cast and (b) homogenized NbTaTiVZr alloy. The frequency-distribution histograms of constituent elements were calculated with a block size of 100 atoms with the solid lines showing the binomial-distribution curves, and the dots are the observed experimental results. 122

Figure 5.4 Comparison of mechanical properties of the as-cast and homogenization-treated NbTaTiV and NbTaTiVZr. Engineering compressive stress-strain curves of the as-cast and homogenization-treated NbTaTiV and NbTaTiVZr alloys at room temperature 126

Figure 5.5 First-principles calculation data. (a) Distribution of the interatomic distances for the first to fifth nearest neighbors (NN) of the BCC NbTaTiV and NbTaTiVZr alloys calculated from the optimized SQS. The blue dashed lines show the average interatomic distances for the first to fifth NNs, and (b) Box plot presenting the distribution of interatomic distances of 1NN bonds in the SQS for the BCC NbTaTiV and NbTaTiVZr alloys. The box presents the first and third quartiles of the bond lengths for a type of atomic bonds. The whisker extends to either the 1.5 interquartile ranges or the maximum and minimum values. The median and mean for each type of atomic bonds exhibit as the green solid line and red dashed line, respectively. The reference bond lengths, calculated from comparable BCC structures for the

homoatomic pairs and B2 structures for the heteroatomic pairs, are shown in blue squares. 129
Figure 5.6 Schematic description of (a) perfect BCC crystal structure and (b) HEA crystal structure, showing detailed process of mathematic calculation of lattice distortion. 135
Figure 5.7 (a) (b) the HRTEM image and Fourier transformation of NbTaTiV and NbTaTiVZr alloys. It shows that NbTaTiV is of BCC structure and the lattice constant is 3.278 Å. (c) (d) the high magnitude HRTEM image for NbTaTiV and NbTaTiVZr, calculating the interatomic distances (e) (f) the HAADF images of NbTaTiV with $[110]$ zone axis and NbTaTiVZr with $[001]$ zone axis. (g) (h) the 2D Gauss fitted images of (e) (f). It provides the atomic position on HAADF of NbTaTiV NbTaTiVZr alloys. 141

CHAPTER ONE

INTRODUCTION

1.1 Objectives and Motivation

The main objectives of this study are to (1) design and explore the new body-centered-cubic (BCC) refractory HEAs; (2) study of lattice distortions; (3) investigate the elastic/plastic deformation behaviors in the temperature range of 25 ~ 900 °C; (4) understand the effect of additional element on the mechanical properties, which is induced by severe distorted lattice; (5) obtain an in-depth understanding of mechanical mechanisms of single body-centered-cubic (BCC) solid-solution refractory HEAs, thus providing an the crucial insight into the design of single-phase solid-solution refractory HEAs and their use in high-temperature applications, such as thermal-protection systems and gas-turbine engines.

The motivations of this proposed study are to (1) design and develop single BCC phase refractory high-entropy alloys (HEAs) for the high temperature applications, (2) investigate the deformation mechanisms of refractory HEAs, (3) improve an integrated approach, coupling focused experiments and theoretical modeling, to design, discover, and develop HEAs, and (4) understand the alloy design-microstructure-property-performance links underlying the mechanical behavior of refractory HEA systems for gas-turbine applications.

The novel metallic alloys beyond Ni-based superalloys with high strengths, thermal stabilities, and large ductility at high temperatures are highly desirable in the

aviation and aerospace industries. To meet the increasing demand of elevated-temperature alloys, exotic multi-principal-element metallic alloy systems, also referred to as high-entropy alloys (HEAs), have been proposed and studied due to their simple microstructures and promising properties. The ideal HEA design strategy is to form a single solid-solution phase via maximizing the configurational entropy (> 1.5R, where R is the ideal gas constant) [1-7]. The reduction of the Gibbs free energy by the high configurational entropy leads to the formation of the simple solid-solution phase, such as face-centered-cubic (FCC) [8], BCC [9-12], and hexagonal close-packed (HCP) [13, 14] structures. These features, in turn, contribute to attractive materials properties, especially, high hardness/strengths, and excellent softening resistance at elevated and cryogenic temperatures [3-5]. The exceptional properties of the near-equimolar HEAs are known to be associated with the locally-strained atomic structures (lattice distortion) in the simple-single solid-solution phase. Moreover, the recently-developed twinning or transformation-induced plasticity (TWIP or TRIP) HEAs, whose composition is greatly deviated from the near-equimolar ratios, have also attracted the increasing attention due to their excellent mechanical properties [15-20].

There have been extensive efforts to develop single-phase refractory HEAs for high-temperature applications above 1,100 °C [21-23] and to comprehend the underlying relationship between the unique microstructure and mechanical performance. However, limited studies have also investigated the lattice distortions in HEAs, using x-ray or neutron diffraction [24-26]. Furthermore, the quantitative

evaluation of the lattice distortion, through statistical calculations with experimental observations, is still not fully developed. Moreover, only a small number of alloy systems have been verified as single BCC solid-solution phases from experiments [27, 28]. For instance, many HEAs exhibit not only elemental segregations in the as-cast condition, but also the formation of small amounts of ordered phases after the heat treatment [29-31]. The chemical inhomogeneity and second-phase formation could hinder the fundamental and in-depth understanding of the main strengthening effect of HEAs. Therefore, the development of single solid-solution phase HEAs with homogeneous elemental distributions is vital to elucidate how lattice distortions affect mechanical properties.

The hypotheses propose that refractory HEAs with optimal compositions and microstructures will demonstrate superior mechanical properties over traditional alloys due to the: (1) formation of the single BCC solid-solution phase with systematic heat treatment, (2) simultaneous substitutional and interstitial solid-solution strengthening, (3) differences in the atomic sizes and shear moduli of composing elements, constituting the main contributions to solid-solution strengthening, and (4) optimization of distorted lattice to enhance the solid-solution hardening effects on mechanical properties.

1.2 Framework

Figure 1.1 shows an integrated theoretical and experimental framework for the proposed research. The proposed endeavors will focus on the design of new HEAs, microstructural evolutions and mechanical behaviors of refractory HEAs

with verification of lattice distortions. Fundamental studies will be performed, including (1) alloy design and property modulation, (2) microstructural characterizations, (3) modeling and analysis, and (4) elastic/plastic deformation behaviors. A systematic investigation of the mechanical properties, which are developed by severe lattice distortions, with the characterization of microstructural evolution, using the integrated experimental (scanning-electron microscopy, energy dispersive spectroscopy, electron backscatter diffraction, scanning-transmission-electron microscopy, in-situ neutron diffraction, and atom-probe tomography) and theoretical (first-principles calculations and finite-element modeling) approaches will be conducted to obtain in-depth understanding of the deformation mechanisms of significantly solid-solution strengthened refractory HEAs.

The present study mainly focuses on the following aspects, i.e., (1) exploration and design new BCC refractory HEAs, (2) measurements of lattice distortions for BCC refractory HEAs, and (3) investigation on elastic/plastic deformation behaviors of BCC refractory HEAs.

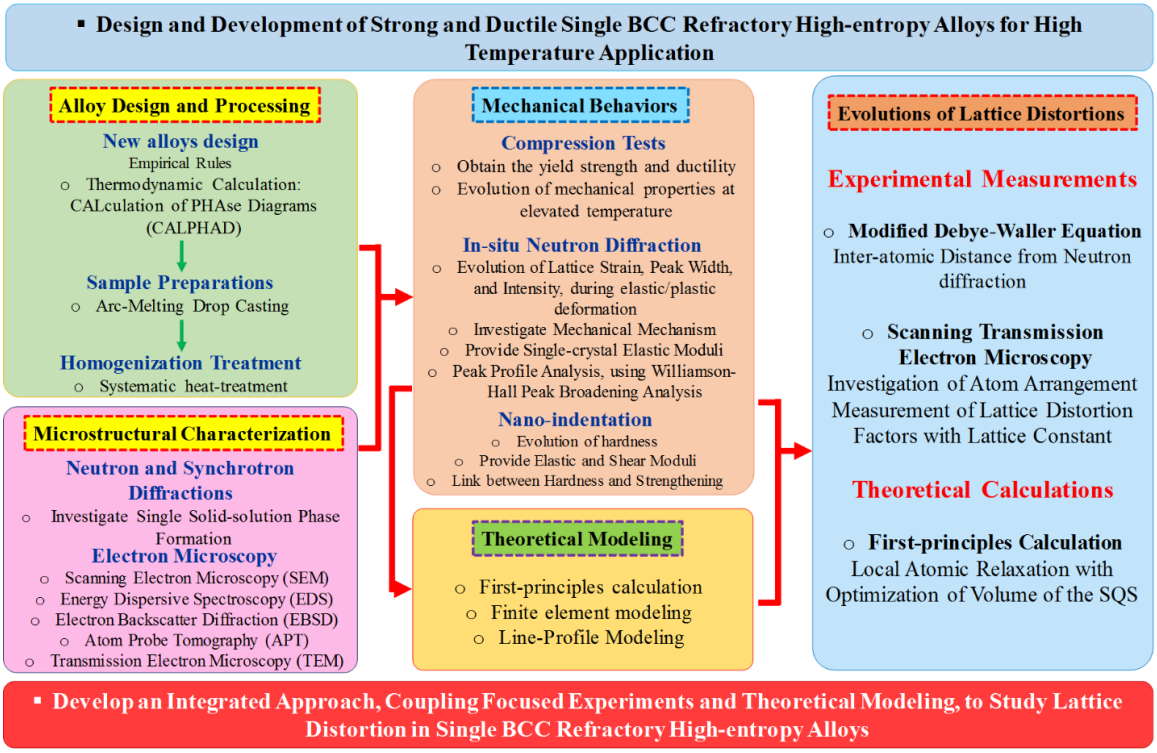

Figure 1.1 The framework of the present integrated experimental and modeling works.

CHAPTER TWO

BACKGROUND: LITERATURE REVIEWS

2.1 Target Applications

In advanced gas generators and turbines, the compressed air is heated in the combustor and then passes through the turbine [shown in Figure 2.1(a)], which means that the turbine blades [Figure 2.1(c)] have to possess the capability for withstanding both high temperatures and high stresses. During the whole process, the air is drawn from outside of the engine and finally exhausted as a high speed [Figure 2.1(b)].

To obtain great combined cycle-energy efficiency, it is needed for turbine components to achieve higher operating temperatures. Hence, it becomes critical to improve the properties of materials, which are used in gas-turbine components, including mechanical properties, thermal conductivity, corrosion resistance, and oxidation resistance, to improve the performance of gas turbines. The proposed research mainly focuses on investigating advanced alloys with great mechanical properties (i.e., tension strength, creep and fatigue resistance) at elevated temperatures. The turbine inlet temperature may exceed 1,700 °C to achieve higher energy efficiency, and some of the critical metals in the turbine have to withstand temperatures as hot as 700 to 900 °C. Thus, the temperatures chosen to be used in the mechanical experiments for the proposed research are 700, 900, and 1,100 °C.

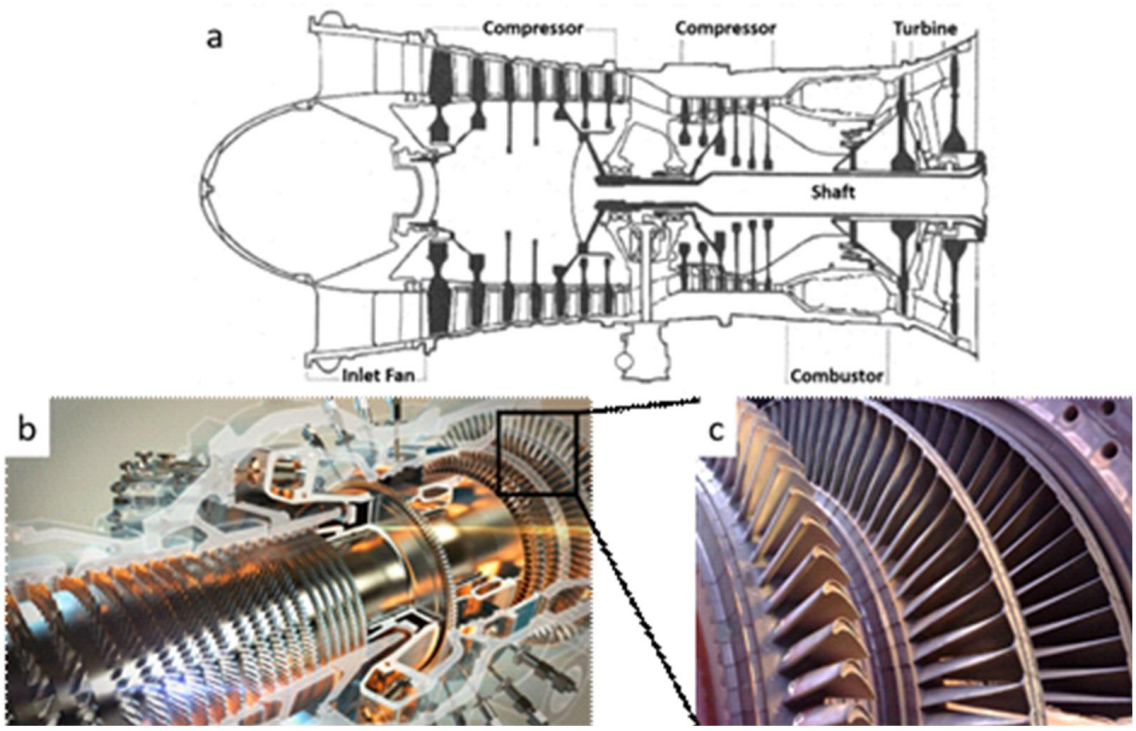

Figure 2.1 (a) Schematic diagram of gas generators and turbines, (b) gas turbine, and (c) gas-turbine blades

2.2 High-entropy Alloys

Nickel-based superalloys are widely used in many turbine components, including Haynes 230, Hastelloy X, Inconel Alloy 600, Inconel 718, etc. To achieve a higher energy efficiency, critical materials used in turbines should withstand high temperatures as mentioned above, while some gas-turbine alloys may not fit the criterion really well. The HEAs are novel alloys that have great mechanical properties, and some of them may also have good behavior (e.g., high yield strength and ductility) at elevated temperatures. Thus, HEAs will be designed and studied in the proposed research. HEAs can be divided into 4 types, which can be seen in Figure 2.2. Type-1 HEAs include 3d-transition metals [5, 8, 28]. Type-2 are transition metals with larger-atomic-radius elements, such as Al, Ti, V, and Mo [2, 22, 32-34]. The third type of HEAs are based on refractory metals [9-11]. The last Type are some other HEA systems. Among these HEA types, some alloys, such as refractory HEAs, have good mechanical performance at high temperatures, and can be considered for turbine applications. Figure 2.3 shows the yield strength of most-studied HEAs, conventional superalloys, and some representative refractory HEAs at different temperatures [10, 11, 22, 35]. The Type-1 HEAs are alloys with the single FCC solid-solution phase (Figure 2.2). This kind of HEAs show relatively-low yield strength but remarkable ductility, compared to Types-2 and 3. When the elements with large radii are introduced, such as Al, the Type-2 HEAs have higher yield stresses than Type 1, which is the result of the solid-solution strengthening mechanisms, dislocation strengthening, and other related effects

[36]. It can be easily seen that the Type-3 refractory HEAs dominate the realm of better mechanical properties at elevated temperatures from approximately 900 to 1,600 C. The yield stresses of refractory HEAs decrease relatively slow when the temperature increases.

Refractory HEAs exhibit high strengths at elevated temperatures mainly because of their configurational entropy and the melting temperatures of constituent elements. These refractory HEAs may have the potential to have better performance than Ni-based superalloys in turbine components. According to literature studies and preliminary results [10, 11, 37], three refractory HEA systems, VNbMoTaW, TaNbHfZrTi, and NbTaTiV, will be considered as candidates in the proposed research. As shown in Figure 2.3, among these refractory HEA candidates, VNbMoTaW has the relatively-high yield strength at elevated temperatures [10], TaNbHfZrTi is much lighter than VNbMoTaW, and NbTaTiV has the lower yield strength but is more ductile at elevated temperatures [28]. They may have different behavior in tension, creep, and fatigue for gas-turbine applications. Thus, their deformation mechanisms and microstructural evolution during tension, creep, and fatigue experiments will be examined for turbine applications in the proposed research.

The development and investigation of refractory HEA systems involve the integration of the focused experiments and theoretical modeling to build the relationship among the processing, microstructure, property, and performance.

Figure 2.4 shows a materials-systems chart describing the alloy design-microstructure-property-theoretical modeling-performance links for the refractory HEA systems. The experimental and computational techniques are listed under each sections of this figure. The relationship among alloy design, structures, and properties will be studied for gas-turbine applications in the proposed research. To optimize the performance of materials, efforts from different aspects, including alloy design, structures, and properties will be made. Throughout the optimization process of the performance of refractory HEAs for turbine applications at elevated temperatures, the integrated approach, coupling experiments and theory, will be developed.

The proposed research focuses on the investigation of mechanical properties of refractory HEAs at elevated temperatures. The program will closely couple experimental studies with theoretical modeling for the goals of (1) performing fundamental studies on refractory HEA systems for use in high temperatures applications, (2) investigating the related deformation mechanisms of refractory HEAs, and (3) studying the alloy design-microstructure-property-performance links underlying the mechanical behavior of refractory HEAs for turbine applications.

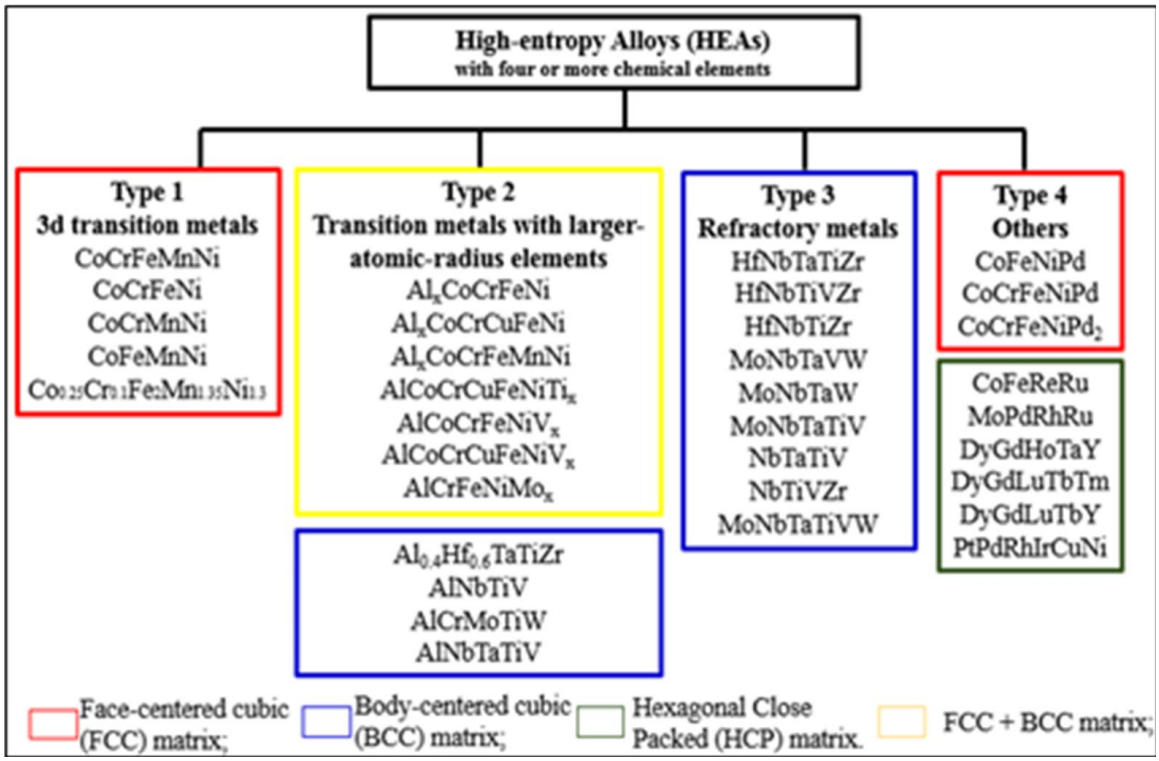

Figure 2.2 The classifications of high-entropy alloys.

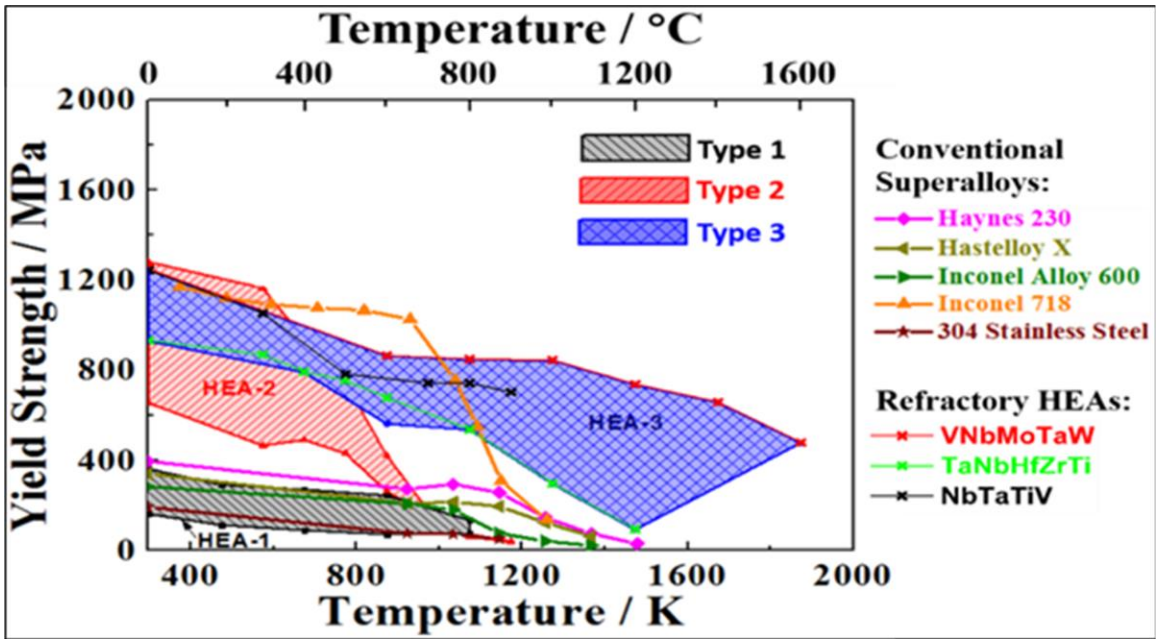

Figure 2.3 Yield strength of high-entropy alloys and superalloys at different temperatures.

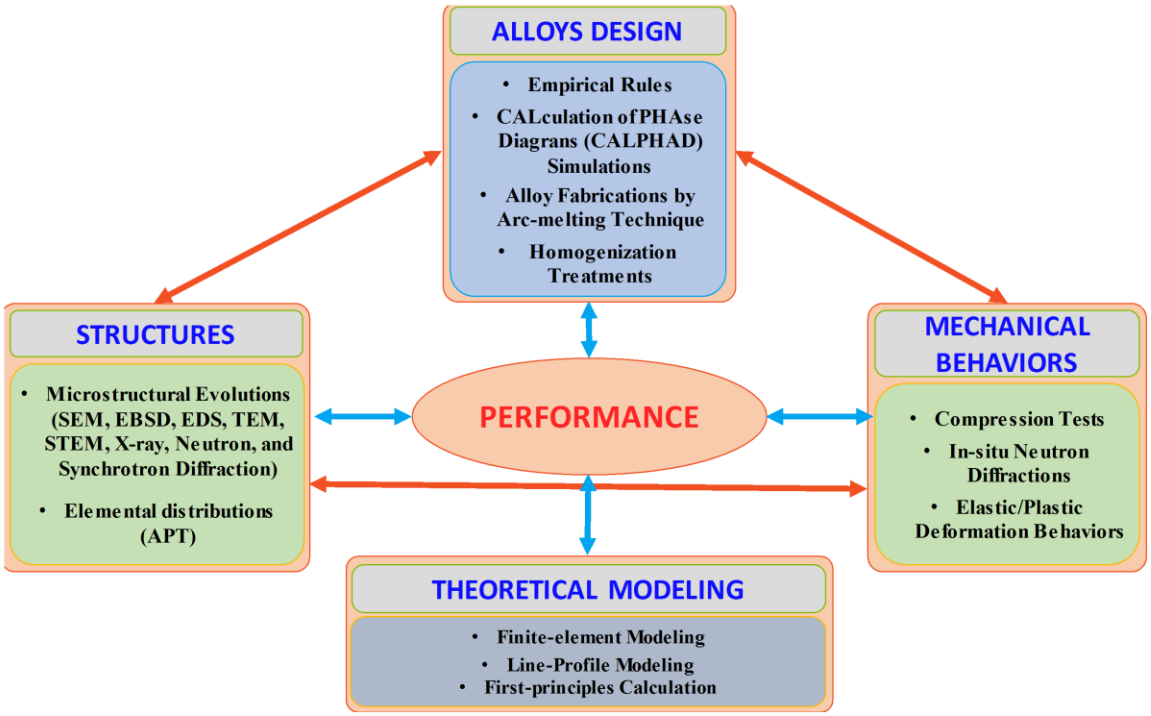

Figure 2.4 A materials-systems chart showing the alloy design-microstructure-property-theoretical modeling-performance links. Experimental and theoretical techniques.

2.3 Refractory High-entropy Alloys

Currently, Ni-based superalloys already show the excellent combination of mechanical properties at elevated temperature, including creep resistance, damage tolerance, and corrosion resistance. However, operating temperatures are reaching the theoretical limits of these materials.

The new alloy design strategy, high entropy alloying, was used to develop new refractory alloys, which contain several principal alloying refractory elements at near equiatomic concentrations, using new metallic materials with higher melting points, such as molybdenum (Mo) and niobium (Nb) alloys [9-12, 38], Senkov *et al*. [10] reported the superior yield strength of NbMoTaW and VNbMoTaW alloys at elevated temperatures as shown in Figure 2.5. It is found that the addition of V element is beneficial to develop the yield strength, but not suitable for the heat-softening resistance. Figure 2.6 exhibits the specific yield-strength for the TaNbHfZrTi, TaNbMoW, TaNbVMoW, and $CrCoCuFeNiAl_{0.5}$ cast alloys at elevated temperature [11]. It can be seen that the high specific yield strength of the $CrCoCuFeNiAl_{0.5}$ HEAs can be sustained over to 1,100 K, and the TaNbMoW HEA can sustain its high strength to 1,800 K.

Low density and excellent room temperature ductility are required if we seek for applications in the aerospace engineering. By replacing V, Ta, and W in the NbMoTaW and VNbMoTaW alloys with lighter Cr, Mo, and Zr, respectively, the density of the new refractory $NbCrMo_{0.5}Ta_{0.5}TiZr$ HEAs alloy was reduced to 8.2 g/cm^3. In addition, the new alloy showed improved room temperature ductility,

relative to the NbMoTaW and VNbMoTaW alloys. Figure 2.7 exhibits the engineering stress–strain compression curves of the NbCrMo0.5Ta0.5TiZr alloy samples after HIP at 296 K, 1,073 K, 1,273 K, and 1,473 K [38]. During deformation at 296 K, the yield strength was 1595 MPa and continuous strengthening occurred until the alloy fractured by localized shearing at maximum strength of 2,046 MPa accumulating about a 5 % strain. During testing at 1,073 K, yield strength decreased to 983 MPa, the ultimate strength of 1,100 MPa was achieved at a strain of 4.2%, and the sample fractured by shearing at a strain of about 6%, after a decrease in strength to 1,050 MPa. An increase in the testing temperature up to 1,273 K resulted in a considerable softening of the alloy after a short stage of strain hardening. At this temperature, yield strength is 546 MPa, compressive strength is 630 MPa, and the minimum strength achieved during strain softening was 393 MPa after a plastic strain of about 22 %. At this temperature, the sample did not fracture. An increase in the temperature up to 1,473 K, led to a further decrease in the flow stress of the alloy. The ultimate stress of 190 MPa was reached shortly after yielding, followed by weak softening and a steady state flow at the minimum strength of 135 MPa. It is not that no fracture occurred at this temperature.

Figure 2.8 presents the secondary-electron microscopy (SEM) images of the fracture surface of a $NbCrMo_{0.5}Ta_{0.5}TiZr$ alloy after compression deformation at room temperature [11]. It shows a combination of plastic and brittle deformation mechanism. The formation of dimples is convincing evidence of plastic deformation [Figure 2.8(b) and (c)] while the microstructure of treated pieces is the symbol of quasi-cleavage fracture of the FCC (Laves) phase, as well as along the

interfaces [Figure 2.8(a) and (d)]. In summary, refractory HEA is a unique idea and relatively new field. Compared to compositions with 3d elements, refractory HEAs (4d elements) show exceptionally bright mechanical properties, especially at elevated temperatures. More research fields including new compositions and fracture mechanism need to be explored.

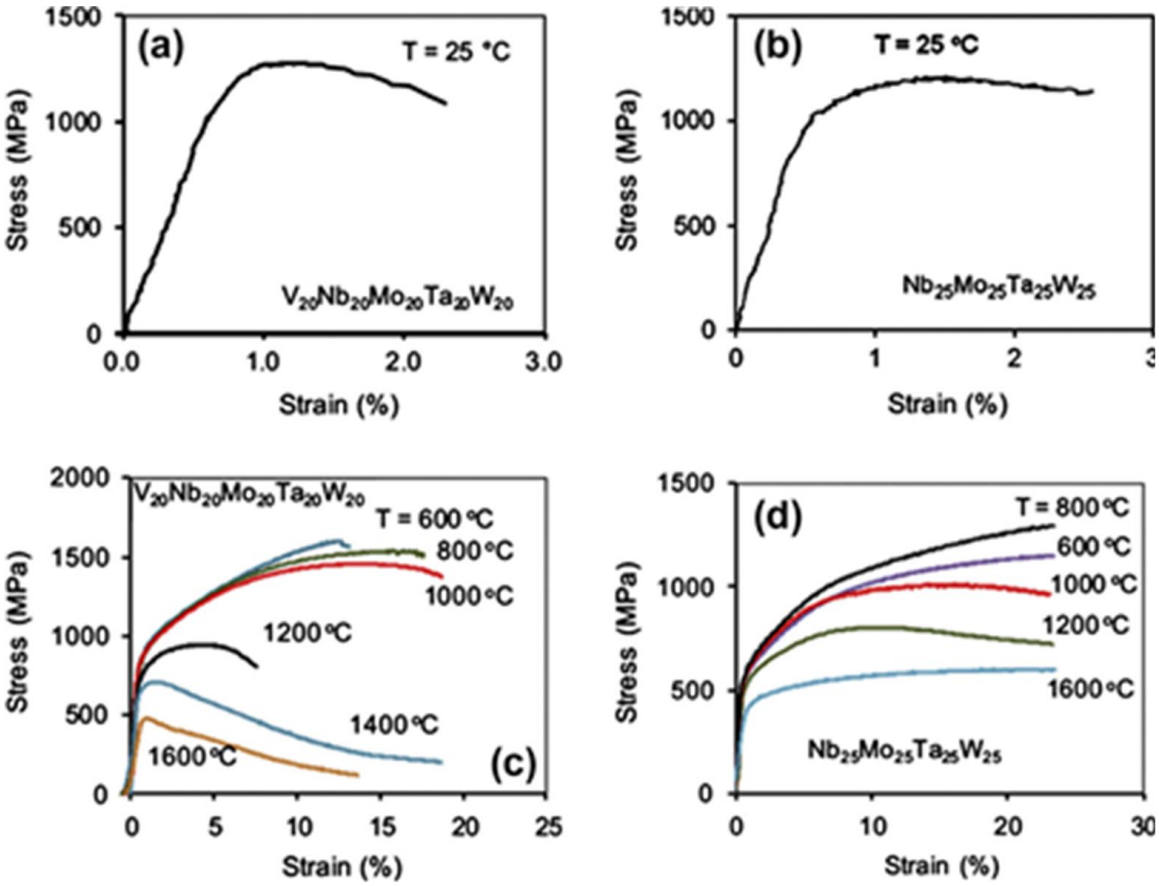

Figure 2.5 Compressive engineering stress–strain curves of NbMoTaW and VNbMoTaW HEAs at room temperature and high temperatures.

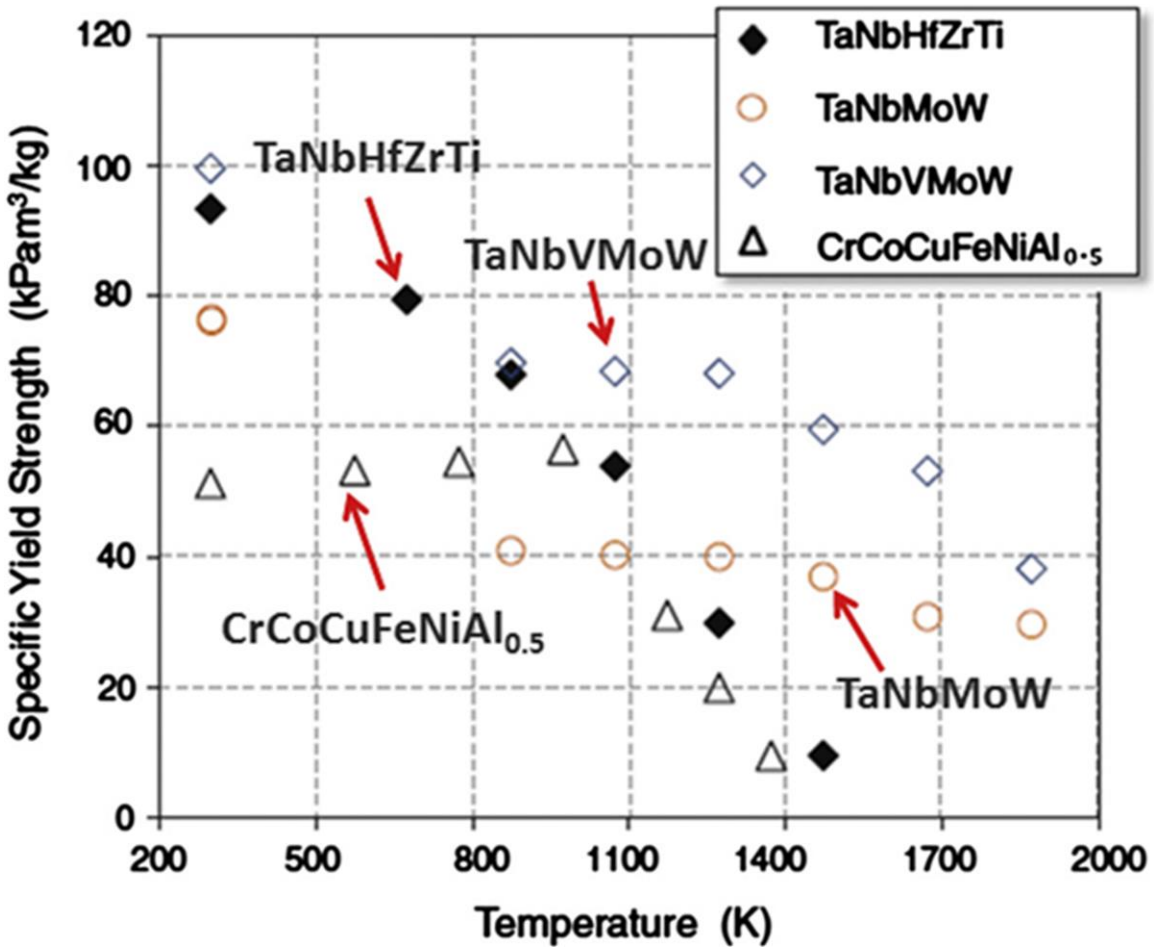

Figure 2.6 The temperature dependence of the specific yield-strength of the TaNbHfZrTi alloy in comparison with that for TaNbMoW, TaNbVMoW, and $CrCoCuFeNiAl_{0.5}$ alloys.

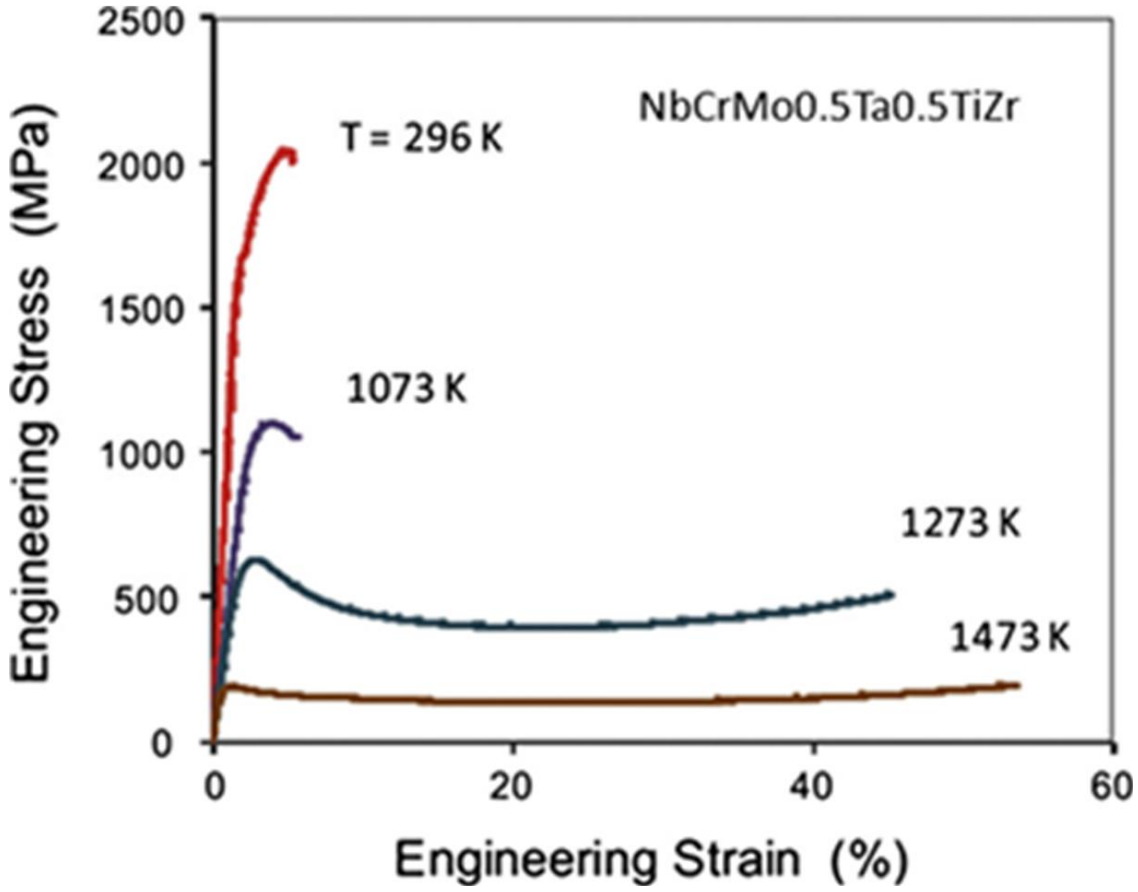

Figure 2.7 The engineering stress–strain compression curves of the $NbCrMo_{0.5}Ta_{0.5}TiZr$ alloy samples after HIP at 296 K, 1,073 K, 1,273 K, and 1,473 K.

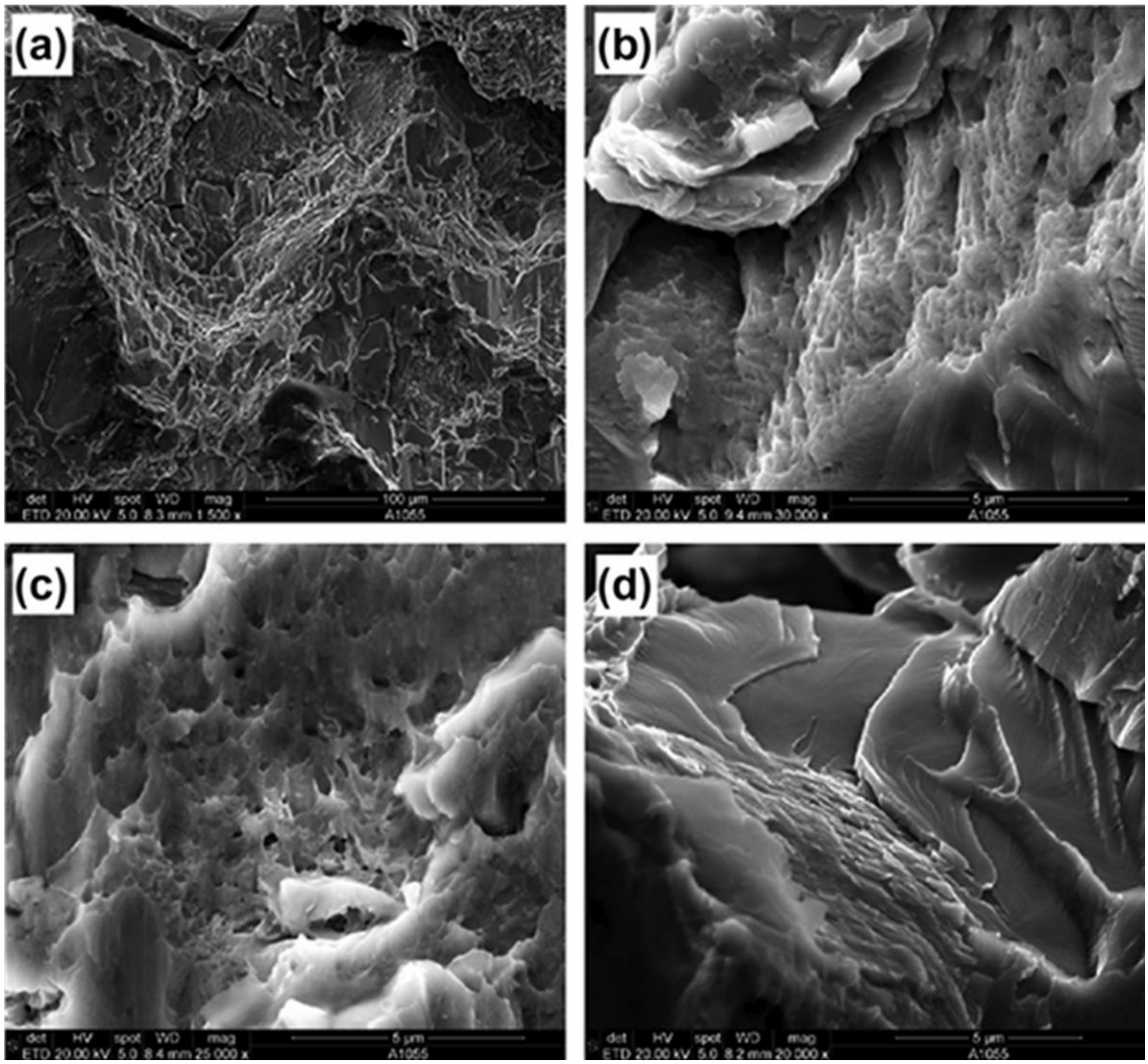

Figure 2.8 SEM images of the fracture surface of a $NbCrMo_{0.5}Ta_{0.5}TiZr$ alloy samples after compression deformation at room temperature.

2.4 Research Tasks

To achieve the fundamental knowledge and in-depth understanding of the structure-property-performance links for the BCC refractory HEAs, we proposed five tasks in this study: (1) exploration and design the new BCC refractory HEAs (Task 1); (2) measurement of lattice distortion for BCC refractory HEA (Task 2); (3) investigation on elastic/plastic deformation behaviors of BCC refractory HEA (Task 3); The new alloy composition will be design by empirical rules and CALculation of PHAse Diagrams (CALPHAD) calculation. The microstructures will be characterized with a combined use of several techniques, such as neutron-diffraction (ND), synchrotron-diffraction, X-ray diffraction (XRD), scanning-electron microscopy (SEM), energy dispersive spectroscopy (EDS), Electron Backscatter Diffraction (EBSD), atom probe tomography (APT) and scanning transmission-electron microscopy (STEM). Systematic heat-treatment will be conducted at different duration times in the temperature range of 1,000 ~ 1,200 °C in order to obtain formation of single BCC phase with homogeneous elemental distributions. Moreover, the in-situ neutron diffraction experiments coupled with Finite-Element-Modeling will be performed to study the elastic and plastic deformation behaviors at elevated temperatures. With the fundamental understanding of new designed BCC refractory HEA, the lattice distortion will be measured/calculated by neutron diffractions and First-Principles calculations. Moreover, the distorted lattice will be optimized by addition of other elements. Finally, the evolution of lattice distortions as increase of additional elements and its effect on the mechanical properties will

be quantitatively studied by experimental results coupled with theoretical calculations. By correlating the structure, properties and performance, the current research could provide the fundamental knowledge and insight into a new refractory HEAs design strategy and development of mechanical properties for applications in advanced gas turbine systems.

CHAPTER THREE

LATTICE DISTORTION IN A STRONG AND DUCTILE REFRACTORY HIGH-ENTROPY ALLOY

3.1 Introduction

Novel metallic alloys beyond Ni-based superalloys with high strengths, thermal stabilities, and large ductility at high temperatures are highly desirable in the aviation and aerospace industries. To meet the increasing demand of high-temperature alloys, exotic multi-principal-element metallic alloy systems, also referred to as high-entropy alloys (HEAs), have been proposed and studied due to their simple microstructures and promising properties. The ideal HEA design strategy is to form a single solid-solution phase, considering configurational entropy (> 1.5R, where R is the ideal gas constant), and enthalpy of formation (ΔH_f) with combinations of alloy components [1-6, 8, 39]. The reduction of the Gibbs free energy by the high configurational entropy and optimal range of enthalpy of formation leads to the formation of the simple solid-solution phase, such as face-centered-cubic (FCC) [9], body-centered-cubic (BCC) [10-13], and hexagonal-close-packed (HCP) [14, 15] structures. These features, in turn, contribute to attractive materials properties, especially, high hardness/strengths, and excellent softening resistance at high and cryogenic temperatures [3-5]. These properties of the near-equimolar HEAs are known to be associated with the locally-strained atomic structures (lattice distortion) in the simple-single solid-solution

phase. Moreover, the recently-developed twinning or transformation-induced plasticity (TWIP or TRIP) HEAs, whose compositions are greatly deviated from the near-equimolar ratios, have also attracted the increasing attention due to their excellent mechanical properties [16-21].

There have been extensive efforts to develop single-phase refractory HEAs for high-temperature applications above 1,100 °C [10-13, 22-24] and to comprehend the underlying relationship between their unique microstructure and mechanical performance. However, limited studies have investigated the lattice distortions in HEAs, using x-ray or neutron diffraction [25-27]. Furthermore, the quantitative evaluation of the lattice distortion, through statistical calculations with experimental observations, is still not fully developed. Moreover, only a small number of alloy systems have been verified as single BCC solid-solution phases from experiments [28, 29]. For instance, many HEAs exhibit not only elemental segregations in the as-cast condition, but also the formation of small amounts of ordered phases after the heat treatment [23, 30, 31, 40]. The chemical inhomogeneity and second-phase formation could hinder the fundamental and in-depth understanding of the main strengthening effect of HEAs. Therefore, the development of single solid-solution phase HEAs with homogeneous elemental distributions is vital to elucidate how lattice distortions affect mechanical properties. In the present study, we have designed a NbTaTiV refractory HEA, which contains a single BCC solid-solution phase, via the CALculation of PHAse Diagram (CALPHAD) approach [41-43]. The structure of the NbTaTiV alloy was investigated, using the integrated experimental

and theoretical approaches. The systematical heat treatments were conducted to develop the single-phase solid-solution microstructure with the fully-homogenous elemental distribution.

Furthermore, we investigated the lattice distortion and the local atomic environment of the BCC NbTaTiV alloy system through the ab initio approach, based on Special Quasirandom Structures (SQS) [43] that approximate random distributions of atomic species in a medium-sized supercell. The fully-homogeneous single-phase NbTaTiV refractory HEA shows excellent yield strengths at room and high temperatures (under 900 °C), which are mostly induced by the lattice distortion. The in-depth understanding of the lattice-distortion effect on mechanical properties gained through this investigation is expected to provide the significant strategy for the design of single-phase solid-solution refractory HEAs and their use in high-temperature applications, such as thermal-protection systems and gas-turbine engines.

3.2 Experimental Methods

3.2.1 Materials

The alloys were prepared from Nb, Ta, Ti, and V elements of 99.99 weight percent (wt.%) purity by arc-melting under the Ti-gettered argon atmosphere on a water-cooled Cu hearth. To achieve a fully-homogeneous distribution of elements, the ingot was melted over 10 times, by flipping them over between each step. From the master alloys, rods with a 4-mm diameter and 50-mm length were solidified in

a Cu mold under an atmosphere, followed by direct casting into cylindrical rods, using a drop-casting technique. These alloys were quartz-tubed with the triple-pumped argon and experienced the heat treatment at 1,000 °C for 1 day, 1,200 °C for 1 day, and 1,200 °C for 3 days. After that, the samples were water quenched.

3.2.2 Computational Methodologies

The CALPHAD calculations were carried out, using the TCNI8 thermodynamic database supplied by ThermoCalcTM [44, 45]. This database covers the entire composition ranges of all six constituent binaries of the Nb-Ta-Ti-V system. However, it is anticipated that the inclusion of thermodynamic descriptions for all ternaries will enhance the reliability of the database especially in applications for HEAs. Recent publications [40, 41, 46] detail the database developments and applications of the CALPHAD modeling for HEAs.

3.2.3 Microstructural Characterization

Scanning-electron microscopy (SEM) was conducted, using a Zeiss Auriga 40 equipped with back-scattered electrons (BSE), and energy-dispersive X-ray spectroscopy (EDS). The SEM images were analyzed, using the ImageJ software [47] to obtain the volume fractions of dendrites and interdendrites, respectively. The surface morphology of the polished samples was studied by the electron-backscatter diffraction (EBSD) to indicate the presence of a single solid-solution phase and confirm the variation of the grain size and morphology after the heat treatment.

For the APT observation, needle-shaped specimens were made, using standard lift-out methods with an FEI Nova focused ion beam (FIB) [45, 48]. The data collection was conducted, using a local electrode atom probe (CAMECA LEAP 4000X HR) equipped with an energy-compensating reflectron lens and a 10 pico-second 355 nm ultraviolet (UV)-pulsed laser. The specimen was cooled to 30 K, while a 50 pJ laser energy and a 200 kHz pulse repetition rate were used to evaporate ions with a detection rate of 0.005 ions per pulse. The data reconstruction and analysis were conducted, employing the IVAS 3.6.12 software (CAMECA instruments).

3.2.4 In-situ Neutron-diffraction Experiments

In-situ neutron-diffraction (ND) measurements of as-cast and heat-treated NbTaTiV alloys with a specimen diameter of 4 mm and length of 8 mm under compression were performed to investigate the deformation behavior at room temperature (RT), using an MTS load-frame on the VULCAN Engineering Diffractometer at the Spallation Neutron Source (SNS), Oak Ridge National Laboratory (ORNL) [49, 50]. The ND instrument utilizes the time-of-flight (TOF) arrangement, which allows for the ND measurements with a diffraction pattern, covering a wide range of d spacings without the rotation of samples or detectors. The VULCAN is equipped with two detectors, designated as Banks 1 and 2 at +/- 90 degrees. These two detectors were employed to record diffraction patterns corresponding to the lattice planes, which are parallel to the axial and transverse directions, respectively. The sample is illuminated by the incident neutron beam of

a 3 × 3 mm^2 slit size and 2-mm collimators. During the measurement of the diffraction patterns, a constant load-control mode with a stepwise-loading sequence was utilized. The measurement time of the neutron-diffraction data was 20 minutes at each stress level. When the stress level reached 1,100 MPa (close to the yield strength), the control mode was changed from the load to displacement control modes with an incremental step of 0.2 mm. The collected data were analyzed by single-peak fitting, using the VULCAN Data Reduction and Interactive Visualization software (VDRIVE) program [51].

3.2.5 Mechanical Tests

The mechanical experiments were carried out under uniaxial compression for the as-cast alloy at RT, as well as the heat-treated alloy at RT, 300 °C, 500 °C, 700 °C, 800 °C, and 900 °C, using a computer-controlled Material Test System (MTS) servo-hydraulic-testing machine. It was very difficult to obtain high-quality specimens without the cast flaws, such as pores using copper-mold drop casting. Alternatively, further processes, such as rolling, are necessary to remove the flaws. Indeed, the secondary processing, i.e., rolling, seems to be quite effective to eliminate the micro-flaws formed during solidification. However, the microstructure, such as the grain size of samples after secondary processing, will be significantly changed or modified from that of the as-cast microstructure. It is believed that uniaxial compression is a possible method to obtain the intrinsic mechanical properties of as-cast and heat-treated NbTaTiV refractory HEAs. The experiments were conducted at an initial strain rate of 10^{-3} s^{-1} with a specimen diameter of 4

mm and length of 8 mm (aspect ratio of 2:1). During the experiments at high temperatures, the test specimens were heated to the desired temperature by a furnace. The surface of the heat-treated specimen was polished to observe the surface-deformation morphology after 15 % deformation.

3.2.6 First-principles Calculations

The total-energy calculations were performed, using the Vienna ab initio simulation package (VASP) [52] based on the density functional theory (DFT) with the projector augmented wave (PAW) [53, 54] method. The Perdew-Burke Ernzerhof (PBE) [55] function under the non-spin polarized generalized gradient correction interaction is used to describe the exchange and correlation interaction. The kinetic energy cutoff of 500 eV for the plane-wave basis is employed. Using the Monkhorst-Pack scheme, the Brillouin zone integration is carried out at 5 × 5 × 5 k-points [56]. The convergence threshold for energy is 10^{-4} eV, while the symmetry-unrestricted optimization for the geometry is performed, employing the conjugate gradient scheme until the residual force on each atom is less than 0.01 eV/Å.

3.3 Results

3.3.1 Computational Prediction of Phase Formation and Evolution via CALPHAD Approach

The CALPHAD calculations were used to predict the microstructure of the NbTaTiV alloy. Figure 3.1 shows the predicted equilibrium and non-equilibrium phase mole fraction versus temperature plots in the alloy system. A single BCC

solid solution is predicted to form with the bulk composition of $Nb_{23.8}Ta_{25.5}Ti_{24.9}V_{25.8}$, atomic percent (at. %). The calculated liquidus and solidus temperatures are T_{liq} = 2,161 °C and T_{sol} = 1,941 °C, respectively. The BCC solid solution decomposes into a minor HCP phase at T_{dec} = 432 °C. The ratio of the temperature range where the BCC solid solution is stable over the solidus temperature $[\mathrm{i.e.}, (T_{sol} - T_{dec})/T_{sol}]$ is determined to be 0.78. Gao *et al.* [57] previously proposed that a ratio greater than 0.30 typically favors a single-phase solid solution in the as-cast state.

The non-equilibrium solidification was simulated, using the Scheil-Gulliver model [58], which assumes equilibrium mixing in the liquid state and no diffusion in the solid state. The simulation predicts the formation of a single BCC solid solution during the entire non-equilibrium solidification. Based on the evidence, the real solidification path is thought to be somewhere between the equilibrium and Scheil-Gulliver model. The simulation also predicts the chemical segregation associated with Ta, Ti, and V due to constitutional cooling. It is believed that as the temperature decreases, the BCC phase is rich in Ta at earlier stages of solidification in the dendrite arms, while the interdendritic region is enriched in Ti and V in later stages (the inset in Figure 3.1).

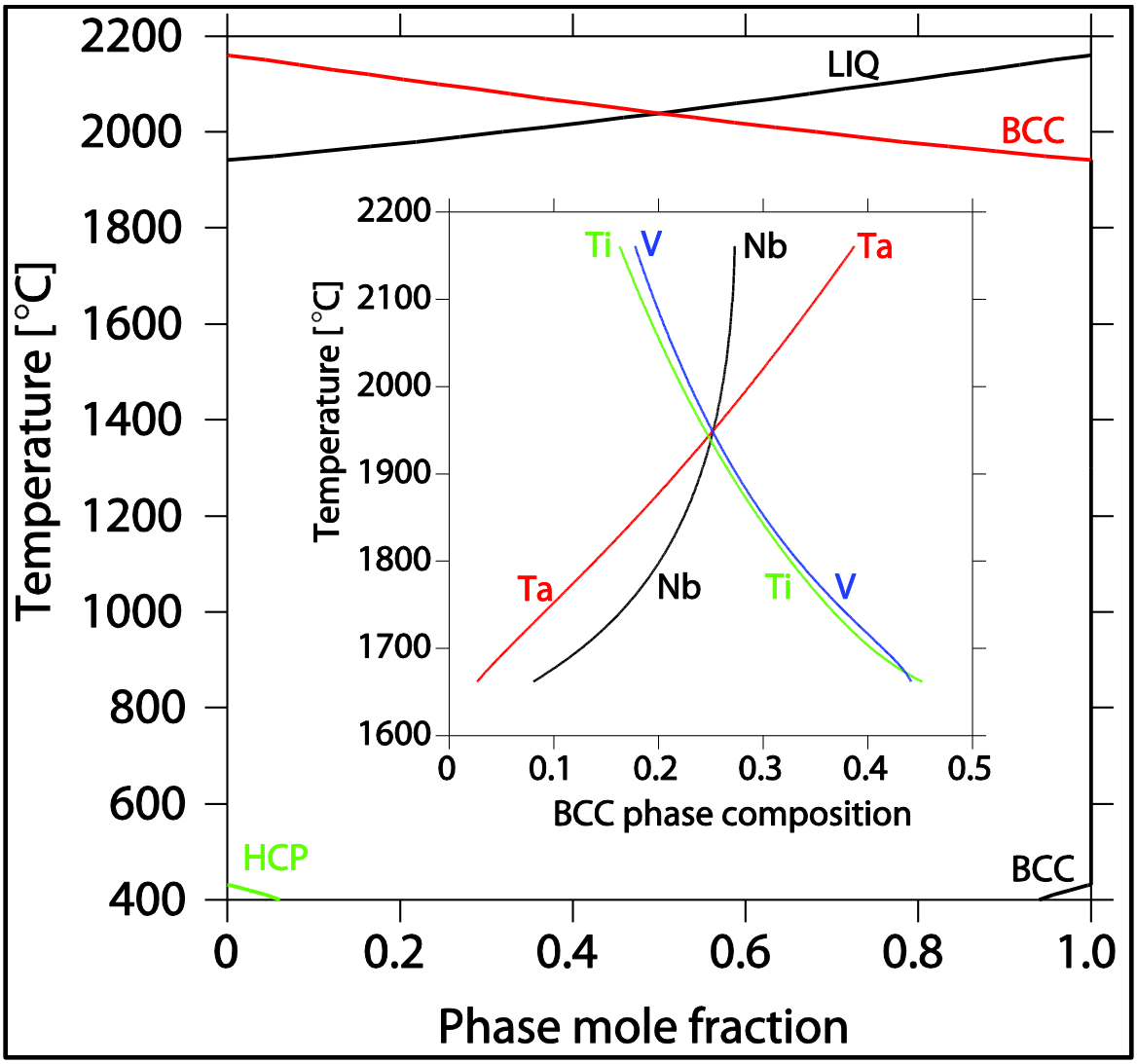

Figure 3.1 CALPHAD-calculation data for NbTaTiV. Calculated equilibrium phase mole fractions during solidification for Nb23.8Ta25.5Ti24.9V25.8. The inset shows the composition evolution of the BCC solid-solution phase during non-equilibrium solidification using the Scheil–Gulliver models.

3.3.2 Chemical Inhomogeneity in the As-cast Sample

Figure 3.2(a) shows the scanning-electron microscopy (SEM) back-scattered electron (BSE) image of the as-cast NbTaTiV refractory HEA. The microstructure consists of dendritic and interdendritic regions without any secondary phase. The different contrast between the dendritic and interdendritic regions suggests that elemental segregation occurs during the solidification process. The elemental distributions and chemical compositions of dendritic and interdendritic regions in the as-cast alloy were examined by the energy-dispersive-spectroscopy (EDS) mapping and point EDS analysis (not shown). The dendrite is enriched in Nb and Ta, while Ti and V are more preferentially distributed in the interdendritic region, which is consistent with the CALPHAD calculation in Figure 3.1. The results of chemical compositions are summarized in Table 3.1.

The neutron-diffraction (ND) pattern in Figure 3.2(b) reveals the formation of a single BCC phase without clear features related to the chemical segregation. Similarly, the EBSD-phase map in Figure 3.2(c) shows the presence of a single BCC solid-solution phase. These results indicate that the ND and EBSD techniques can properly characterize the crystallographic-based microstructural features, such as the phase formation and grain size.

Atom probe tomography (APT) was performed to confirm the chemical homogeneity of the as-cast sample at the atomic scale and the composition of each region. Figure 3.2(d) and (e) present elemental maps and one-dimensional concentration-depth data from the dendritic (bright contrast) and interdendritic

(dark contrast) regions in analyzed volumes of 74 × 71 × 79 nm^3 and 81 × 76 × 114 nm^3 in the as-cast condition, respectively. The dendritic region was found to have a calculated composition of Nb 27.265, Ta 27.381, Ti 21.862, and V 22.150, at. %, while the interdendritic region had a calculated composition of Nb 20.997, Ta 11.669, Ti 33.149, and V 32.164, at. %.

The homogeneity of the atomic distributions within the APT dataset was evaluated via the chi-squared statistics using a frequency distribution analysis (FDA) [58], in which compositions from 100 ion bins of the observed data were compared to a binomial distribution, which represents a random solid solution. The results of this analysis are presented in the inset of Figure 3.2(d) and (e) with the experimental data (dots) overlaid on the theoretical binomial (random) distribution (solid line). The experimental results were in good agreement with the random binomial distribution, indicating random atomic arrangements within the atom-probe dataset. The μ value or χ^2 normalized to the sample size quantifies the extent of the elemental-distribution randomness. Only the μ value is reported in this case (see Table 3.1) due to the very large sample size, which causes the p test to be extremely sensitive to small variations. The μ value ranges from 0 to 1, with 0 indicating a complete random solid solution, and 1 representing a complete association of the elements. The χ^2 statistics applied to the APT data, including the μ value, are explained in more detail by Moody *et al*. [59] and Miller [58]. One-dimensional concentration-depth profiles taken along a 10-nm cylindrical region further reflect that there are no statistically-significant concentration fluctuations in

the dendritic and interdendritic regions, as shown in Figure 3.2(d) and (e). However, there are clear chemical-composition differences between the two regions. The dendritic region contains higher amounts of Nb and Ta elements, whereas the interdendritic region consists of higher amounts of Ti and V, which are consistent with the EDS results (Table 3.1), and CALPHAD prediction (Figure 3.1).

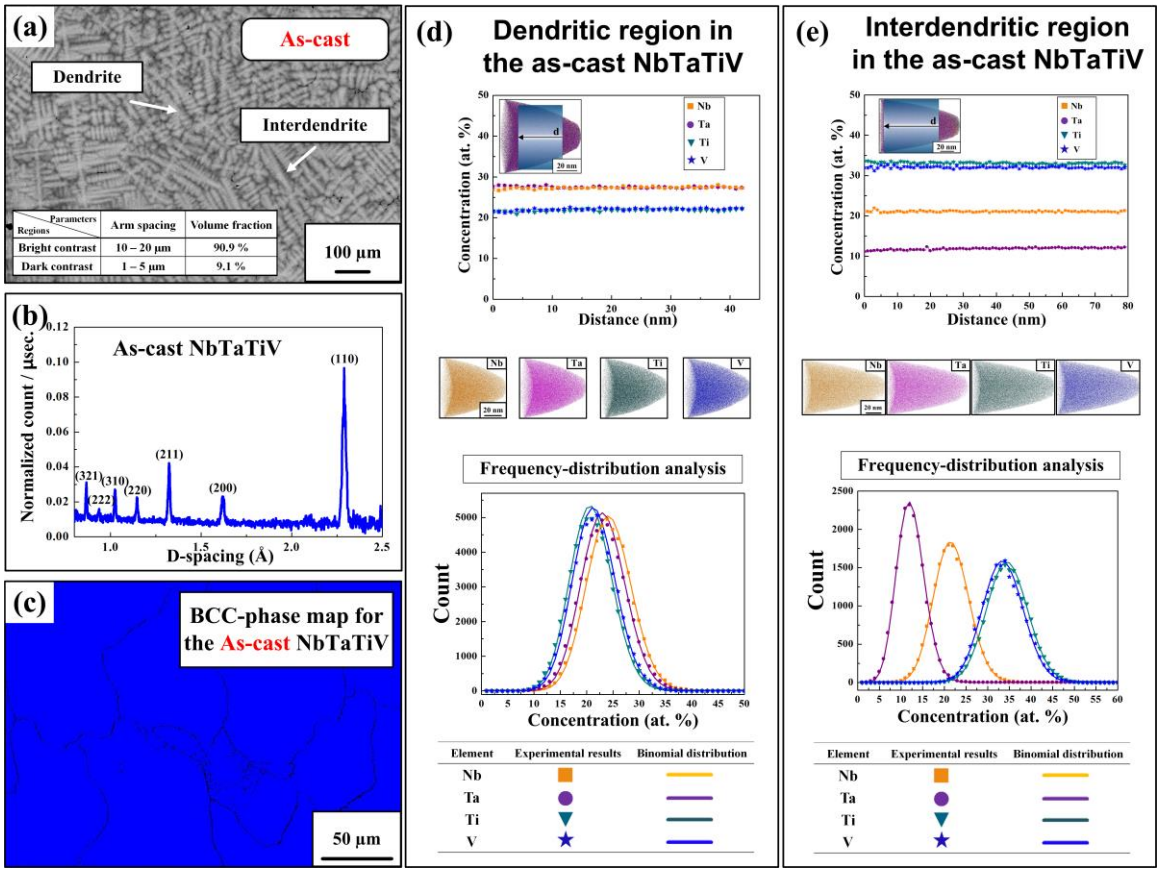

Figure 3.2 Phase and microstructural characteristics of as-cast NbTaTiV, studied by SEM, ND, EBSD, and APT data. (a) The dendritic microstructure in SEM-BSE images of the as-cast NbTaTiV alloy (b) Neutron-diffraction patterns with the peaks indexed for a BCC structure (c) EBSD-phase map of the as-cast NbTaTiV alloy (d) Concentration-depth profile of all alloying elements taken along the black arrow (top), three-dimensional atom maps of individual elements (middle) and frequent-distribution histograms (bottom), for the dendritic region, and (e) Interdendritic region in the as-cast NbTaTiV alloy.

Table 3.1 SEM-EDS and APT compositions, and elemental distribution analyses of as-cast and homogenization-treated refractory NbTaTiV HEAs. Chemical composition (in atomic percent, at. %) of constitutive regions in as-cast and homogenized alloys, determined using the energy-dispersive spectroscopy (EDS) and atom-probe tomography (APT), respectively. The binomial distribution of the analyzed data in comparison to the binomial distribution of the theoretical data is provided by the parameters of χ^2 and μ for each element.

Parameters / Materials	-	EDS results	APT results	
Alloys	**Elements**	**Average of atom fraction (%)**	**Average of atom fraction (%)**	**μ**
As-cast NbTaTiV (Bright contrast region)	**Nb**	**28.6**	**27.265**	**0.0564**
	Ta	**33.7**	**27.381**	**0.1029**
	Ti	**19.8**	**21.862**	**0.0779**
	V	**17.9**	**22.150**	**0.1014**
As-cast NbTaTiV (Dark contrast region)	**Nb**	**18.9**	**20.997**	**0.0422**
	Ta	**9.0**	**11.669**	**0.0390**
	Ti	**36.3**	**33.149**	**0.0586**
	V	**35.8**	**32.164**	**0.0664**
Homogenized NbTaTiV	**Nb**	**23.8**	**24.944**	**0.0375**
	Ta	**25.5**	**23.627**	**0.1328**
	Ti	**24.9**	**25.076**	**0.0820**
	V	**25.8**	**24.959**	**0.0379**

3.3.3 Tailoring Single Phase with Homogeneous Chemistry via Thermal Treatment

As an attempt to achieve a homogeneous single phase without the compositional segregation in the as-cast alloy, systematic thermal treatments have been conducted, based on the CALPHAD results (i.e., heat treatments at 1,000 °C for 1 day, 1,200 °C for 1 day, and 1,200 °C for 3 days). As the homogenization temperature and duration increase, an apparent microstructural variation is observed, as shown in Figure 3.3(a-c). The dendrite-arm spacings and volume fractions of dendritic and interdendritic regions for the sample heat-treated at 1,000 °C for 1 day are slightly larger [Figure 3.3(a)] than those of the as-cast sample [Figure 3.2(a)]. The quantitative difference of dendrite-arm spacings and volume fractions are summarized in each figure. This variation implies an insufficient diffusion at the above temperature. The heat treatment at 1,200 °C for 1 day leads to the blurred contrast between dendrites and interdendrites [Figure 3.3(b)], which indicates a gradual reduction of the compositional segregation.

To obtain a fully-homogeneous elemental distribution, the sample was subjected to a longer heat treatment at 1,200 °C. This thermal treatment results in the complete elimination of the dendritic segregation concomitant with the grain growth (grain sizes of 200 – 400 μm), as observed in Figure 3.3(c). The EDS measurements (not shown) were conducted to further confirm the homogeneous chemical distribution in the sample heat-treated at 1,200 °C for 3 days. No formation of other phases along the grain boundary as well as inside the grain was

observed. The specific chemical composition for the homogenized microstructure was investigated by the point EDS analysis. Importantly, each element was distributed as a nearly-equi-atomic percentage throughout the sample. The results of chemical compositions are summarized in Table 3.1. The ND pattern and EBSD-phase map show that there is no obvious formation of the secondary phase or phase transformation after the heat treatment [Figure 3.3(d) and (e)].

The atomic-scale distribution of elements for the homogenized sample was measured, using an analyzed volume of 63 × 61 × 75 nm^3 by APT. The APT results reveal a uniform distribution of alloying elements with near-equal atomic concentrations, as can be seen in Figure 3.3(f). The FDA in Figure 3.3(g) shows a good agreement between the experimental data and the binomial distribution [28, 59]. The μ values, as discussed above, can be found in Table 3.1. Note that the APT-tip samples were extracted, adjacent to the grain-boundary region, to ensure a homogeneous elemental distribution, as secondary phases tend to precipitate along grain boundaries [60]. In short, the chemical segregation in the as-cast state was effectively eliminated by a systematic heat-treatment process, and the single-phase solid solution with the atomic-scale random elemental distribution was accomplished.

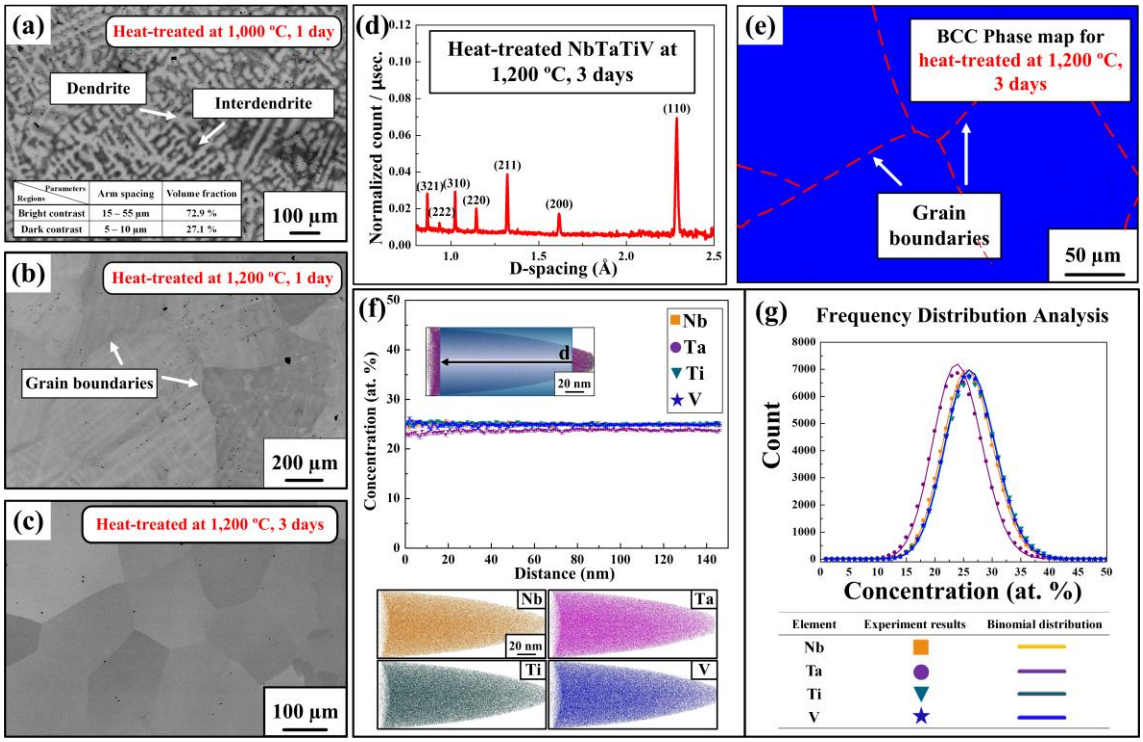

Figure 3.3 Microstructural evolutions of the NbTaTiV alloy, studied by SEM, ND, EBSD, and APT data. The SEM-BSE images of after-annealed samples at different temperatures and time periods: (a) 1,000 °C for 1 day, (b) 1,200 °C for 1 day, and (c) 1,200 °C for 3 days, (d) Neutron-diffraction patterns of the NbTaTiV alloy after the heat treatment at 1,200 °C for 3 days with the peaks indexed for a BCC structure. (e) EBSD-phase map of the homogenization-treated NbTaTiV alloy, and (f) A one-dimensional concentration-depth profile of all alloying elements taken along the black arrow for the homogenization-treated NbTaTiV alloy. Three-dimensional atom maps of individual elements (g) FDA of constituent elements with a block size of 100 atoms for the homogenized NbTaTiV alloy.

3.3.4 Mechanical Properties at Room and Elevated Temperatures

Figure 3.4(a) presents the compressive engineering stress-strain curves of the as-cast and homogenization-treated NbTaTiV alloys at RT with a strain rate of 1×10^{-3} s^{-1}. The yield strengths (σ_y) of the as-cast and heat-treated samples are comparable (as-cast: 1,236 MPa, and heat-treated: 1,273 MPa) without the fracture occurring at a compressive strain limit of 30 %. The compression experiments at RT were carried out, using the in-situ ND to investigate the deformation behavior during elastic and plastic deformations. Figure 3.4(b) and (c) exhibit the corresponding lattice-strain evolutions of (110) and (200) planes along the loading direction, as a function of the applied stress for the as-cast and homogenized samples, respectively. The lattice strains during loading, εhkl, are calculated from the shift of single-peak positions, using

$$\varepsilon_{hkl} = \frac{d_{hkl} - d_{hkl,0}}{d_{hkl,0}} \tag{3.1}$$

where dhkl is the d-spacing obtained from the hkl diffraction at a given load, and dhkl,0 refers to the value without the load. The lattice-strain evolution can provide the (hkl) plane-specific lattice strain during deformation. Generally, the [110]-oriented grains yield initially, because the [110] orientation is preferred for the slip in the BCC structure, and then the additional load transfers to [200]-oriented grains, resulting in the increase of the [200] lattice strain, which is known as load sharing or partitioning [61]. Our results obtained from both the as-cast and homogenized samples show the similar load-sharing trend, as observed in the

conventional BCC alloys. However, the slopes of [110] and [200] lattice strains increase during the loading to 750 – 850 MPa, and 900 – 1,000 MPa, respectively, in the as-cast condition. In contrast, the slopes for the homogenized state maintain a linear response until 1,100 MPa.

The lattice-strain evolutions for [110] and [200] grains reveal that the stress value for the elastic-plastic transition of the as-cast sample (~ 1,000 MPa) is slightly lower than the homogenized one (~ 1,100 MPa), which is consistent with the engineering stress-strain behavior [Fig. Figure 3.4(a)]. Figure 3.4(d) and (e) illustrate the variations in the normalized peak width (W/W_0) of [110], [200], [211], and [310] peaks as a function of engineering strain. Note that the reference peak width (W_0) was taken at the initial diffraction pattern (before the applied stress). For both conditions, no significant changes of peak widths were observed during elastic deformation. After yielding, however, the peak widths of the homogenized sample [Figure 3.4(e)] increase more considerably than those of the as-cast one during plastic deformation. The width increase could be associated with the stress-induced heterogeneous substructure, such as distortion and twining [62, 63]. However, based on our examination concerning the lateral surface of the 15 % deformed specimens using SEM and EBSD as shown in Figure 3.5, a number of slip bands are observed without the formation of twin bands. These results indicate that the plastic-deformation behavior is mainly dominated by the dislocation-slip mechanism, and during the deformation of the homogenized sample, more dislocations are produced as the plastic deformation proceeds.

The elevated-temperature compressive tests were performed up to 900 °C at a strain rate of 1 x 10^{-3} s^{-1} for the homogenized alloy, and the stress-strain curves are illustrated in Figure 3.6. As the temperature increases, the yield strength gradually decreases from 1,273 MPa (RT) to 688 MPa (900 °C). Similar to the RT stress-strain curve, potent strain hardening is retained up to 800 °C, but a slight reduction of the hardening capability is observed at 900 °C. Note that the samples did not fracture up to a compressive strain limit of 30 %. The values of the yield stress (σ_y) for the homogenized NbTaTiV alloy as a function of temperature are summarized in Figure 3.6.

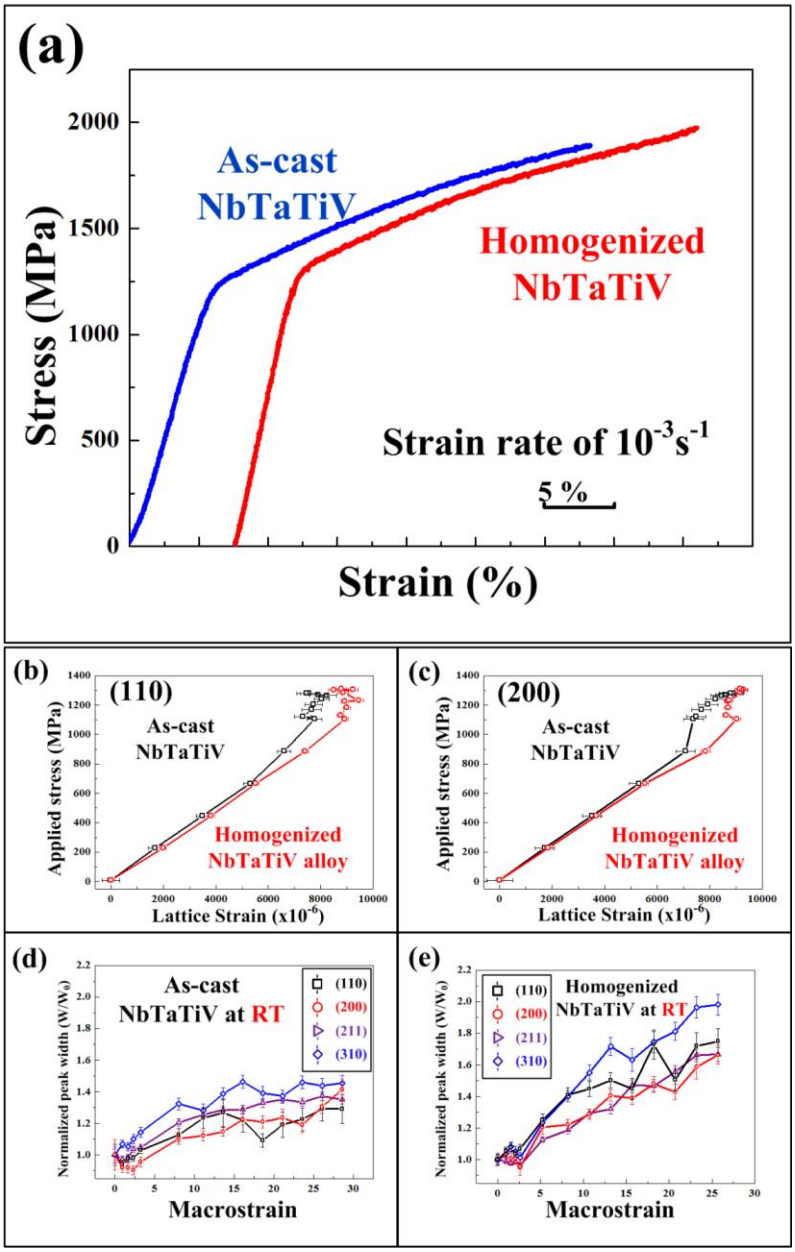

Figure 3.4 Comparison of mechanical properties and in-situ neutron-diffraction data of the as-cast and homogenization-treated NbTaTiV. (a) Engineering compressive stress-strain curves of the as-cast and homogenization-treated NbTaTiV at room temperature. Evolution of lattice strains for (b) [110] (c) [200] oriented planes in as-cast (black line) and homogenization-treated (red line) alloys as a function of applied stress. Evolution of normalized peak widths as a function of macro-strain for (d) As-cast, and (e) Homogenization-treated NbTaTiV HEAs.

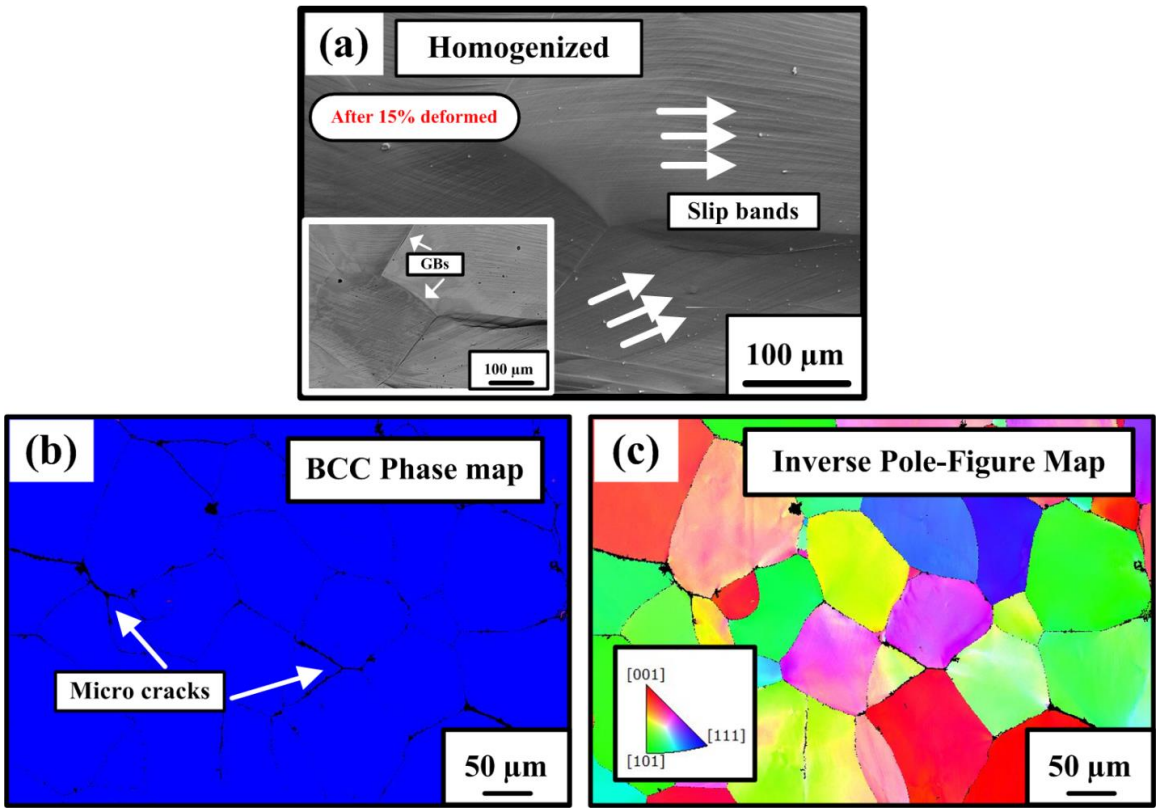

Figure 3.5 SEM and EBSD images of the deformed lateral surface. (a) SEM micrograph of the homogenization-treated alloy after 15 % deformation. (b and c) The EBSD phase and inverse pole-figure mapping images of the 15 %-deformed homogenized NbTaTiV at room temperature. The SEM micrograph of the 15 %-deformed homogenized sample shows a large density of slip bands that were nonuniformly oriented within different grains formed during plastic deformation. Furthermore, no strain-induced phase transformation was found to occur during compression testing, i.e., the single BCC solid-solution phase is observed on the phase map, and other deformation bands, such as local twin bands, were not observed from EBSD analyses.

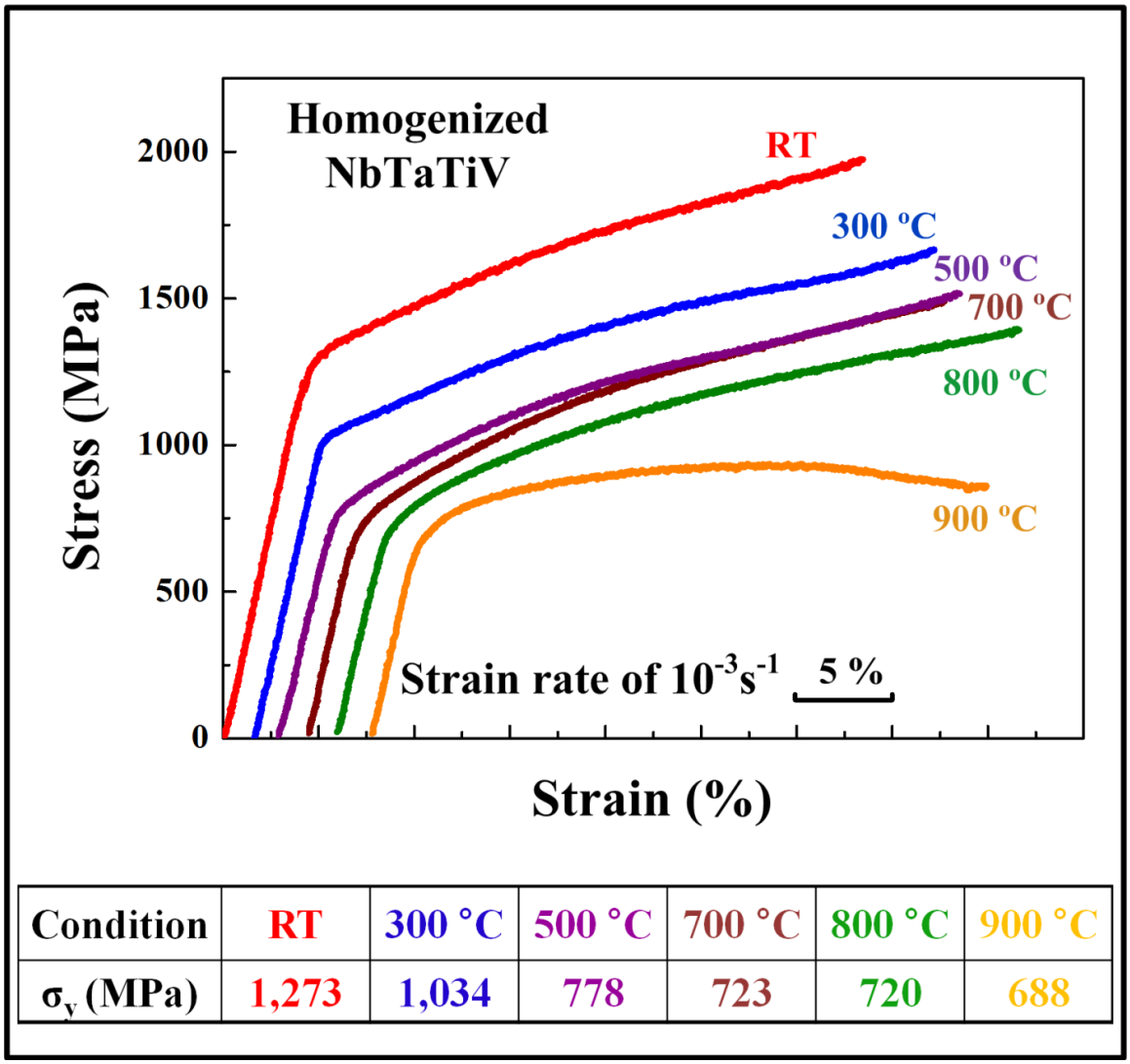

Condition	RT	300 °C	500 °C	700 °C	800 °C	900 °C
σ_y (MPa)	1,273	1,034	778	723	720	688

Figure 3.6 Mechanical properties for NbTaTiV at elevated temperatures. Compressive engineering stress-strain curves and a summary of compression-yield strength (σ_y) for the homogenization-treated NbTaTiV alloy obtained at room temperature, 300 °C, 500 °C, 700 °C, 800 °C, and 900 °C, respectively.

3.4 Discussion

3.4.1 Homogenization-treatment Effects

The unique property of HEAs is obtained by increasing the configurational entropy, which introduces a simple solid-solution microstructure with severe lattice distortions caused by the random distribution of the constitutive elements that vary appreciably in size. Therefore, it is expected that the extent of the distortion effect is maximized when all the elements are homogenously distributed without the second-phase formation. In the present work, the fully-homogeneous single solid-solution microstructure in the NbTaTiV refractory HEA was achieved through experimental and theoretical approaches. The clear microstructural evolution was captured from the chemically-inhomogeneous to simple BCC structures after the heat treatments. The chemical inhomogeneity is associated with the different melting temperature of each element in the alloy system. The segregation ratio, $S_R = (C_{dr})_i/(C_{idr})_i$, which considers the melting temperature of each constituent element [64] of the alloying component, was used to quantify the influence on micro-segregation. Here, the $(C_{dr})_i$ and $(C_{idr})_i$ are the atomic fractions of the element, *i*, in the dendritic and interdendritic regions, respectively. The calculated S_R values for Nb, Ta, Ti, and V in the as-cast sample based on the APT chemical analysis are 1.30, 2.35, 0.65, and 0.69, respectively. These values reflect that the Nb and Ta elements with high melting temperatures contribute mainly to the formation of dendritic regions, whereas the Ti and V elements with lower melting temperatures

are preferentially distributed in the interdendritic regions. This calculation trend is consistent with the CALPHAD results (the inset in Figure 3.1)

Based on the configurational-entropy approach, the chemical inhomogeneity in the as-cast sample is expected to reduce the distortion effect, as compared to the fully-homogeneous sample, which determines the extent of strengthening in the materials. However, the alloys in both states exhibit similar yield strengths. This trend could be due to other microstructural differences between the as-cast and heat-treated alloys, such as the grain size and possible presence of the residual stress during the casting process, as well as the compositional segregation making it difficult to clarify the influence of lattice distortion. Nevertheless, the variation at the distortion level during microstructural evolution could be determined by features obtained from neutron diffraction, such as lattice parameters and peak intensities. The lattice parameters of the as-cast sample and the heat-treated sample at 1,200 °C for 3 days were determined from the ND patterns, using a single-peak fitting approach [65], and the averaged lattice parameters from the peaks observed were estimated to be 3.2372 ± 0.0002 Å and 3.2318 ± 0.0001 Å, respectively. A theoretical crystal-lattice parameter (amix) of the NbTaTiV alloy can be estimated with the rule of mixtures approach:

$$\mathrm{a}_{mix} = \sum_{i=1}^{n} c_i a_i \tag{3.2}$$

where *n* is the number of alloy components, c_i is the atomic fraction of the ith element, and ai is the lattice parameter of the ith element. The lattice parameters

measured for both as-cast and homogenized samples are slightly different with those acquired from the rule of mixtures (3.2342 Å), which could indicate lattice distortions in both cases.

3.4.2 Quantitative Measurement of Lattice Distortion via Experimental and Theoretical Calculations

Lattice distortion, which essentially originates from the atomic-size mismatch in an alloy, constitutes one of the main features distinguishing HEAs from other metallic materials [4]. Importantly, lattice distortion affects the deformation mechanism as well as the mechanical properties of HEAs [25, 26, 66]. For example, severe lattice distortions produce unconventional dislocation lines in HEAs, leading to a distinct deformation mechanism in metallic materials [67]. These lattice distortions also introduce energy barriers against dislocation motions and serve as a strengthening mechanism [67]. Many properties of solid-solution HEAs, e.g., the phase stability and atomic-level stresses, are found to be correlated with the overall atomic-size mismatch [68, 69].

There are experimental and theoretical reports regarding the influence of the lattice distortion on the diffraction-peak intensities in HEAs [25, 26]. Specifically, the Cu-Ni-Al-Co-Cr-Fe-Si HEAs exhibit a considerable reduction in the XRD or ND intensities with the increase of the number of additional principal elements [26]. It is suggested that the atomic deviation from their neutral positions (structural distortion) gives rise to the substantial deviation of the crystallization integrity, and, thus, an enhanced scattering effect [26]. In the present study, the ND results

indicate that the intensity of the [110] peaks for the homogenized sample is reduced by approximately 27 %, as compared to the as-cast condition. Note that the diffraction peaks are fitted by the single-peak fitting method and, then, divided by the proton charge to conduct the precise comparison of peak heights. It can be deduced that severe lattice distortions are expected to exist in the homogenized sample. Furthermore, the evolutions of lattice strains and normalized peak widths during deformation, obtained by in-situ neutron studies, indicate that the slips of the as-cast alloy in the (110) and (200) oriented planes occur earlier than the homogenization-treated alloy, and a high density of dislocations is formed during plastic deformation. These distorted lattices induce the formation of local elastic-stress fields. During deformation, mobile dislocations could interact with the local elastic-stress fields. These stress fields could hinder the dislocation movements, which accounts for the high amounts of dislocations during plastic deformation [70].

Recently, Toda-caraballo *et al.* developed the strengthening theories to evaluate solid-solution strengthening in multicomponent alloy systems [71]. For solid-solution strengthening of metallic solid solutions originates from the elastic interactions between local stress fields of solute atoms and those of dislocations [67, 72]. The interaction force (*F*) can be estimated as

$$F = \mathrm{Gb}^2\delta = \mathrm{Gb}^2[\beta\delta_a + \delta_G] \tag{3.3}$$

where $\delta_a = \frac{1}{a}\frac{da}{dc}$, $\delta_G = \frac{1}{G}\frac{dG}{dc}$, G is the shear modulus of the alloy, b is the Burgers Vector, and β is the constant, which is related with the type of the mobile

dislocations. Typically, β is 2 - 4 for screw dislocations and ≥ 16 for edge dislocations, respectively [71-73]. Since most of alloys are strengthened by a mixture of edge and screw dislocations, the β was determined to be 9 [12, 74]. In a concentrated solid solution, the solute induced stress, Δσ, can be expressed as:

$$\Delta\sigma = \frac{AF^{4/3}c^{2/3}{E_L}^{-1/3}}{b^2} \tag{3.4}$$

where *A* is a dimensionless material constant, *c* is a solute concentration, and E_L is the dislocation-line tension.

In the case of the single solid-solution phase HEA, the elastic and atomic-size mismatches are major factors for the solid-solution strengthening, which can be expressed as [12]:

$$\Delta\sigma_s = \Delta\sigma_a + \Delta\sigma_G \tag{3.5}$$

where $\Delta\sigma_a$ and $\Delta\sigma_G$ are the strengthening contributions from the atomic-size mismatch (lattice distortion), and elastic-modulus mismatch (modulus distortion), respectively. According to Eqs. (3) and (4), the solute-induced stress with the consideration of the lattice distortion and modulus distortion can be expressed as [75]:

$$\Delta\sigma_{a(G)} = \mathrm{A'G}{\delta_{a(G)i}}^{4/3}{\mathrm{c}_{a(G)i}}^{2/3} \tag{3.6}$$

where $\mathrm{A'}$ is a material-dependent dimensionless constant of the order of 0.04, G is the shear modulus of the alloy, δ_i is the estimated average difference of the atomic size or shear modulus, and c_i is the solute concentration [74, 75]. In case of a single BCC phase HEA, the δ_{ai} and δ_{Gi} in the adjacency of an element, *i*, are

evaluated as averages of the atomic-size and modulus differences of this element with its neighbors, respectively,

$$\delta_{ai} = \frac{9}{8}\sum c_j \delta_{aij} \tag{3.7}$$

$$\delta_{Gi} = \frac{9}{8}\sum c_j \delta_{Gij} \tag{3.8}$$

where $\delta_{aij} = 2(r_i - r_j)/(r_i + r_j)$, $\delta_{Gij} = 2(G_i - G_j)/(G_i + G_j)$, and c_j is the atomic fraction of jth element in the alloy.

According to the above equation, the strengthening components in the NbTaTiV alloy due to the lattice and modulus distortions are estimated to be $\Delta\sigma_a \approx$ 431 MPa, and $\Delta\sigma_G \approx$ 227 MPa, respectively. This result indicates that the lattice distortions are likely to be the dominant strengthening factor rather than modulus distortions in this alloy system.

From this point of view, one can point out that the quantitative as well as qualitative measurement of lattice distortions in the homogenized alloy is apparently important for understanding the strengthening mechanism. Yeh *et al.* [26] suggested the mathematical parameters of the distortion effect from the x-ray diffraction (XRD) structure factor of $\bar{F}_{hkl}^{T,D} = F_{hkl}\, exp(-M^T - M^D)$, which is formulated by the combination of the Debye-Waller temperature factor, $M^T = 8\pi^2(\bar{u}^2)^T \left(\frac{sin\,\theta}{\lambda}\right)^2$, and lattice-distortion factor, M^D, where θ and λ are the angle and wavelength of the incident x-ray beam, respectively. This thermal factor is remarkably associated with the vibration amplitude of atoms, $\bar{u}^T$. Similar to the vibrational amplitude of atoms caused by thermal effects, the lattice-distortion factor, M^D, is formulated as:

$$M^D = 8\pi^2(\bar{u}^2)^D \left(\frac{sin\,\theta}{\lambda}\right)^2 \quad (3.9)$$

In this factor, which is modified from M^T, the deviation displacement of atoms due to the intrinsic lattice distortion, $\bar{u}^D$, is the major effective term to determine M^D. The $\bar{u}^D$ can be expressed by the following equation:

$$\bar{u}^D = \sqrt{\sum_i^n \left(d_i^{eff} - \bar{d}\right)^2} \quad (3.10)$$

where d_i^{eff} is the effective lattice constant of the *i*th element, and $\bar{d}$ is the average lattice constant of *n* elements, which are obtained from the atomic size of the incorporated elements related to the crystal structure. The effective lattice constant, d_i^{eff}, is calculated by:

$$d_i^{eff} = \sum_j^n f_j \left(1 + \frac{\Delta V_{ij}}{V_i}\right)^{1/3} d_i \quad (3.11)$$

where f_j is the atomic fraction, V_i is the atomic volume, d_i is the lattice constant of the *i*th element, ΔV_{ij} is the atomic-volume change of the *i*th element dissolved into the *j*th element, respectively. According to Eq. 3.11, the intrinsic lattice distortions due to the incorporation of different size elements were calculated, using the first-principles method. The BCC NbTaTiV HEAs were modeled through the special quasi-random-structure (SQS) [76] method. Here, the intrinsic lattice distortion of the NbTaTiV alloy at zero temperature is calculated. The f_j is set to 0.25 because there are four elements, in which the composed elements are equally distributed in the HEA alloy. To calculate ΔV_{ij} and V_i, six kinds of binary systems need to be constructed, including $A_{50}B_{50}$, which denote the systems containing A and B, two of the four elements. A supercell containing 16 atoms is employed to construct the

binary systems through SQS, and the lattice vectors of the supercell are defined as $\mathrm{a} = [1\ \bar{1}\ 1],\ \mathrm{b} = [1\ \bar{1}\ \bar{1}],\ \text{and}\ \mathrm{c} = [2\ 2\ 0]$. The volumes of the six binary systems are listed in Table 3.2. The volume before alloying denotes the sum volume of all the atoms in the supercell. To calculate the volume of supercells, one needs to multiply the number of atoms by the atomic volume in Table 3.3. The volume after alloying denotes that of the supercell after optimization. Then the total volume change, ΔV, can be obtained by $\Delta V = V$(after alloying) - V (before alloying). Also, the average atomic-volume differences, ΔV_{ij}, can be calculated through $\Delta V_{ij} = \Delta V/\mathrm{N}$. Here N is equal to 8, since it corresponds to half of the number of atoms in the supercell.

According to Eqs. (3.10) and (3.11), the lattice-distortion parameters ($\bar{u}^D$) are calculated and listed in Table 3.3. For the quantitative comparison with the experimental result, the atomic fraction, which is obtained by the APT measurement, and the lattice parameter, which is acquired from the neutron-diffraction pattern, is replaced in f_j and $\bar{d}$ factors, respectively. The obtained parameter, applying these experimentally-measured values, 0.2373 Å, is fairly close to the theoretically-calculated parameter (0.2344 Å) of the lattice distortion ($\bar{u}^D$). The detailed values of lattice constants and lattice distortions are illustrated in Table 3.3. It indicates that the homogenization treatment promotes the rearrangement of atoms as a random distribution. Hence, the crystalline lattice is distorted as the predicted value of the theoretical calculation with the homogenization treatment.

Table 3.2 The theoretical parameters (Å^3) of the six binary systems. A calculated volume before and after alloying for six binary systems, variation of volume, ΔV, and average of the volume difference, ΔV_{ij}, in the supercell.

Materials / Parameters	$Nb_{50}Ta_{50}$	$Nb_{50}Ti_{50}$	$Nb_{50}V_{50}$	$Ta_{50}Ti_{50}$	$Ta_{50}V_{50}$	$Ti_{50}V_{50}$
Volume (Before alloying)	**294.17**	**284.45**	**256.31**	**284.34**	**255.03**	**244.89**
Volume (After alloying)	**294.08**	**284.72**	**254.32**	**285.04**	**254.64**	**245.28**
ΔV	**0.0900**	**- 0.2700**	**1.9900**	**-0.7000**	**0.3900**	**-0.3900**
ΔV_{ij}	**0.0113**	**-0.0338**	**0.2488**	**-0.0875**	**0.0488**	**-0.0488**

Table 3.3 Theoretical calculations and experimental results of lattice distortions. Effective lattice constant $\left(d_i^{eff}\right)$ of each element, lattice constant ($\bar{d}$), and lattice-distortion parameter ($\bar{\mu}^D$) of theoretically-calculated results in comparison to the experimental data. Note that the experimental results are calculated, based on the chemical composition, which is obtained from the APT measurements and lattice constants that are obtained through neutron diffraction.

Elements / Parameters	Condition	Nb	Ta	Ti	V
Atomic Volume (Å^3)	-	18.36	18.40	17.23	13.43
Atomic Fraction (%)	Calculation	0.250	0.250	0.250	0.250
	Experiment	0.249	0.236	0.251	0.250
d_i^{eff} (Å)	Calculation	2.8613	2.8597	2.8611	2.6263
	Experiment	2.8558	2.8578	2.8563	2.6194
$\bar{d}$ (Å)	Calculation	2.8021			
	Experiment	2.7988			
$\bar{\mu}^D$ (Å)	Calculation	0.2344			
	Experiment	0.2373			

3.4.3 Quantitative Measurement of Lattice Distortion via First-principles Calculation

The mean-field lattice-distortion parameter is somewhat ambiguous in determining the local atomic displacement. To quantitatively understand the local lattice distortion of the BCC NbTaTiV HEA system, the distribution of atomic distances in a relaxed 64-atom NbTaTiV SQS was analyzed and shown in Figure 3.7(a). It illustrates that the interatomic distance of all *n*th nearest-neighboring (NN) pairs extends over a wide range, suggesting that many of the atoms deviate profoundly from their ideal lattice sites, leading to a severe local lattice distortion in this alloy system. The average interatomic distances of atomic pairs are r = 2.80, 3.23, 4.57, 5.42, and 6.47 Å for the first to fifth NN pairs, respectively. The effects of the local atomic relaxation can be excluded if we fix the atomic positions at the BCC lattice and only optimize the volume of the SQS. In such a case, the interatomic distances, rather than showing a wide spread, exhibit single values with r = 2.80, 3.24, 4.58, 5.37, and 5.61 Å for the first to fifth NN pairs. For the short-range pairs, the average NN distances from the SQS are similar to the ideal BCC lattice. However, the deviation in average interatomic distances from an ideal BCC lattice for the 4NN and 5NN is noticeable. These results suggest that while the BCC lattice is maintained on average for the NbTaTiV HEA, a severe lattice distortion is predicted to be noticeable over longer ranges of atomic distances.

The BCC NbTaTiV system has ten different types of atomic pairs, i.e., the homoatomic pairs of Nb-Nb, Ti-Ti, Ta-Ta, and V-V, and the heteroatomic pairs of

Nb-Ti, Nb-Ta, Nb-V, Ti-Ta, Ti-V, and Ta-V. Figure 3.7(b) presents the NN interatomic distance of the aforementioned pairs in the SQS after the structural optimization. Additional DFT calculations were performed for the homoatomic and heteroatomic pairs with BCC and B2 crystal structures, respectively, to obtain the reference bond length for the interatomic pairs. These calculations provide comparable bond lengths for the atomic pairs in the BCC HEA. The mean and median of the interatomic distance of each pair are also shown in Figure 3.7(b). The interatomic distance of all 1NN pairs spreads in wide ranges. Considering both the range of the interatomic distances and the mean value of a pair, a large number of atoms in the SQS shift strongly away from their ideal lattice sites, indicating a severe local lattice distortion in the NbTaTiV system. The lattice distortions can be defined as the change of the bond length with respect to the reference bond length:

$$Lattice\ distortion = \frac{|d_i - d_r|}{d_r} \times 100 \tag{3.12}$$

where d_i is the interatomic distance of a pair in the relaxed SQS, and d_r is the interatomic distance obtained for a pair with a BCC or B2 structure. Using this formula, the largest lattice distortion pairs are V-V and Ti-Ti, which are 4.7% and 5.1%, respectively. Among the heteroatomic pairs, the largest lattice distortions are the Nb-V and Ti-V pairs with a lattice distortion of 6.1% and 8.1%, respectively. Figure 3.7(b) illustrates how likely an atomic pair is compressed or elongated in the HEA. When the median bond length is less than the reference bond length of a pair, e.g., Nb-Nb, the bond is more likely to be under compression. The homoatomic pairs between Nb-Nb and Ta-Ta, the largest atoms of the HEA are

mostly compressed, while the pairs of V-V, the smallest atom of the HEA are mostly elongated. On the other hand, in heteroatomic pairs, Ti atoms in combination with Nb and Ta appear to be balanced with their neighboring atoms on average. The heteroatomic pairs, with the V atoms, show mostly elongation in their bond lengths. The compression/tension behavior in the bond lengths can be referred to the local environment of a pair, where placing some of the atoms in its neighborhood induces compression or tension to its bond. For example, while most of the Nb-Nb pair bonds are under compression in the HEA system, some of the Nb-Nb pair bonds are elongated due to the existence of V atoms in its first nearest neighboring environment as shown in Figure 3.7(c). In addition to the difference in the atomic size, the change in the bond length of the HEA is also related to the chemical interactions among the principal elements.

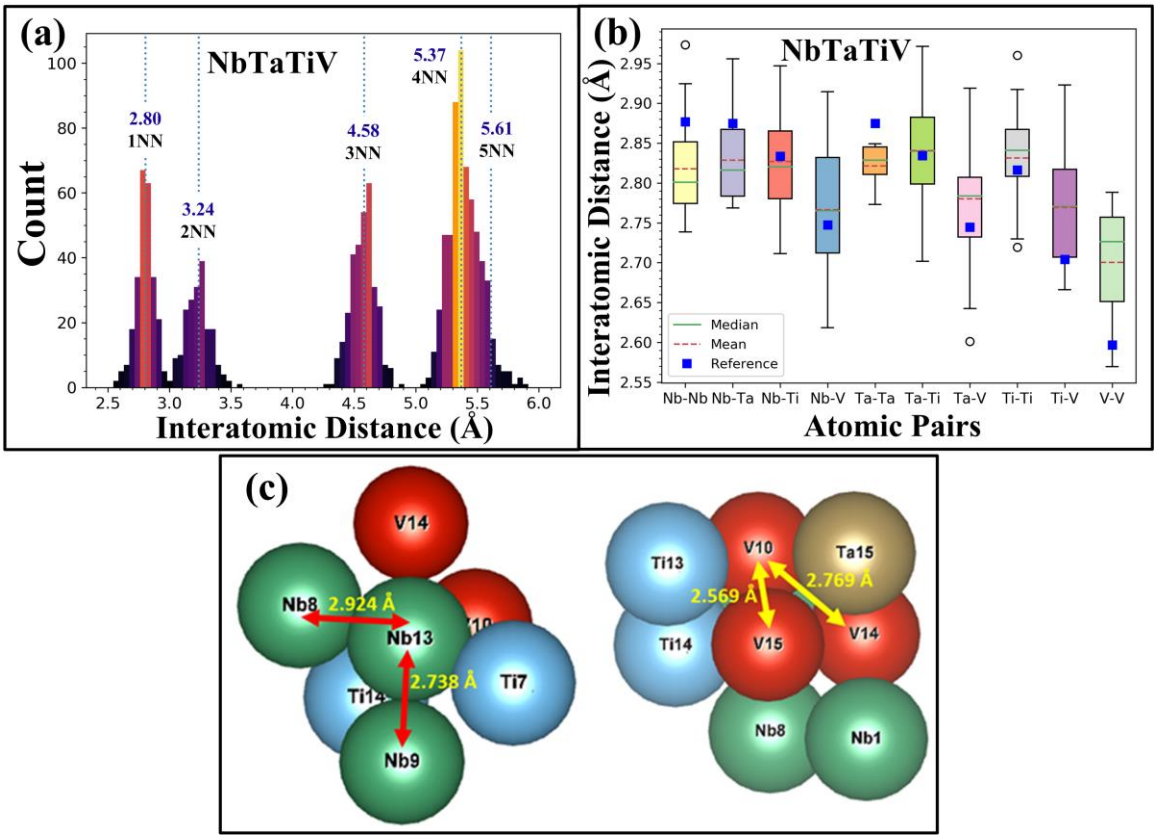

Figure 3.7 First-principles calculation data. (a) Distribution of the interatomic distances for the first to fifth nearest neighbors (NN) of the BCC NbTaTiV HEA calculated from the optimized SQS. The blue dashed lines show the average interatomic distances for the first to fifth NNs, and (b) Box plot presenting the distribution of interatomic distances of 1NN bonds in the SQS for the BCC NbTaTiV HEA. The box presents the first and third quartiles of the bond lengths for a type of atomic bonds. (c) Two different locally-relaxed atomic structures of the BCC NbTaTiV HEA. The shortest and longest bond lengths of the Nb-Nb and V-V pairs for the first nearest neighbors in the supercells with the SQS model.

3.4.4 Comparison of the Temperature Dependence of Yield Strengths

Figure 3.8 shows the yield strengths of the NbTaTiV refractory HEA and two reported refractory HEAs [10], and conventional alloys, such as the Al-based alloy [35], Ti-based alloy [77], and Ni-based superalloys [10] at high temperatures. Compared with refractory HEAs, other alloys show a drastic decrease of the yield strength at certain temperatures. The Inconel 718, which maintains higher yield strengths at elevated temperatures, as compared with other conventional alloys, exhibits a rapid decline of the yield strength around 700 °C. However, the refractory HEAs, NbTaTiV, MoNbTaW, and MoNbTaVW, present no substantial reduction of yield strengths as a function of temperatures. Besides, the values of yield strengths for NbTaTiV and MoNbTaVW alloys are much higher than other alloys at the temperatures above 800 °C. The ability of the material to retain its strength at high temperatures could be the consequence of the sluggish diffusion [78]. The nature of the slower diffusion of elements at higher temperatures in the single BCC structural refractory HEAs may arise from its structure, which consists of multi-principal elements (that possess the high melting temperature and different atomic radii) [79]. Thus, these trends can lead to the strong resistance of high-temperature softening.

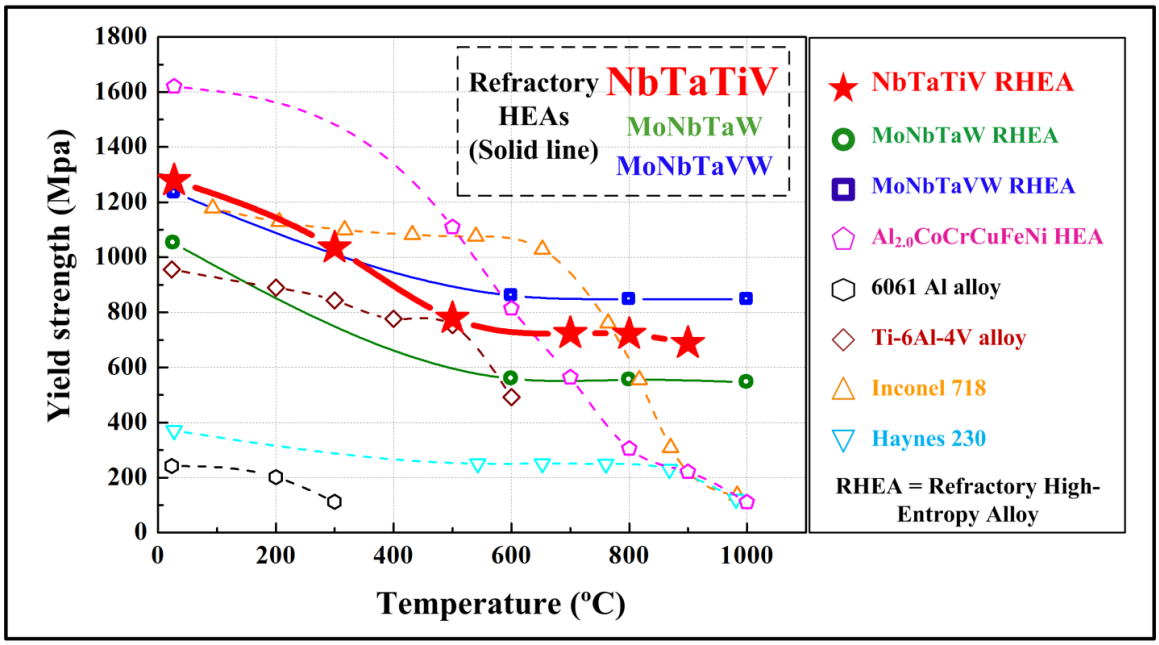

Figure 3.8 Comparison of the temperature dependence of yield strengths. Yield strengths of the NbTaTiV alloy and two reported refractory HEAs (MoNbTaW and MoNbTaVW), conventional HEA ($Al_{2.0}$CoCrCuFeNi), Al-based alloy (6061 Al alloy), Ti-based alloy (Ti-6Al-4V alloy), and Ni-based superalloys (Inconel 718 and Haynes 230) as a function of temperature.

3.5 Conclusions

Overall, this comprehensive study provides a method of the design and development of the single-phase BCC solid-solution phase refractory HEA, using an integrated experimental and theoretical thermodynamic-calculation approach. The results of the APT measurement and the neutron-diffraction patterns indicate that the structure is composed of a single-phase BCC solid solution as well as a homogeneous elemental distribution with equimolar ratios. Furthermore, the mechanical-test results of the homogenization-treated sample show the excellent yield strength and plasticity at RT as well as elevated temperatures. The dominant strengthening mechanism was found to be solid-solution hardening, which stems from the distortion of the crystalline lattice during deformation. It is thought that this strengthening mechanism induces slow elemental diffusion at high temperatures, which, consequently, leads to the strong resistance of high-temperature softening. The distorted lattice for this alloy system was quantitatively calculated by the mathematical computation and theoretical modeling, such as first-principles calculations. The results of the above modeling and analysis indicate that the local severe lattice distortions are induced, due to the atomic-size mismatch and local atomic interactions in the homogenization-treated NbTaTiV refractory HEA. These results provide (1) a novel alloy-design strategy, (2) a fundamental understanding of the lattice-distortion effect on mechanical properties, and (3) a road map to produce better materials for high-temperatures applications.

CHAPTER FOUR

TEMPERATURE DEPENDENCE OF ELASTIC AND PLASTIC DEFORMATION BEHAVIOR OF A DUCTILE REFRACTORY HIGH-ENTROPY ALLOY

4.1 Introduction

High-entropy alloys (HEAs) were defined as single-phase solid-solution alloys, composing of four or more principal metallic elements based on the new alloy-design strategy with increasing the configurational entropy (> 1.5R, R is gas constant) [1-7, 24, 66, 79]. The minimization of the Gibbs free energy by increasing the configurational entropy results in the formation of the single solid-solution phase, instead of intermetallics or multi-phases, such as body-centered-cubic (BCC) [9-12], face-centered-cubic (FCC) [8], and hexagonal-close-packed (HCP) solid-solution phases [13, 14, 80]. Moreover, the uniform distribution of multiple elements with the different atomic radii leads to severely-distorted lattice with various interatomic distances along the crystallographic direction in unit cells [24-26, 81-83]. These features, in turn, arouse unusual mechanical properties, such as the high hardness, strength, ductility, and softening resistance at room and elevated temperatures [82].

Especially, refractory HEAs, which mainly consist of the simple BCC solid-solution phase, possess the exceptional high yield strength and hardness, compared to Ni-based superalloys at elevated temperatures. For example, NbMoTaW,

NbMoTaVW, and NbTaTiV refractory HEAs present not only the higher yield strength than conventional alloys at room temperature but also no significant reduction of strengths at temperatures above 800 °C with the excellent phase stability [10, 82]. In order to identify the origin of their unique mechanical properties, significant theoretical efforts have been conducted to verify the mechanical mechanism, considering the elastic and plastic deformation fashion in the BCC refractory HEAs [20, 84]. However, it is still unclear to establish the link between unique microstructure and outstanding mechanical properties due to the lack of the experimental verification of suggested deformation theories, such as elastic isotropic deformation behavior [20, 84].

Different from the conventional alloys, the atomic deviation from their neutral positions gives rise to the various bond lengths and atomic interactions in the unit cell of HEAs. Thus, the above characteristic of unusual atomic arrangement may indicate the unique elastic and plastic deformation behaviors at room and elevated temperatures, compared to conventional BCC alloys.

Recently, Tian *et al*. [84] suggested the alloy-design strategies to develop the elastic isotropic HEAs ($TiZrNbMoV_x$ systems), using the state-of-the-art ab-initio simulation. According to their calculations, the $TiZrNbMoyV_x$ [(x, y) are (0, 0.9) and (0.5, 0.8)] refractory HEAs exhibit the elastic-isotropic deformation behavior, and it is strongly correlated to the value of the valence electron concentration (VEC) [84-86]. Furthermore, they provide the criteria of single-crystal elastic constants to evaluate the brittle-ductile behaviors, predicting that a few BCC HEA systems can

be ductile [87-91]. However, these theoretical calculation methods to design the elastically-isotropic and ductile BCC HEAs are still under debate, due to the lack of experimental validations to date [20, 84]. In order to demonstrate the unusual deformation behaviors, which is predicted by the above extensive computational simulations, we investigated the elastic- and plastic-deformation behaviors for the NbTaTiV BCC refractory HEA at room and elevated temperatures, using in-situ neutron experiments and theoretical approach. Different from the conventional BCC alloys [61, 92], the features of lattice strain evolutions and measured elastic moduli indicate the elastically-isotropic behavior at room temperature. The magnitude of single-crystal and bulk elastic moduli, which are obtained by in-situ neutron experiments are quantitatively compared to theoretical calculation results, such as first-principles calculation. Furthermore, it is found that the elastic isotropic-anisotropic transition occurs at about 700 °C, indicating the strong texture effects at high temperatures.

The excellent ductility of the present refractory HEA can be predicted by the correlation between polycrystalline elastic moduli, such as the Cauchy pressure ($C_{12} - C_{44}$) [89], Pugh ratio [bulk modulus (K) / shear modulus (G)] [88, 91], and Poisson' ratio (v) [90]. Moreover, we investigated the type of mobile dislocations, using the neutron diffraction peak broadening modeling and analysis employing the Williamson-Hall plot method, experimentally verified by the high-angle-annular-dark-field (HAADF) scanning-transmission-electron-microscopy (STEM) technique. It is found that the type of dominant mobile dislocations could be edge

dislocations, during plastic deformation, which is different from the conventional BCC metals. These new discoveries of the unique elastic and plastic deformation behaviors of the NbTaTiV refractory HEA will facilitate the development of the possible alloy systems for structural-materials applications.

4.2 Experiment

4.2.1 Materials Preparation and Microstructural Characterization

The alloys were synthesized by arc-melting under the argon atmosphere on a water-cooled Cu hearth from Nb, Ta, Ti, and V elements of 99.99 weight percent (wt. %) purity. The nominal composition of the present alloy is $Nb_{25}Ta_{25}Ti_{25}V_{25}$ in the atomic percent (at. %). In order to ensure a fully-homogeneous distribution of elements, the ingot was melted over 10 times. From the master alloys, the specimens were fabricated, followed by direct casting into cylindric rods with a 4-mm diameter and 50-mm length, using a drop-casting technique. These alloys were sealed with the triple-pumped argon in quartz tubes and homogenized at 1,200 °C for 3 days, followed by water cooling. The microstructure was examined by scanning-electron microscopy (SEM), using a Zeiss Auriga 40 equipped with back-scattered electrons (BSE). The chemical analysis of the alloy was studied by the energy-dispersive X-ray spectroscopy (EDS) after the homogenization treatment.

4.2.2 In-situ Neutron Diffraction Experiments

The in-situ neutron-diffraction (ND) measurements were carried out on the VULCAN Engineering Diffractometer at the Spallation Neutron Source (SNS) facility located at the Oak Ridge National Laboratory (ORNL) [49, 50]. The ND instrument utilizes the time-of-flight (TOF) measurements, which allows for the development of neutron-diffraction pattern, covering a wide range of d spacings without the rotation of detectors or samples. The two detectors, which designated as Banks 1 and 2 at +/-90 degrees, were employed to collect diffracted neutrons from the polycrystalline grains with lattice planes parallel to the axial and transverse directions, respectively. The compression experiments on homogenization-treated NbTaTiV alloy with a diameter of 4 mm and length of 8 mm were conducted to investigate the elastic and plastic deformation behaviors at room and elevated temperatures, using a mechanical-testing system (MTS) load frame. The samples are illuminated by the incident neutron beam of a 3 × 3 mm^2 slit size and 2-mm receiving collimators. During the measurement of the diffraction patterns for the elastic deformation period, a stepwise-force control sequence was utilized. The measurement time of the neutron-diffraction data was 20 minutes at each stress level. When the stress level reached 1,100 MPa for RT, 750 MPa for 700 °C, and 620 MPa for 900 °C (close to the macroscopic yield strength), a stepwise displacement control with an incremental step of 0.2 mm employed. The collected data were analyzed by single-peak fitting, using the VULCAN Data Reduction and Interactive Visualization software (VDRIVE) program [51].

4.2.3 First-principles Calculations

First-principles calculations were performed with the Vienna Ab-initio Simulation Package (VASP) [52, 96], using the projector augmented wave (PAW) method [97]. The exchange-correlation energy was described with the generalized gradient approximation (GGA) in the Perdew-Becke-Ernzehof (PBE) parameterization [55]. A plane-wave cutoff of 700 eV and Monkhorst-Pack k-point grid of 4 × 4 × 4 was used for all calculations. The chemical disorder of the solid solution was modeled using a 64 atom Special Quasirandom Structure (SQS) [43]. The SQS was employed, using a method based on a Monte Carlo-simulated annealing loop where atomic configurations are proposed by randomly swapping atomic positions and accepting changes when the configuration's calculated correlation functions are a closer match to that of a disordered state [76].

The elastic tensor of the SQS supercell was calculated, using a set of distorted structures based on the methodology described in [98]. The supercell's lattice parameters were fixed at the experimentally determined room temperature values, and the ionic positions were allowed to relax. A set of deformed structures were generated using 3 × 3 Green-Lagrange strain tensors of varying magnitudes at ± 0.5% and ± 1%. For each distorted structure, the 3 × 3 stress tensor is computed by the density functional theory (DFT). A linear least-squares fit between the stress and strain tensors was performed to calculate the elastic tensor of the SQS. However, since the SQS supercell does not conserve the point-group symmetry, a projection technique is used to derive the closest elastic tensors with cubic

symmetry for the NbTaTiV alloy [99], which is equivalent to crystallographically-averaging tensor elements. The projection method is a computationally-efficient and the elastic constant values converges quickly with the size of SQS. The elastic moduli of current HEA are calculated, using the elements of the projected elastic tensor as described below. The bulk modulus (*K*), shear modulus (*G*) were obtained, considering Voigt-Reuss-Hill averaged, then young's modulus was mathematically calculated, substituting of *K* and *G* in simple equation ($E = \frac{9KG}{3K+G}$), which considered the correlation between *E*, *K*, and *G*.

$$K = \frac{5}{(s_{11}+s_{22}+s_{33})+2(s_{12}+s_{23}+s_{31})} \tag{4.1}$$

$$G = \frac{15}{4(s_{11}+s_{22}+s_{33})-4(s_{12}+s_{23}+s_{31})+3(s_{44}+s_{55}+s_{66})} + \frac{(s_{11}+s_{22}+s_{33})-(s_{12}+s_{23}+s_{31})+3(s_{44}+s_{55}+s_{66})}{15} \tag{4.2}$$

where s_{ij} is the stiffness tensor, and the elastic tensor C_{ij} was calculated, following their correlation $s_{ij} = C_{ij}^{-1}$.

4.3 Results

4.3.1 Formation of the Single BCC Solid Solution and Its Mechanical Properties of the Homogenization-treated NbTaTiV HEA at Elevated Temperatures

Figure 4.1(a) shows the scanning-electron microscopy (SEM) back-scattered electrons (BSE) images of the homogenization-treated NbTaTiV refractory HEA. The simple solid-solution microstructure was clearly observed with no formation of second phases or elemental segregation within grains and grain boundaries. The

chemical composition of the homogenization-treated sample was identified by the point EDS analysis, which is close to the nominal composition ($Nb_{23.8}Ta_{25.5}Ti_{24.9}V_{25.8}$, the average of the atom fractions). The measured ND patterns of the bulk samples prove the single BCC solid solution at room as well as elevated temperatures, as illustrated in Figure 4.1(b). The averaged lattice parameters of the present alloy at RT, 700 °C, and 900 °C, which were determined by a single-peak fitting approach [51], are 3.2318 ± 0.0001, 3.2511 ± 0.0002, and 3.2588 ± 0.0003 Å, respectively. It is seen the single BCC phase is presented up to 900 °C, indicating the excellent phase stability at elevated temperatures. Figure. 1(c) exhibits the nominal compressive true stress-strain curves of the homogenization-treated NbTaTiV alloy at RT, 700 °C, and 900 °C with an estimated-strain rate of 1×10^{-4} s^{-1}, which are directly obtained from the in-situ neutron measurement. The yield strengths (σ_y) and work-hardening exponent (*N*) of the present alloy gradually decrease from 1,146 MPa (RT) to 627 MPa (900 °C) and from 0.2732 (RT) to 0.1199 (900 °C), respectively. The working-hardening exponents (*N*) were estimated with the Holloman equation [100]:

$$\sigma_t = k\varepsilon_t^N \tag{4.3}$$

where σ_t is the true applied stress, *k* is the strengthening coefficient, and ε_t is the true plastic strain. During plastic deformation, the applied load slightly relaxes, while the neutron-recording time (about 20 mins) with a constant displacement-control mode at 700 °C. Moreover, this relaxation behavior becomes more severe

at 900 °C (about 440 – 580 MPa) than 700°C (about 130 – 260 MPa), as shown in Figure 4.1(c).

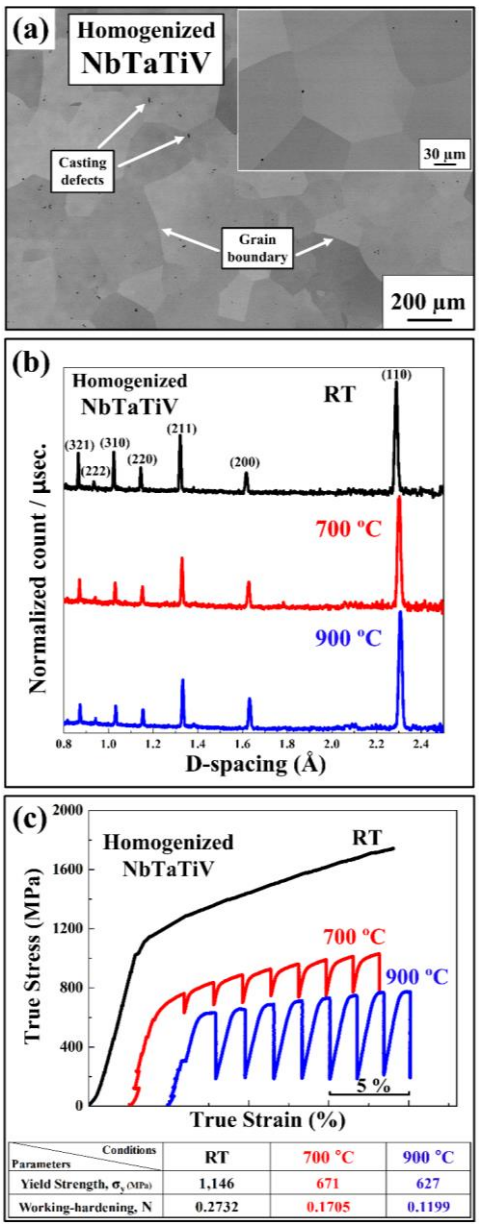

Figure 4.1 Microstructural, phase characteristics, and mechanical properties of the homogenized NbTaTiV alloy, studied by SEM, neutron diffraction (ND), and nominal compressive true strain-stress curves during in-situ ND experiments at elevated temperatures. (a) SEM-BSE image of the homogenization-treated NbTaTiV refractory HEA. (b) neutron-diffraction patterns with the peaks indexed for a BCC structure at RT, 700 °C, and 900 °C, respectively. (c) True stress-strain curves recorded during in-situ compression experiment at RT, 700 °C, and 900 °C with a strain rate of 1×10^{-4} s^{-1}.

4.3.2 Lattice-strain Evolutions of the Homogenized NbTaTiV HEA at Room and Elevated Temperatures

The in-situ ND with compression tests on the homogenization-treated NbTaTiV alloy were carried out to investigate the elastic and plastic deformation behaviors for differently oriented grains along the loading and transverse directions. Figure 4.2 reveals the corresponding lattice-strain evolutions of {110}, {200}, {211}, and {310} planes, as a function of applied stresses at RT. The lattice strains (ε_{hkl}) were calculated from the variation of the diffraction peak position, during loading by the following equation:

$$\varepsilon_{hkl} = \frac{d_{hkl} - d^0_{hkl}}{d^0_{hkl}} \quad (4.4)$$

where d_{hkl} is the *hkl* lattice spacing as a function of the applied stress, and d^0_{hkl} is the reference *hkl* lattice spacing under the unloaded state. The lattice-strain evolution can provide the {*hkl*} plane-specific lattice strain during deformation. The evolution of lattice strains in the elastic region exhibits that the change of lattice strains is not dependent on the grain orientation, i.e., all oriented-grains [{110}, {200}, {211}, and {310}] exhibit almost the similar diffraction elastic constants (the slope) due to the elastic isotropy. The change of the slopes happened around 1,100 MPa, as a result of elastic-plastic transition. Furthermore, no significant load transfer is observed from grain to grain, which is manifested by the small deviation of slopes, during plastic deformation.

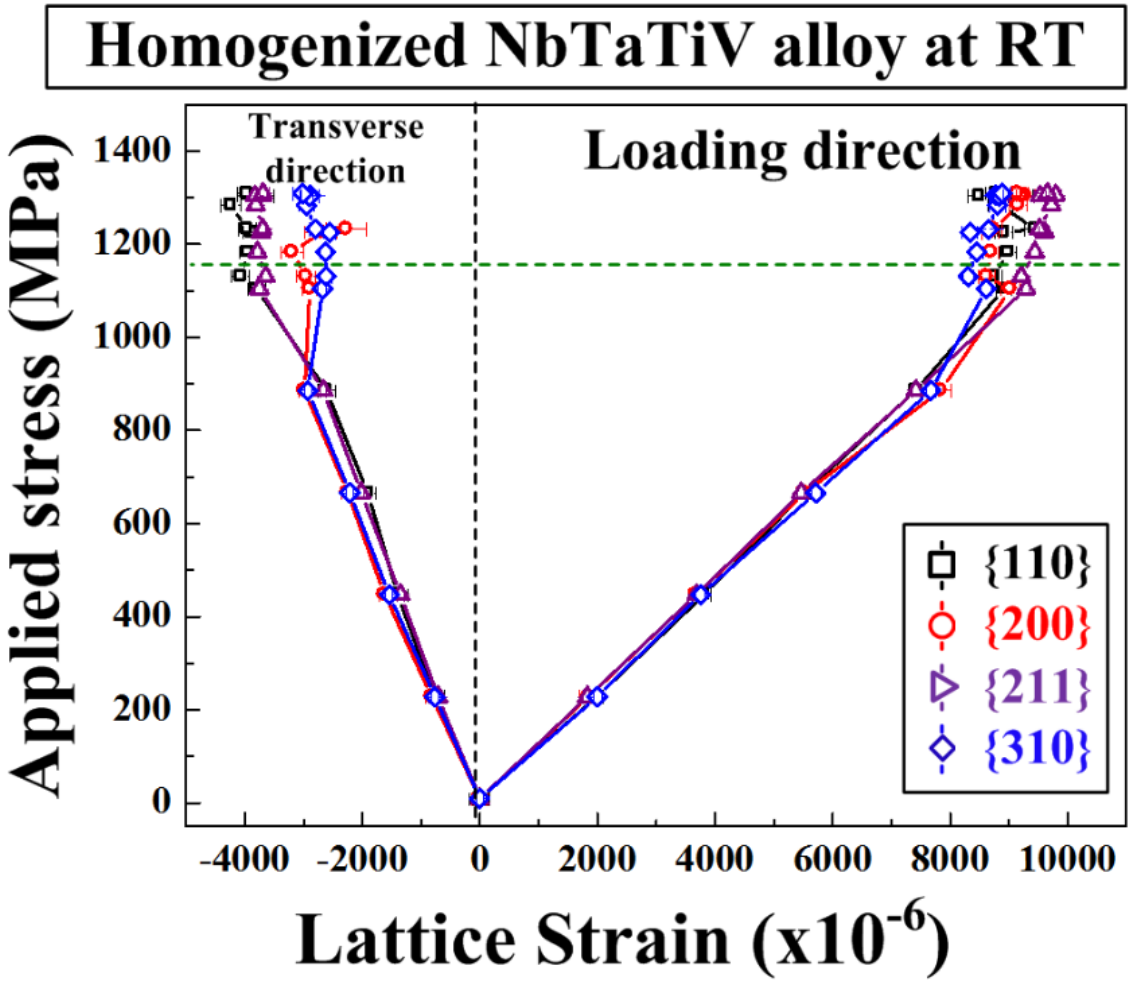

Figure 4.2 Lattice-strain evolution in the NbTaTiV refractory HEA as a function of applied stress, obtained from the in-situ ND experiments at RT. The corresponding lattice-strains of {110}, {200}, {211}, and {310} orientation planes along the axial and transverse direction at RT as a function of applied stress during the elastic and plastic deformations. The onset of yielding is marked as the green dot line.

Figure 4.3(a-c) present the lattice-strain evolution along the axial and transverse directions during elastic deformation, respectively, as a function of the applied stress at various temperatures (RT, 700 °C, and 900 °C). Different with the feature of the lattice-strain evolution at RT, which exhibits the elastically-isotropic deformation Figure 4.2 and Figure 4.3(a)], the different slopes of the lattice strain are observed due to increased elastic anisotropy, as shown in Figure 4.3(b) and (c). Note that the elastic anisotropy behavior was not apparently observed, during deformation at 500 °C (not shown). It can be found that the elastic characteristic may transit from the isotropy to anisotropy in a certain temperature range about 700 °C. At higher temperature, while the overall stiffness reduces, the anisotropy increases. More detail in the grain level, the {200}-oriented grain shows the largest elastic lattice strain with lowest stiffness, and the {310} grains have the second largest elastic strain with nearly a linear response. Whereas, the {110} and {211} grains exhibit the lower lattice strain and higher directional strength-to-stiffness ratio. The diffraction elastic moduli, E_{hkl}, of different crystallographic planes at elevated temperatures are listed in Table 4.1, and it shows the subequal values of elastic moduli in different orientations. This trend indicates that NbTaTiV HEA exhibits the unique elastic-deformation behavior at RT as an elastic isotropy. Besides, it transfers to the severe elastic anisotropy at high temperatures, which is usually observed from the conventional BCC structure alloys at RT [61, 92, 101].

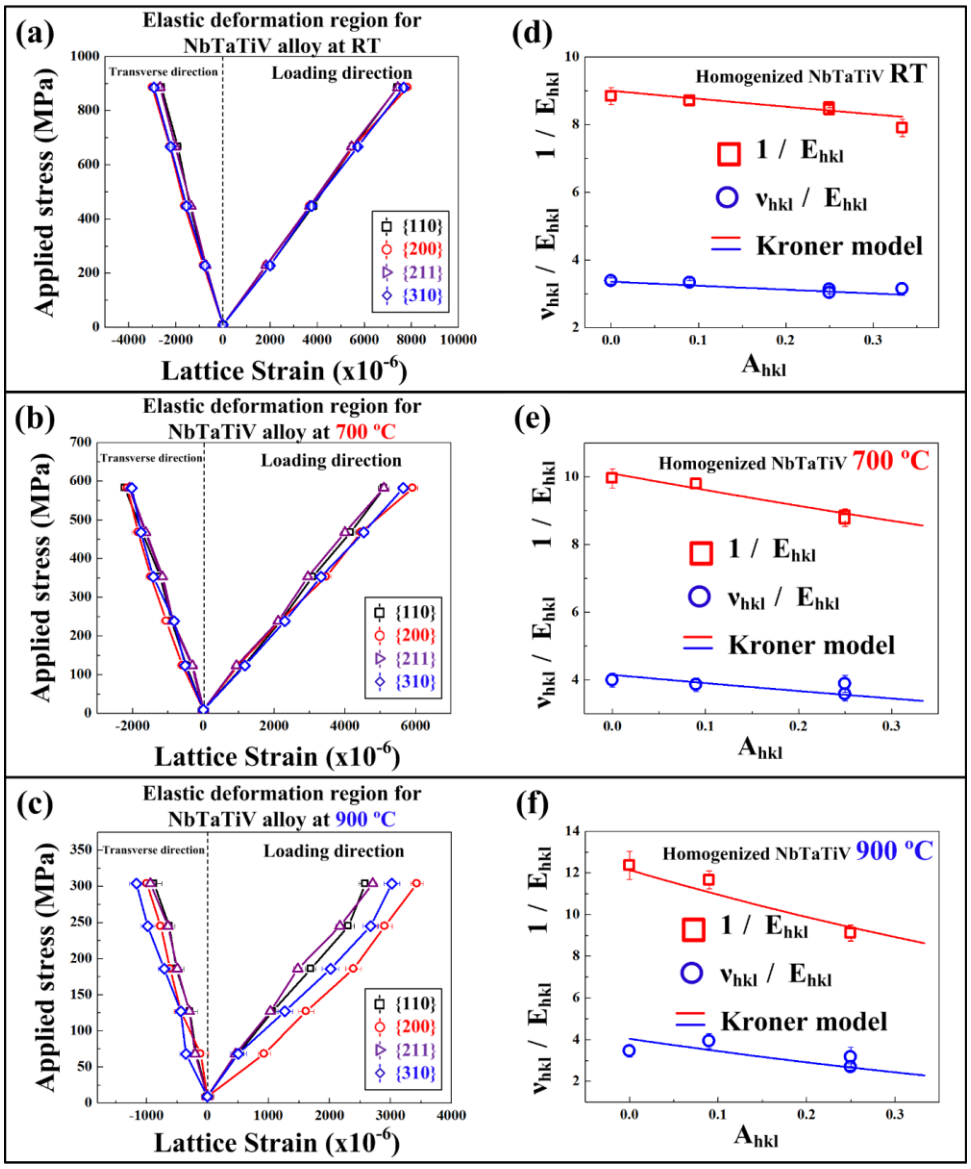

Figure 4.3 Lattice-strain evolution in the NbTaTiV refractory HEA as a function of applied stress, obtained from the in-situ ND experiments during elastic deformation and plots of elastic moduli of different oriented crystals as a function of the elastic-anisotropy factor and fitting with the Kroner model at RT, 700 °C, and 900 °C. The corresponding lattice-strains of {110}, {200}, {211}, and {310} orientation planes along the axial and transverse direction during the elastic deformation (a) RT, (b) 700 °C, and (c) 900 °C, respectively. The reciprocal diffraction elastic moduli, ($1/E_{hkl}$ and ν_{hkl}/E_{hkl}), as a function of the elastic-anisotropy factor, A_{hkl}, ($\frac{h^2k^2+k^2l^2+l^2h^2}{(h^2+k^2+l^2)^2}$), which are obtained from the experimental elastic lattice-strain (symbols) and fitted by Kroner models (solid lines) at (d) RT, (e) 700 °C, and (f) 900 °C, respectively.

Table 4.1 The elastic moduli, E_{hkl}, of different crystallographic planes for the homogenized NbTaTiV alloy at elevated temperatures. Elastic moduli of {110}, {200}, {211}, and {310} at RT, 700 °C, and 900 °C are obtained from in-situ neutron diffractions.

Parameters / Conditions	Diffraction elastic modulus E_{hkl} (GPa)				FEM elastic modulus E_{hkl} (GPa)			
Planes	**{110}**	**{200}**	**{211}**	**{310}**	**{110}**	**{200}**	**{211}**	**{310}**
RT	**122.5**	**115.9**	**121.7**	**117.9**	**121.4**	**120.2**	**121.4**	**120.4**
700 °C	**114.2**	**97.8**	**114.0**	**103.2**	**112.0**	**105.6**	**112.5**	**108.7**
900 °C	**106.9**	**84.7**	**106.7**	**90.6**	**108.5**	**90.7**	**109.3**	**99.7**

4.3.3 Quantitative Calculations of Single-crystal Elastic Moduli for NbTaTiV HEA via Kroner Model

In order to quantitatively and efficiently underlying the elastic-deformation behaviors as a function of temperature for the NbTaTiV alloy, the macroscopic elastic moduli (E_M) are obtained from the diffraction elastic moduli (E_{hkl}), using a theoretical model. The Kroner's self-consistent model, which is the most adequately applied calculation methods to determine the macroscopic elastic moduli from diffraction elastic moduli for HEA systems [102-105], was applied in the current lattice-strain evolution results.

Figure 4.3 (d-f) show the reciprocal diffraction elastic moduli ($1/E_{hkl}$ and v_{hkl}/E_{hkl}) as a function of the elastic-anisotropy factor, A_{hkl}, ($\frac{h^2k^2+k^2l^2+l^2h^2}{(h^2+k^2+l^2)^2}$), which are obtained from the experimental elastic lattice strain and calculated by the Kroner model at the room and elevated temperatures [50-53]. It is found that the theoretical Kroner model fits with the experimental data in all temperature ranges. Based on this agreement with in-situ neutron experimental data, the single-crystal elastic constants, C_{ij}, macroscopic bulk modulus (K_M), and shear modulus (G_M) were calculated [104, 105]:

$$G_K^3 + \alpha G_K^2 + \beta G_K + \gamma = 0 \tag{4.5}$$

where GK is the diffraction shear modulus, and α, β, and γ are constants given by [104]:

$$\alpha = \frac{3\{3K_M+4[\mu+3(\eta-\mu)A_{hkl}]\}}{8} - \frac{(2\eta+3\mu)}{5} \tag{4.6}$$

$$\beta = \frac{3K_M[\mu+3(\eta-\mu)A_{hkl}]}{4} - \frac{3(6K_M\eta+9K_M\mu+20\eta\mu)}{40} \quad (4.7)$$

$$\gamma = -\frac{3K_M\eta\mu}{4} \quad (4.8)$$

where K_M is the bulk modulus, which is given by (C_{11} + 2C_{12})/3, η is (C_{11} - C_{12})/2, and μ is equal to C_{44}. The value of the isotropic macroscopic shear modulus, GM, becomes diffraction shear modulus, G_K, in Eq. (4.5), by substituting 0.2 for Ahkl. Then, the isotropic macroscopic Young's modulus, EM, can be calculated by the equation:

$$E_M = \frac{9G_MK_M}{G_M+3K_M} \quad (4.9)$$

The calculated single-crystal elastic constants, Cij, macroscopic elastic (EM), shear (G_M), bulk (K_M) moduli, and Poisson' ratio (v) at room and elevated temperatures are listed in Table 4.2. As the temperature increases up to 700 °C, the variation of C_{11} with temperature is found to be larger, as compared with C_{12} and C_{44}. These results can be manifested that a longitudinal strain majorly induces the change in the volume. The change of the volume is strongly associated with temperature and thus, presents a relatively-large change in C11. As a result, the tetragonal shear modulus, C' = [(C_{11} - C_{12})/2], is significantly reduced with the gradually decreasing elastic, shear, and bulk moduli. Moreover, different from the elastic constants at 700 °C, the values of C_{11} and C_{12} are drastically reduced at 900 °C but not the case for C_{44}, and this results in a small change of the tetragonal shear modulus, C'. The result implies the elastic stability of this BCC HEA against the tetragonal shear deformation.

Table 4.2 Single-crystal and macroscopic elastic constants of NbTaTiV alloy at elevated temperatures obtained from Kroner model based on in-situ neutron data (RT, 700 °C and 900 °C) and first-principles calculation (-273 °C and RT). The single-crystal elastic constants, C_{11}, C_{12}, C_{44}, macroscopic elastic (E_M), shear (G_M), bulk (K_M) moduli, and Poisson' ratio (v) at RT, 700 °C, and 900 °C are obtained from the diffraction elastic moduli, using Kroner model and theoretical calculation.

Parameters / Conditions	C_{11} (GPa)	C_{12} (GPa)	C_{44} (GPa)	C' (GPa)	E_M (GPa)	G_M (GPa)	K_M GPa)	v
First-principles calculation Results at -273 °C	211.8	131.2	31.6	43.3	97.3	34.8	158.1	0.397
First-principles calculation Results at RT	190.2	111.57	33.51	39.33	98.6	35.7	137.8	0.381
Experimental Results at RT	196.8	121.44	46.74	37.68	117.3	42.9	146.6	0.368
Experimental Results at 700 °C	184.3	122.52	45.93	30.91	107.9	39.3	143.1	0.376
Experimental Results at 900 °C	134.9	76.78	46.65	29.05	102.3	38.7	96.1	0.325

4.3.4 Predictions of Elastic Moduli for the NbTaTiV Refractory HEA via First-principles Calculations

Based on experimental observations of elastic deformation behaviors for NbTaTiV alloy, the first-principles calculations are employed to theoretically confirm the values of single-crystal elastic moduli at RT, using density functional theory. The Young's, bulk and shear moduli at -273 ºC and RT for the current HEA are quantitatively calculated by Voigt-Reuss-Hill average approach. The calculated and measured bulk elastic moduli at -273 ºC and RT are summarized in Table 4.2, indicating the good agreement with the experimental results. The relative error at RT for the derived elastic moduli were -15.9%, -16.6%, and -6.0% for the Young's, shear, and bulk moduli respectively. The calculated elastic moduli at RT were systematically smaller than experimentally measured values. The calculated elastic constant values for C_{11}, C_{12}, and C' all decrease from -273 ºC to RT; an exception is C_{44} which hardly changes with an increase from 31.6 GPa to 33.51 GPa. The stiffness of metals is expected to decrease with temperature and this is seen in the general trend, comparing calculated elastic constants at -273 ºC and at RT.

The FCC structured CoCrFeMnNi HEA shows a strong temperature dependence of yield strength, which is predicted by theoretical calculations. However, the temperature dependence experimentally measured shear strength was found to be very weak; from 55 K to 300 K the shear modulus only changes from 86 GPa to 80 GPa (a decrease of 7%) [106]. Another study of the CoCrFeMnNi HEA

observed Young's and shear modulus dependence on temperature between 200 K and 1,000 K. Both moduli decrease monotonically with increasing temperature, and this study also found that the shear modulus dependence on temperature was relatively weaker, decreasing only 26 GPa over an increase of 800 K [107]. The mechanical behavior such as strength or shearing reflects atomic bonding and how electron density responds to an applied strain [108]. The shear modulus is isotopic, which implies isotropic bonding charge density or bonding of a metallic nature. Thus, while the bond strength of the HEA may have a strong temperature dependence, the metallic bonding nature makes it, so the shear modulus has a weaker temperature dependence.

The elastic properties of the NbTaTiV HEA was analyzed and plotted with respect to crystallographic orientation as illustrated in Figure 4.3. To compute the direction dependent elastic properties, tensorial operations were applied to the fourth order elastic tensor determined from the DFT calculations described above. The fourth order elasticity tensor is transformed in a new basis set to determine elastic properties in any direction using the equation below.

$$C'_{\alpha\beta\gamma\delta} = \lambda_{\alpha i}\lambda_{\beta j}\lambda_{\gamma k}\lambda_{\delta l}C_{ijkl} \tag{4.10}$$

where each λ is a direction cosine of the angle between the rotated and reference axes [109].

A higher degree of isotropic elastic property results in less variation in the magnitude of the 3D surfaces and 2D contours. The 2D contour plots correspond

to a cut through the 3D surface plots at the XY, XZ, and YZ planes. The Young's modulus is represented above by a solid surface with a color map in which darker colors represent smaller values and brighter colors represent larger values. The anisotropy in Yong's modulus values as the ratio of the maximum to minimum Young's modulus value is 1.16, indicating the significant small anisotropy characterization. The maximum is in the <100> directions with a value of 107.7 GPa and the minimum is in the <111> directions with a value of 93.0 GPa, respectively, as shown in Figure 4.4(a) and (b). The 3D surface plot for linear compressibility is a translucent green sphere which shows no anisotropy at all as it has a value of 2.42 TPa^{-1} in all directions [Figure 4.4(c) and (d)]. Furthermore, the detailed behavior of the shear modulus and Poisson's ratio over all directions of applied stress is represented by plotting separate surfaces for maximum and minimum values. Note that the shear modulus and Poisson's ratio cannot be represented by a single surface as they depend on both the direction of applied stress and a measurement direction, which is perpendicular to the first [110]. In the 3D surface plots of the shear modulus and Poisson's ratio, the translucent green surface represents the maximal values and envelopes the solid surface inside which represents the minimal values. The minimum surface has a color-map applied such that darker colors represent smaller values than brighter colors, as illustrated in Figure 4.4(e) and (g). In the 2D plots, the maximum values are represented by a green curve, and the minimum values are represented by a pink curve. The ratio of the maximum shear modulus value to the minimum value is 1.17. The maximum is in the <111> directions with a value of 39.33 GPa and the

minimum is in the <110> directions with a value of 33.51 GPa. The ratio of the maximum Poisson's ratio to the minimum ratio is 1.32. The maximum and minimum values both occur in the <110> directions with values of 0.44 and 0.33, respectively [Figure 4.4(f) and (h)].

Recently, Ranganathan *et al*. [111] introduced a measurement method of anisotropy, using the universal elastic anisotropy index, which can be generally apply to crystal systems with consideration of the bulk component of the elastic tensor. As opposed to other anisotropy measurement methods, such as the Zener anisotropy index which is only applicable to cubic crystals, and the Ledbetter-Migliori anisotropy index, which only considers the shear component of the elastic tensor, the universal anisotropy index is given by the following equation

$$A^U = \frac{5G^V}{G^R} + \frac{K^V}{K^R} - 6 \geq 0 \quad (4.11)$$

where G is the shear modulus and K is the bulk modulus, and the V and R superscripts refer to the Voigt and Reuss estimates respectively. For a basis of comparison, the A^U values of the constituent elements obtained from the Materials Project database are Nb: 2.71, Ta: 0.07, Ti: 0.27, and V: 3.42 [46]. As a result, the AU value for the NbTaTiV HEA is 0, which defines the single crystal elastic properties as isotropic.

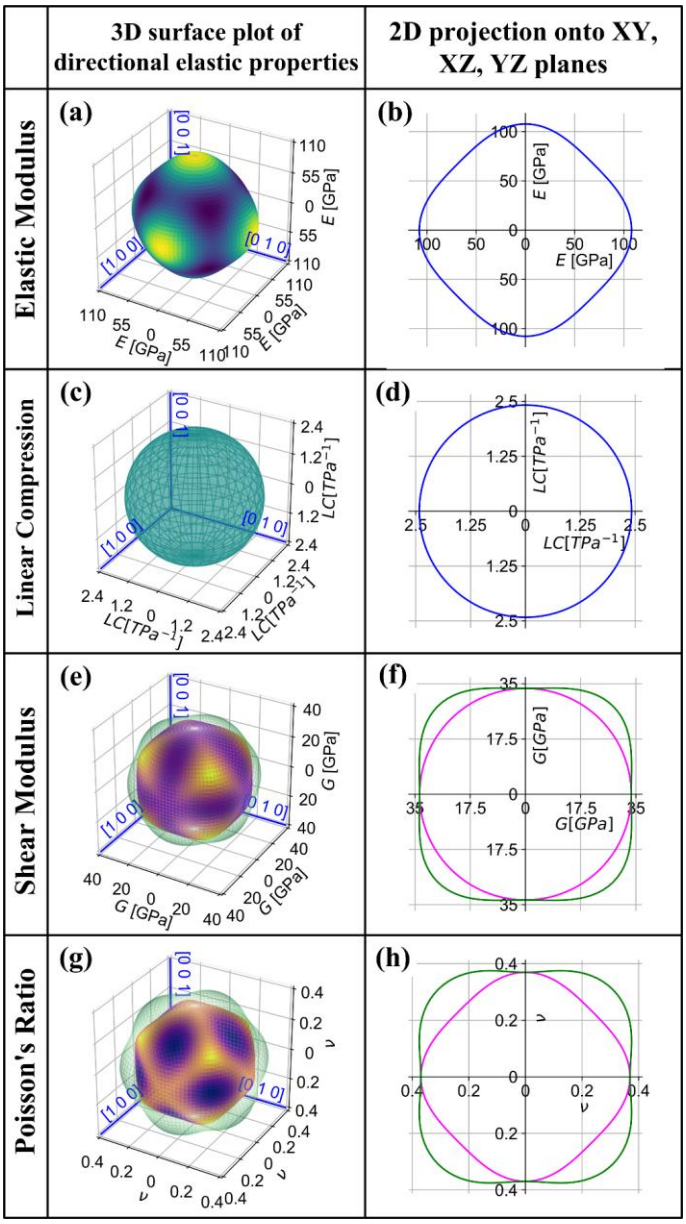

Figure 4.4 Directional dependence of first-principles calculated RT elastic properties. The magnitude with respect to direction in three dimensions for (a) Young's modulus in GPa, (b) linear compressibility in TPa^{-1}, (c) shear modulus in GPa, and (d) Poisson's ratio respectively. Shear modulus and Poisson's ratio is represented by two surfaces for maximum and minimum values. The magnitude with respect to direction on the XY, XZ, YZ planes for (e) Young's modulus in GPa, (f) linear compressibility in TPa^{-1}, (g) shear modulus in GPa, and (h) Poisson's ratio respectively. Shear modulus and Poisson's ratio is represented by two lines for maximum and minimum values.

4.3.5 Plastic-deformation Behaviors of the NbTaTiV HEA at Elevated Temperatures

Figure 4.5 illustrates the evolutions of the normalized full width at half maximum ($FWHM/FWHM_0$) of {110}, {200}, {211}, and {310} diffraction peaks as a function of macro-strain at RT, 700 °C, and 900 °C, respectively. Note that the reference full width at half maximum ($FWHM_0$) was considered as a FWHM at the initial diffraction pattern. With no significant orientation dependence, the FWHM of (*hkl*) oriented-grains substantially increased up to 1.7 during the 18 % plastic deformation at RT. When the temperature reaches 700 °C, however, the deviation of FWHM in all oriented-grains under the macro-strain of 15 % become much smaller than RT, as shown in Figure 4.5(b). The evolution of the FWHM, eventually, almost unchanged as a function of macro-strain at 900 °C, indicating the significant working softening. This trend is consistent with the decrease of working-hardening exponents (*N*) at elevated temperatures [Figure 4.1(c)]. Generally, the broadening of the diffraction peak profile at RT is significantly related to the generation of the mechanically-induced substructures and the local stress field, which are originated from intergranular stresses with dislocations and twining [62, 63]. Thus, the increase of the FWHM after yielding in this alloy system is significantly contributed from the development of the dislocation substructure, during plastic deformation with the `macrostrain of 18 %. Note that the plastic-deformation behavior of the present alloy is mainly dominated by the dislocation-slip mechanism at RT [82]. On the other hands, slight broadening of the diffraction

FWHM at 700 °C can imply that the alloy is plastically deformed by the mixture of the formation of dislocations and structural relaxation. After further increasing the temperature up to 900 °C, the structural relaxation with the dislocation creep could be dominant mechanical mechanism, which can often occur through the dislocation climb during the recovery at high temperatures [112-114]. The detailed plastic deformation mechanism with dislocation motions at elevated temperature will be discussed later.

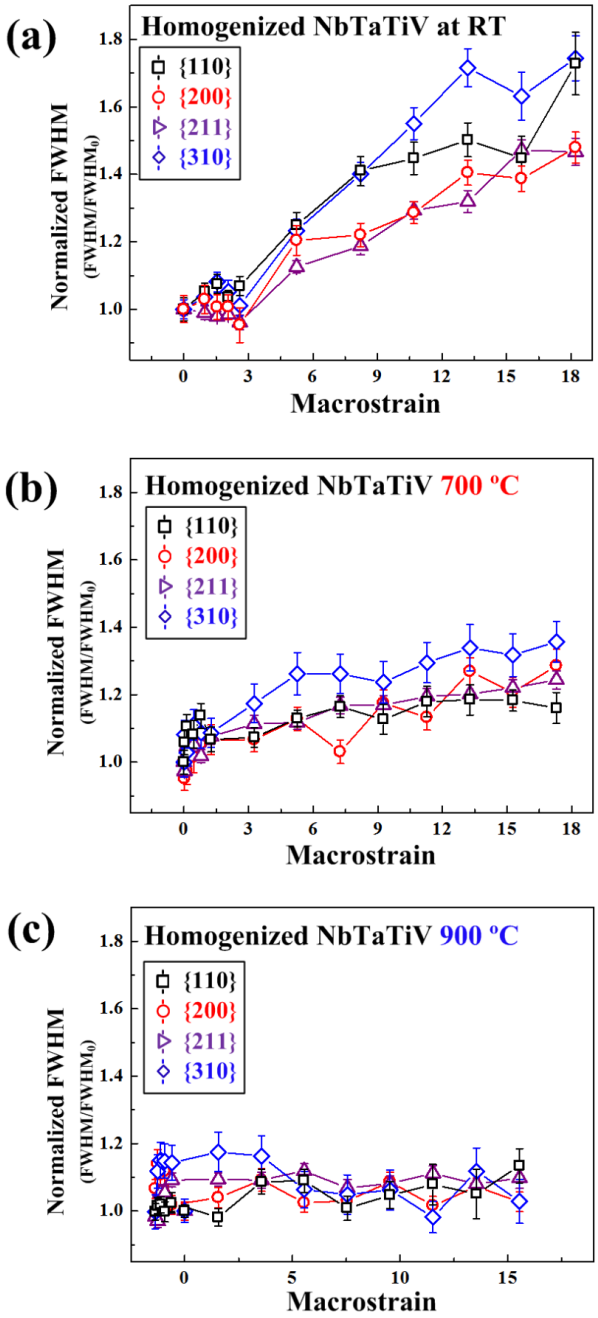

Figure 4.5 Evolution of normalized full width at half maximum ($FWHM/FWHM_0$) as a function of macrostrain for homogenized NbTaTiV alloy, obtained from in-situ neutron experiment at elevated temperatures. The evolutions of the normalized Full width at half maximum ($FWHM/FWHM_0$) of {110}, {200}, {211}, and {310} diffraction peaks as a function of macrostrain at (a) RT, (b) 700 °C, and (c) 900 °C, respectively.

4.4 Discussion

4.4.1 Elastic Isotropy and Anisotropy Deformation Behaviors of the NbTaTiV Refractory HEA

Typically, the response of lattice strains under the applied stresses is strongly associated with the oriented grains due to the effects of elastic anisotropies in polycrystalline metal materials [61, 115-119], including the FCC structured HEAs [120]. The elastically-anisotropic deformations are originated from the orientation-dependent elastic modulus, which is presented by the different slopes in the plots of the lattice-strain evolution as a function of applies stresses. In case of the BCC structural materials, the {110} and {211} oriented grains, which possess larger elastic stiffness, exhibit the larger slope. The {200} and {310} grains, on the other hands, are indicating the smaller slopes with the lower elastic stiffnesses [61, 92]. After this elastic stretch, the sequence of grain yielding depends on the value of the Schmid factor and showing the different stress levels for the onset of yielding in differently oriented grains, which is commonly characterized as the grain-to-grain yielding behaviors [92, 101, 121]. The plastic anisotropy is derived from the occurrence of the plastic deformation on certain (*hkl*)-oriented grains, which is preferred for the slip. An increase of the slope indicates plastic yielding of particularly oriented grains, whereas, the reduction of slope represents an intergranular load-transfer from the yielding grains to the neighboring grains, which are still in the elastic-deformation region. With these trends of the lattice-strain evolution, {110} and {211}-oriented grains with the largest stiffness in the elastic

region tend to yield at the early stage due to their slip system. Subsequently, a load transfers to {200} and {310}-oriented grains, resulting in an increase of lattice strains during plastic deformation. Interestingly, different with conventional BCC alloys, as discussed above, the NbTaTiV BCC refractory HEA exhibits no orientation-dependent lattice-strain evolutions during elastic deformation at RT, leading to a nearly the same values of elastic moduli in differently oriented grains. With this unusual elastic deformation, all orientated grains yield at the same stress level (around 1,100 MPa) as shown in Figure 4.2. Furthermore, the features of the load transfer were not clearly presented, indicating the less anisotropic behavior during plastic deformation at RT.

The elastic isotropy is often quantitatively described by the Zener anisotropy (A_z) ratio and Vigot and Reuss bounds (A_{VR}):

$$A_Z = \frac{2C_{44}}{C_{11}-C_{12}} \tag{4.12}$$

$$A_{VR} = \frac{G_V-G_R}{G_V+G_R} \tag{4.13}$$

where, $G_R = [5(C_{11} - C_{12})\, C_{44}] / [4C_{44} + 3(C_{11} - C_{12})]$ and $G_V = (C_{11}\text{-}C_{12} + 3C_{44}) / 5$ [122]. The calculated values of A_Z and A_{VR} at elevated temperatures can be found in Table 4.3. In case of ideal isotropic materials, the value of the tetragonal shear modulus (C') can be identical to the cubic shear modulus (C_{44}), and it results in A_z =1 and A_{VR} = 0 [20, 84]. Normally, the Zener ratio of most of conventional FCC and BCC structural materials are over the values of 2.0 or 3.0, with the significant elastic anisotropy [115, 120, 123-126]. Recently, Tian et al. suggested the alloy design strategy to perform the elastic isotropy HEAs, using ab initio calculation

[84]. It is found that Mo-contained BCC refractory HEAs have the same polycrystalline shear and Young's moduli along all orientations, indicating the elastic isotropy. Furthermore, these isotropic HEAs possess similar valence electron concentration (VEC) about 4.7, (generally, HEAs tend to form BCC solid-solution phases when VEC becomes less than 7.55) [84, 86], which are the same features with other elastic isotropy alloys, such as Ti-V alloy (Gum Metals) [127]. However, they have strongly focused on the only theoretical calculations, due to the lack of experimental verifications. According to our calculated results of A_z and A_{VR} in Table 4.3, which are basically obtained from in-situ neutron experiments, the NbTaTiV refractory HEA manifests almost the perfectly isotropic elastic deformation at RT ($A_Z \approx 1.2$, $A_{VR} \approx 0.0056$ and VEC ≈ 4.68) and gradually transfer to anisotropy at elevated temperatures. Similar to other conventional metallic alloys, the anisotropic-deformation behaviors may imply that textures play an important role in affecting the macroscopic stress at high temperatures [112, 115, 128].

Table 4.3 Elastic anisotropy factors (A_z, A_{VR} and VEC) and brittle-ductile criterion (B/G and Cauchy Pressure) for homogenized NbTaTiV alloy at RT, 700 °C and 900 °C. The calculated Zener anisotropy ratio, $A_z = [2C_{44} / (C_{11} – C_{12})]$, Vigot and Reuss bounds, $A_{VR} = (G_V – G_R) / (G_V + G_R)$, Valence electron concentration (VEC), Pugh ratio [bulk modulus (K) / shear modulus (G)], and Cauchy pressure ($C_{12} – C_{44}$) for homogenized NbTaTiV alloy at RT, 700 °C, and 900 °C.

Parameters / Conditions	A_Z	A_{VR}	K/G	Cauchy Pressure	VEC
RT	1.2405	0.00557	3.4172	74.70	4.68
700 °C	1.4860	0.01872	3.6412	76.59	-
900 °C	1.6062	0.02672	2.4832	30.13	-

4.4.2 Mechanical Stability and Ductility of the NbTaTiV Refractory HEA

The mechanical stability of the NbTaTiV refractory HEA can be evaluated, considering the values of single-crystal elastic constants. Born and Huang suggested the evaluation criteria of the elastic stability through the dynamical stability conditions, $C_{11} > |C_{12}|, C_{11} + 2C_{12} > 0, \text{and } C_{44} > 0$ [129, 130]. According to elastic constants in Table 4.2, the present alloy shows good mechanical stability in all ranges of temperatures.

The intrinsic brittle/ductile deformation behaviors of HEAs, which dominantly consist of solid solution phases, can be predicted by the interrelation of polycrystalline elastic moduli, such as the Cauchy pressure ($C_{12} - C_{44}$) [89], Pugh ratio [bulk modulus (K) / shear modulus (G)] [88, 91], and Poisson' ratio (v) [90]. The Cauchy pressure (CP) often used to categorize the type of atomic bonding. The large and positive CP represents the increased degree of the metallic-bonding character with the ductile-deformation behavior, while the negative CP stands for covalent bonding with brittle behavior [89]. Moreover, Pugh suggested that the B/G ratio can be applied to predict the ductility and brittleness of materials [88]. The brittle-to-ductile transition point $(K/G)_0$ is 1.75, which is established by experimental results of large amounts of materials. Higher values of Pugh ratios (> 1.75) represent that the materials are ductile, whereas lower values are related to the brittle property [131]. Based on the empirical criteria of the Pugh ratio above, the ductile/brittle limit may also be assessed by the Poisson' ratio, considering the correlation between v and $(K/G)_0$, as v = (3K - 2G) / [2(3K + G)], in case of isotropic

polycrystalline materials. Therefore, the brittle-to-ductile transition limit $(K/G)_0$ > 1.75 corresponds to v > 0.26. Note that the brittle-ductile criterion for bulk metallic glasses is v > 0.31 [90, 132]. According to the values for the Cauchy pressure, Pugh ratio, and Poisson' ratio in Table 4.2 and Table 4.3, which are obtained from in-situ neutron experiments, it is found that these predicted standards of ductility manner are in good agreement with the experiment data, showing the excellent ductility of the NbTaTiV refractory HEA.

4.4.3 Line-profile Modeling

In order to further investigate the deformation behaviors of NbTaTiV alloy, during plastic deformation, the line-profile modeling and analyses, considering the evolutions of neutron diffraction peak width, are carefully conducted as a function of macrostrains at elevated temperatures. In general, plastic deformation often leads to significant broadening of diffraction peaks, which is dominantly contributed by the formation of inhomogeneous strain fields [62, 63, 133]. It is well known that the inhomogeneity of the sub-grain structure is usually more related to the accumulation of dislocations than variations of intergranular strains. Thus, it gives rise to strain fluctuations with the strain field around dislocations responsible for diffraction peak broadening [134]. With the above fundamental understanding of the plastic-deformation behavior in metal materials, evolutions of diffraction peak widths at different strain levels for the NbTaTiV refractory HEA are further discussed by the Williamson-Hall peak broadening analysis approach [95]. The Williamson-Hall plot efficiently provides the qualitative behaviors of the diffraction-

peak-broadening profile (ΔK), considering the grain size and strain effects, as shown in following modified Williamson-Hall plot equation [93, 135, 136]:

$$(\Delta K)^2 = (0.9/D)^2 + (\pi A^2 b^2/2)\rho(K^2C) + O(K^2C)^2 \quad (4.14)$$

where *D* is the average sub-grain size, A is a constant relying on the effective outer cutoff radius of dislocations, *b* is the magnitude of the Burgers vector, *ρ* is a dislocation density, O is the noninterpreted higher-order terms, and *C* is the dislocation-contrast factor. The ΔK equals -K Δd/d, where $K = \frac{1}{d}$, d (nm) is the d-spacing, and Δd (nm) is the FWHM, which is obtained from neutron diffraction with single-peak fitting.

The dislocation contrast factor, C_{hkl}, is obtained using the ANIZC software [137], considering averaged possible slip systems, elastic anisotropy factor, single-crystal elastic constants (obtained from Section 3.3) and type of mobile dislocations as given by

$$C_{hkl} = C_{h00}\left[1 - q\left(\frac{h^2k^2+k^2l^2+h^2l^2}{(h^2+k^2+l^2)^2}\right)\right] \quad (4.15)$$

It is found that the values of *q* and C_{h00} to be 2.2244 and 0.2415 for screw dislocation, and 0.0673 and 0.1937 for edge dislocation, at RT. The obtained values of *q* and C_{h00} at various temperatures are listed in Table 4.4, considering the single-crystal elastic constant. With substituting the values of C_{hkl} and ΔK into Eq. (4.14), the modified Williamson-Hall plots for the NbTaTiV alloy corresponding to the macrostrain range from 0 to 15 %, is shown in Figure 4.6. These plots could

provide significant features of deformation behaviors. The response of linear fitting of the plot, considering specific types of dislocations, refers to the dominant mobile dislocation character during plastic deformation [93, 136]. Hence, when the plot applied q and C_{h00} values as pure screw dislocations (q = 2.2244 and C_{h00} = 0.2415), the non-monotonous deviation of ΔK as a function of K^2C gradually increased with increasing the macrostrain except the initial status (0 % strain) as shown in Figure 4.6(a). However, the datum points follow a linear fitting at all strain levels, when the values of ΔK and K^2C obtained with the pure edge-dislocation consideration (q = 0.0673 and C_{h00} = 0.1937), as shown in Figure 4.6(b). The deviations between experimental data point and linear fitted line, considering the edge or screw dislocation as a dominant type of mobile dislocation at elevated temperatures, are quantitatively described by R-squared coefficients in Table 4.5. These results infer that the type of mobile dislocations of the NbTaTiV refractory HEA is edge dislocations in initial condition (non-deformed) at elevated temperatures. Moreover, with increasing macrostrains (up to 15 % deformed), the <111> {110} edge dislocation is sustained as a dominant mobile dislocation character.

The BCC metallic materials, typically, show that the mobility of edge dislocations is faster than screw dislocations due to their core properties of dislocations during plastic deformation [138-140]. The critical stress, which forces to move the edge dislocation, is quite small (< 10 MPa for the pure BCC Fe), leading to the fact that edge dislocations can be easily annihilated, which results in the screw/edge

anisotropy in the apparent mobility deviation [140]. As a consequence, the remained dislocations tend to be more of a screw character in BCC metals. Recently, however, Rao *et al*. [141] have reported atomistic simulations of plastic-deformation behaviors for the BCC HEA in terms of dislocation motions. This in-depth investigation suggests that the prediction of the tendency of dislocation motions in the BCC solid-solution HEA, which show the random elemental distribution, is considerably different with conventional BCC metals. During the plastic deformation, the edge dislocation core can be deviated from their neutral dislocation planes, producing the wavy dislocation lines due to the severe lattice distortion, which is induced by compositional fluctuations and thus lead to not only strengthening but also huge difficulty of the movement of edge dislocations. With these predictions of plastic-deformation behaviors for the BCC HEA, it is worth to noting that the amount of edge dislocations is comparable to that for the screw dislocations, which is significantly anomalous, as compared to the normal BCC metals. As similar to the above reported prediction, the dominant mobile dislocations of the present NbTaTiV BCC refractory HEA, which has severe distorted lattices, are close to <111> {110} edge dislocations with increasing the macrostrain, as presented in Figure 4.6(b).

Furthermore, the slope of the modified William-hall plot can provide the evolution of dislocation densities as a function of macrostrains at elevated temperatures according to Eq. (4.13). The second coefficient $(\pi A^2 b^2/2)\rho$ in Eq. (4.14) represents the slope of plots as shown in Figure 4.6(b-d), and it is majorly

determined by the dislocation density (ρ) [142]. The detailed values of the slopes $(\pi A^2 b^2/2)\rho$ with different macrostrains at elevated temperature are listed in Table 4.6. The slope of the modified William-hall plot is gradually increased during plastic deformation from 0 to the 15 % macrostrain at RT, manifesting the development of dislocation substructures with the increase of dislocation densities. On the other hand, there is no considerable change of slopes when the sample deformed from 5 % to 15 % at 700 °C, as shown in Figure 4.6(c), then eventually the slopes at all ranges of macrostrain become close to the initial state (0 %) at 900 °C, showing the efficient structural relaxation.

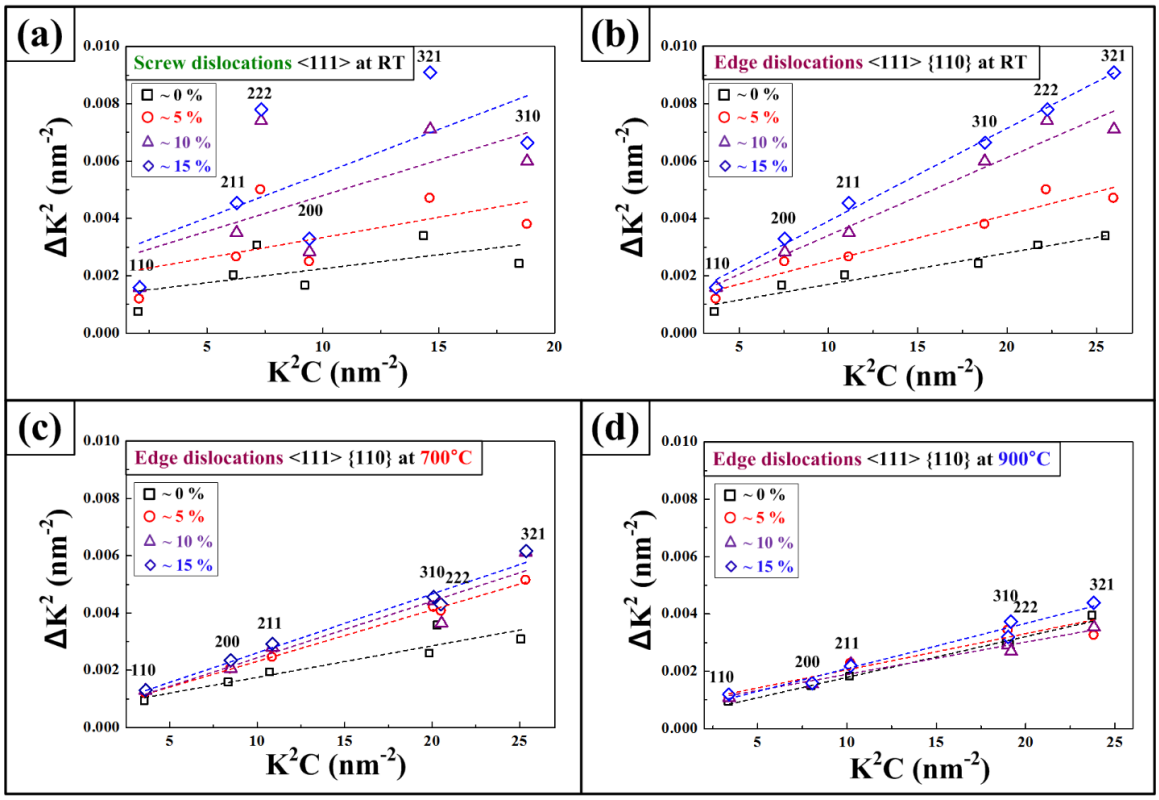

Figure 4.6 Neutron diffraction pattern line-profile modeling for the homogenized NbTaTiV alloy during plastic deformation, using the modified Williamson-Hall plot at elevated temperatures. The peak broadening analysis, ΔK^2 as a function of K^2C, for the sample compressed from 0 % to 15 %, considering the dominant type of dislocation as a pure (a) <111> screw dislocation at RT, (b) <111> {110} edge dislocation at RT, (c) <111> {110} edge dislocation at 700 °C, and (d) <111> {110} edge dislocation at 900 °C, respectively.

Table 4.4 Substituting values (C_{h00} and q) for the dislocation contrast factor (C_{hkl}) to perform the modified Williamson-Hall plots at RT, 700 °C, and 900 °C. The C_{h00} is obtained, using the ANIZC software, considering the single crystal elastic moduli (C_{11}, C_{12}, and C_{44}) at various temperatures, then q is mathematically calculated according to Eq. (4.15).

Conditions / Dislocation type	RT		700 °C		900 °C	
	C_{h00}	q	C_{h00}	q	C_{h00}	q
<111> {110} Edge dislocation	0.19366	0.06728	0.22153	0.57851	0.21296	0.61448
<111> Screw dislocation	0.24149	2.22441	0.25721	2.36367	0.26606	2.43006

Table 4.5 R-squared coefficients, which is statistically obtained from the fitting of modified Williamson-Hall plots for the homogenized NbTaTiV alloy at various temperatures and macrostrains. The goodness of fitting of a modified Williamson-Hall plots with ≈ 0 %, 5 %, 10 % and 15 % macrostrain at RT, 700 °C, and 900 °C is quantitatively described by R-squared coefficients. The 100 % value of R-squared indicates a perfect fitting.

Parameters / Conditions		R^2(%)			
		~ 0 %	~ 5 %	~ 10 %	~ 15 %
Edge dislocation	RT	93.94	92.14	95.86	99.41
	700 °C	82.91	99.68	89.70	96.71
	900 °C	98.56	85.04	94.17	96.63
Screw dislocation	RT	20.39	18.06	23.30	28.43
	700 °C	19.59	35.96	39.29	35.17
	900 °C	28.22	13.96	28.80	8.66

Table 4.6 The coefficient of the linear fitting in the modified Williamson-Hall plot for homogenized NbTaTiV alloy at elevated temperatures as a function of macrostrain. The second coefficient $(\pi A^2 b^2/2)\rho$ of Modified Williamson-Hall plot with ≈ 0 %, 5 %, 10 % and 15 % macrostrain at RT, 700 °C, and 900 °C.

Conditions / Compressed %	Slope $\left(\pi A^2 b^2/2\right)\rho$ (× 10^{-4})		
	RT	700 °C	900 °C
≈ 0 %	1.319	1.165	1.607
≈ 5 %	1.934	2.137	1.379
≈ 10 %	3.303	2.411	1.279
≈ 15 %	3.979	2.449	1.661

4.5 Conclusion

Overall, this comprehensive study provides the unique elastic and plastic deformation behavior of the single BCC solid-solution phase refractory HEA at elevated temperatures, using in-situ neutron experiments coupled with theoretical calculations. The results of the microstructure and the neutron-diffraction patterns exhibit the excellent BCC single-phase stability up to 900 °C. Furthermore, the present alloy possesses the high yield strength and excellent ductility at RT as well as softening resistance at elevated temperatures. The lattice-strain-evolution results show the distinctive elastic-deformation behavior as an elastic isotropy at RT, and the elastic isotropic-anisotropic transition appeared at about 700 °C.

The single-crystal elastic moduli are obtained from the in-situ neutron-diffraction data coupled with the Kroner model approach, showing the great agreement with first-principles calculations. Moreover, this alloy followed the criteria for the prediction of the ductility, such as the Cauchy pressure, Pugh ratio, and Poisson's ratio. The evolution of the dislocation density and verification of mobile dislocation type was quantitatively investigated by the Williamson-hall plot profile. The dislocation density during the 15 % plastic deformation is significantly decreased at high temperatures due to the strong structural-relaxation effects, and the dominant mobile dislocation can be edge dislocations. It is though that the severely-distorted lattice induces the deviation of the formation of dislocations from their neutral dislocation planes, which, consequently, leads to the significant difficulty of the movement of edge dislocations during plastic deformation. Thus,

the edge dislocations can be the dominant dislocation type for the BCC refractory HEA, which is atypical, as compared to the conventional BCC metals and alloys. These new discoveries of the unique elastic and plastic deformation behaviors of the NbTaTiV refractory HEA may lead to the overall excellent mechanical performance and provide a road map to produce newly-designed polycrystalline materials for high-temperature applications.

CHAPTER FIVE

IMPROVEMENT OF LATTICE DISTORTION BY ADDITION OF ZR ELEMENT IN NBTATIV REFRACTORY HIGH-ENTROPY ALLOY

5.1 Introduction

The maximization of mixing entropy with optimal range of enthalpy in high-entropy alloys (HEAs) can promote the formation of stable single solid-solution phase with the absence of competing intermetallic compounds. The resultant effects, such as lattice distortion, can contribute to excellent mechanical properties, which has motivated numerous efforts to develop and design single-phase HEAs. However, challenges still remain, particularly on quantifying lattice distortion and relating it to materials properties. In this study, we have developed a NbTaTiV refractory HEA with a single body-centered-cubic (BCC) structure using integrated experimental and theoretical thermodynamic calculations (CALPHAD) approach. The microstructural evolutions have been investigated by systematic heat-treatment processes. The typical dendrite microstructure was observed, which is caused by elemental segregation during the solidification in the as-cast condition, and structural inhomogeneity and chemical segregation were completely eliminated by the proper homogenization treatment for 1,200 ºC for 3 days. The homogeneous elemental distribution was quantitatively verified by the Atom Probe Tomography (APT) technique. Importantly, results indicate that this HEA exhibits high yield strength and ductility at both room and high temperatures (under 900 °C). Furthermore, the effects of the high mixing entropy on the mechanical properties

are further discussed and quantified in terms of lattice distortions and interatomic interactions of the NbTaTiV HEA via first-principles calculations. It is found that the local severe lattice distortions are induced, due to the local atomic interactions and atomic-size mismatch in the homogenization-treated NbTaTiV refractory HEA.

5.2 Experimental Methods

5.2.1 Materials Preparations

The nominal chemical compositions of the present HEA is Nb20Ta20Ti20V20 in atomic percentage (at. %). An ingot of alloy was fabricated from Nb, Ta, Ti, V and Zr pure elements (99.99 weight percentage elemental purity), using the vacuum-arc-melting facility. The melting chamber was evacuated to 10-5 torr pressure then the high-purity argon gas injected to generate a stable arc beam. To perform a uniform elemental distribution, the ingot has gone through 10 times melting and solidification processes. From the prepared ingot alloy, the cylindrical rod with 4-mm diameter and 50-mm length samples were fabricated using drop casting to conduct microstructure investigation and compressive mechanical test. The systematic heat-treatments were applied to the rod-sample at 1,000 °C for 1day and 1,200 °C for 12 hours after sealing the samples in the vacuumed (10-2 torr) quartz tube to avoid oxidation contamination.

5.2.2 CALPHAD Modeling

The phase stability of NbTaTiVZr was studied using the CALPHAD (acronym of Calculation of Phase Diagrams) method. The goal of the modeling was to help

interpret experimental results. The TCNI8 thermodynamic database supplied by ThermoCalc^{TM} was used, which covers the entire composition ranges of all ten constituent binaries of the Nb-Ta-Ti-V-Zr system. To enhance the reliability of the database especially for applications for HEAs, the inclusion of thermodynamic descriptions for all ten constituent ternaries is required in future work.

5.2.3 Synchrotron X-ray Diffractions

The synchrotron X-ray diffraction (XRD) experiments for as-cast and heat-treated NbTaTiVZr samples (at 1,000 °C for 1day and 1,200 °C for 12 hours) were conducted using high energy synchrotron XRD at the beamline 11 ID-C, Advanced Photon Source (APS), Argonne National Laboratory. The wavelength employed was 0.1173 Å with a sample to detector distance of 1800 mm, which covered 7 reflections for the BCC (110) to (321) oriented grains. The beam size was 600 × 600 μm, which is the largest beam size to to illuminate enough amounts of grains, and a PerkinElmer area detector was used to obtain the Debye–Scherrer rings using the transmission geometry. To evaluate the phase evolution the Debye–Scherrer rings obtained from the synchrotron XRD were converted into diffraction patterns using the Fit2D software. The diffraction data were then analyzed by performing Rietveld refinement using the General structure analysis system (GSAS II) software to identify the phase formations and lattice parameters.

5.2.4 Scanning-electron Microscopy and Electron-backscatter Diffraction

Scanning-electron microscopy (SEM) was conducted, using a Zeiss Auriga 40 equipped with an Everhart-Thornley secondary-electron, back-scattered-electrons

(BSE), and energy-dispersive X-ray spectroscopy (EDS) detectors. The micro-scale chemical compositions of present alloys were performed by mapping and point EDS analyses. The volume fractions of dendrites and interdendrites in SEM-BSE images were measured, using Image J software. The micro-scales phase distribution for as-cast and homogenized samples was investigated by electron-backscatter diffraction (EBSD) to confirm the presence of single BCC solid-solution phase after homogenization treatment.

5.2.5 Atom-Probe Tomography

To observe atomic-scale elemental distribution, using atom-probe tomography (APT), the sharp-tip specimens were prepared, using standard lift-out methods with a FEI Nova focused ion beam (FIB). The APT runs were performed in a laser-mode to capture large regions of interest. The acquisition conditions were shown as follow: cooling to 30 K, 50 pJ laser energy and 200 kHz pulse repetition rate with a detection rate of 0.0005 ions per pulse. The data collection was performed, using a CAMECA local electrode atom probe (LEAP) 4000XHR equipped with an energy-compensated reflection lens and a 10 pico-second 355nm ultraviolet (UV)-pulsed laser. Then the acquired data were reconstructed and analyzed, using the IVAS 3.6.12 software.

5.2.6 Mechanical Tests

The room temperature mechanical properties of as-cast and homogenization-treated NbTaTiVZr alloys were carried out under uniaxial compression at a strain rate of 10^{-3} S^{-1}, using a computer-controlled Material Test System (MTS) servo-

hydraulic-testing machine. The size of specimens for compression test was 4 mm in diameter and 8 mm in length (aspect ration of 2:1). The compressive mechanical tests were repeated three to five times to ensure the data consistent. The stress-strain curves and values of yield strengths and plastic strains in this paper are selected as the representative data, which exhibits the mean values of yield strengths. The deviation of each set of tests for as-cast and homogenized NbTaTiV alloys were less than 6.5 % and 8 %, respectively, which is mainly originated from small defect of inside of samples, such as voids or pores.

5.2.7 First-principles Calculations

First-principles calculations were performed with the Vienna Ab-initio Simulation Package (VASP), using the projector augmented wave (PAW) method. The exchange-correlation energy was described with the generalized gradient approximation (GGA) in the Perdew-Becke-Ernzehof (PBE) parameterization. A plane-wave cutoff of 400 eV and Monkhorst-Pack k-point grid of 2 × 2 × 2 was used for all calculations. The chemical disorder of the solid solution was modeled using Special Quasirandom Structures (SQS). The SQS was employed, using a method based on a Monte Carlo-simulated annealing loop to enumerate atomic configurations and choosing the configuration for which the calculated correlation functions are a closer match to that of a disordered state. A 64 atom SQS was generated for the NbTaTiV HEA, and a 75 atom SQS was generated for the NbTaTiVZr HEA. The SQS volume and ionic positions were optimized with an energy (EDIFF) convergence criteria of 0.1 meV.

5.2.8 Transmission-electron Microscopy

The thin foils TEM specimens for transmission-electron-microscopy (TEM) and scanning-transmission-electron-microscopy (STEM) observation were prepared by focus ion beam (FIB, TESCAN GAIA3). The rod sample were cut into under 1000 um sheet with diamond saw. The sheet sample were flattened on both sides with sandpaper (600#, 2000#, 2500#, and 4000#), and the top side is polished with diamond lapping film (1 um and 0.1 um) for better adhesion, and slurry (0.05 um and 0.02 um) on polishing cloth. The in-situ transfer technique was adopted to fabricate the samples. It follows the sample thinning process in conventional FIB sample preparation process, but the sample is transferred to TEM grid with nanomanipulator (OXFORD OmniProbe 400) in FIB chamber. With this technique, the drift rate is reduced, sample can be thinner, and the image quality is improved due to the lack of carbon supporting film on copper grid. Transmission electron microscope (TEM, JEOL ARM200F) equipped with High angle annular dark field (HAADF) detector was used to measure the lattice distortion factor. The position of each atomic column on HAADF image was fitted with 2D Gauss fitting. The distance of nearest neighbor atomic column along different crystal plane or direction on HAADF images were collected to calculate the lattice distortion factor.

5.3 Results

5.3.1 Theoretical Prediction of Phase Formation for NbTaTiVZr HEA via CALPHAD Modeling

The prediction of phase evolution in non-equilibrium state as well as equilibrium state, including the possible chemical distribution for NbTaTiVZr alloy were performed by CALPHAD modeling. Figure 5.1(a) shows the non-equilibrium solidification using the Scheil-Gulliver models [143, 144], which presumes equilibrium mixing in the liquid state and no diffusion in the solid state. This modeling predicts the formation of a single BCC solid solution during the entire non-equilibrium solidification. In fact, the real solidification path will be somewhat between equilibrium and Scheil-Gulliver models. The simulation also anticipates the likely segregation in particular associated with Ta and Zr due to constitutional cooling: Ta enrichment in the dendrite arms at earlier stages of solidification, and Zr enrichment in the interdendritic region in later stages. The predicted elemental segregation largely agrees with EDX/APT results in the as-cast state.

The calculated equilibrium phase diagram for NbTaTiVZr is shown in Figure 5.1(b). The database predicts a liquidus (T_{liq}) temperature of 1,949 °C and a solidus (T_{sol}) temperature of 1,581 °C. The primary BCC solid solution phase starts to decompose at 942 °C (T_{dec}) by precipitation of a Zr-Ti-rich BCC phase (the combined contents of Zr and Ti exceeding 80 atomic percentage). The ratio of the temperature range where the BCC solid solution is stable over the solidus temperature [i.e.,($(T_{sol} - T_{dec})/T_{sol}$] is determined to be 0.40 for NbTaTiVZr,

agreeing with the argument made by Gao [57], who proposed that a ratio greater than 0.30 typically favors a single-phase solid solution in the as-cast state.

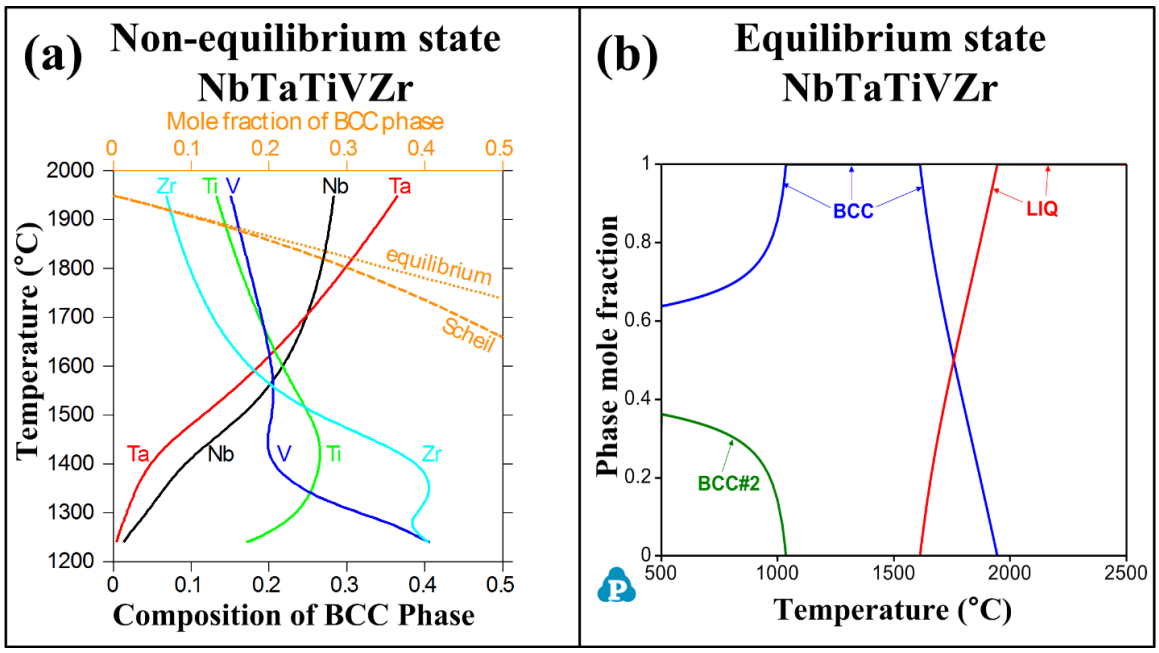

Figure 5.1 CALPHAD-calculation data for NbTaTiVZr. Calculated equilibrium phase mole fractions during solidification for $Nb_{19.8}Ta_{18.3}Ti_{20.8}V_{19.8}Zr_{20.7}$. The inset shows the composition evolution of the BCC solid-solution phase during non-equilibrium solidification using the Scheil–Gulliver models.

5.3.2 Phase and Microstructural Evolutions for NbTaTiVZr HEA via Systematic Thermal Treatment

The scanning-electron microscopy (SEM) back-scattered electron (BSE) image of the as-cast NbTaTiVZr HEA is illustrated in Figure 5.2(a). The simple dendritic microstructure is observed in this condition, which is the typical feature of microstructure in the most of as-cast HEAs [9, 57, 64, 145-149]. The presence of different contrast between dendrites and interdendrites is mainly contributed by different principle elements concentration during the solidification process as predicted by CALPHAD simulation. In order to verify the specific chemical compositions and elemental distributions of dendrite and interdendrite regions in as-cast alloy, the point energy-dispersive-spectroscopy (EDS) analysis and EDS mapping were conducted (not shown). The Ta and Nb, which exhibit relatively high melting temperature, is the dominantly distributed in dendrite regions, whereas the interdendrite is enriched in Zr element. The detailed averages of atomic fraction are given in Table 5.1. These results of elemental distribution are consistent with the CALPHAD modeling in Figure 5.1. Figure 5.2(b) shows the synchrotron XRD pattern of the as-cast NbTaTiV alloy, which is refined by Rietveld full pattern refinements [150]. The sharp diffraction peaks are basically indexed as BCC phase with a lattice parameter of 3.29568 ± 0.000160 Å. However, diffuse scattering is significantly observed in all diffraction peaks, indicating the asymmetric peaks toward the origin. This gentle slope in left side of peaks imply the overlapping of two peaks, which is diffracted from both dendrites and interdendrites regions with

close lattice parameters. The distinct microstructural variation is obtained from the heat-treated sample at 1,000 °C for 1 day, as shown in SEM-BSE image [Fig. 2(c)]. The interfaces between dendrites and interdendrites become clearer than as-cast condition, which may arise from the significant spinodal decomposition, as shown inset high magnitude SEM image in Figure 5.2(c). Moreover, the volume fractions of interdendrite regions are significantly increased from 8.8 % to 18.1 % after heat treatment at 1,000 °C for 1 day. The quantitatively measured dendrite arm spacing and volume fractions are inserted in each figure. The preferentially distribution of particular element in dendrite and interdendrite is clearly reflected in the synchrotron XRD pattern, as shown in Figure 5.2(d). The diffraction peaks are identified as a two BCC phases, which manifest the significantly different lattice parameters between dendrite and interdendrite. The lattice parameters were estimated to be 3.28499 ± 0.000060 Å (BCC 1) and 3.42753 ± 0.000030 Å (BCC 2), respectively. These observations imply that the distribution of different principal atom, which possess the largest distinction of lattice parameter in dendrite (Ta) and interdendrite (Zr), could induce the significant variation of lattice parameters, thus it results in the formation of two BCC phase after premature homogenization-treatment at 1,000 °C for 1 day. In order to fulfill a single phase with homogeneous elemental distribution, the NbTaTiV alloy was subjected to a further heat treatment at higher temperature. The simple microstructure with complete elimination of elemental segregation was successfully achieved after heat-treatment at 1,200 °C for 12 hours, as shown in Figure 5.2(e). The analysis of homogeneous elemental distribution was further verified by EDS measurements, showing chemical

composition of nearly-equi-atomic percentage (Table 5.1). With these trends of microstructural and compositional characterization of homogenized NbTaTiVZr alloy, the synchrotron XRD pattern confirm the formation of only single BCC phase with the lattice parameter of 3.30919 ± 0.000149 Å. Importantly, the feature of main BCC diffraction peaks eventually become close to symmetrical feature [Figure 5.2(f)]. Similarly, the further crystallographic-based microstructural verification of the formation of single BCC solid-solution phase for as-cast and homogenized NbTaTiVZr alloys was examined by the EBSD-phase maps, as shown in Figure 5.2(g) and (h). However, the synchrotron XRD, SEM, EDX and EBSD techniques cannot afford to provide the in-depth information of elemental distribution, such as randomness of atomic arrangement with quantitatively measured nano-scale chemical compositions. Note that the precise chemical composition of homogenized NbTaTiV will be used as an important substituting value to calculate lattice distortion in discussion section.

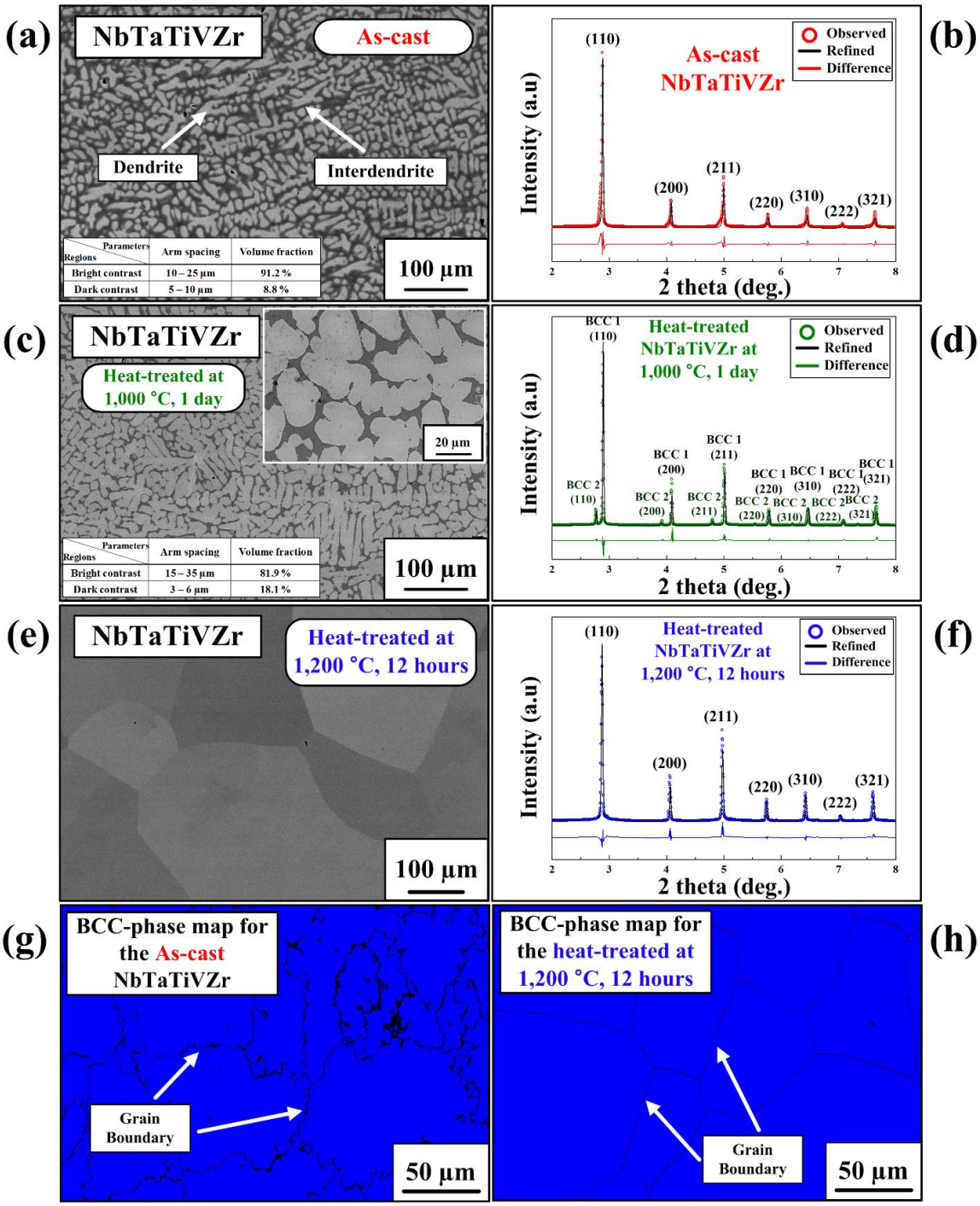

Figure 5.2 Phase and microstructural characteristics of as-cast and heat-treated NbTaTiVZr, studied by SEM, synchrotron XRD, and EBSD. The SEM-BSE images and synchrotron XRD patterns for as-cast and after-annealed samples at different temperatures and time periods: (a) (b) as-cast, (c) (d) 1,000 °C for 1 day, and (e) (f) 1,200 °C for 12 hours, EBSD-phase map of the (g) as-cast and (h) homogenization-treated NbTaTiVZr alloy.

Table 5.1 SEM-EDS and APT compositions, and elemental distribution analyses of as-cast and homogenization-treated refractory NbTaTiVZr HEAs. Chemical composition (in atomic percent, at. %) of constitutive regions in as-cast and homogenized alloys, determined using the energy-dispersive spectroscopy (EDS) and atom-probe tomography (APT), respectively. The binomial distribution of the analyzed data in comparison to the binomial distribution of the theoretical data is provided by the parameters of χ^2 and μ for each element.

Parameters / Materials	-	EDS results	APT results	
Alloys	**Elements**	**Average of atom fraction (%)**	**Average of atom fraction (%)**	**μ**
Dendrite region in As-cast NbTaTiVZr (Bright contrast region)	**Nb**	**25.4**	**22.962**	**0.0633**
	Ta	**30.7**	**27.275**	**0.1472**
	Ti	**16.7**	**18.358**	**0.0726**
	V	**15.5**	**17.122**	**0.0587**
	Zr	**11.7**	**13.672**	**0.0771**
Interdendrite region in As-cast NbTaTiVZr (Dark contrast region)	**Nb**	**12.9**	**15.282**	**0.0484**
	Ta	**7.4**	**11.764**	**0.0955**
	Ti	**20.2**	**21.419**	**0.0361**
	V	**22.9**	**20.129**	**0.0270**
	Zr	**36.5**	**30.437**	**0.0555**
Homogenized NbTaTiVZr	**Nb**	**18.8**	**19.786**	**0.0808**
	Ta	**20.1**	**18.327**	**0.1626**
	Ti	**20.1**	**20.267**	**0.0710**
	V	**20.2**	**19.809**	**0.0401**
	Zr	**20.8**	**20.670**	**0.0905**

5.3.3 Verification of Chemical Homogeneity for Homogenized NbTaTiVZr HEA

In order to complement the limitation of experimental investigations above, the atom probe tomography (APT) studies for as-cast and homogenized NbTaTiVZr samples were employed, as shown in Figure 5.3. The analyzed volumes of APT experiments for as-cast and homogenized samples are 58 × 57 × 102 nm^3 (dendrite region in as-cast), 66 × 67 × 236 nm^3 (interdendrite region in as-cast), and 71 × 70 × 99 nm^3 (homogenized), respectively. The results of one-dimensional concentration-depth data (sample distance versus concentration) and atom maps for as-cast sample [Figure 5.3(a)] indicate a uniform distribution of all alloying components without statistical-considerable fluctuations of atom concentration in the dendrite and interdendrite regions. On the other hands, the clear differences of principal element concentration between two regions are observed, showing the enrichment of Nb and Ta elements in dendrite regions and Zr in interdendrite regions, respectively. The quantitatively measured atomic-scare chemical compositions of as-cast NbTaTiVZr alloy are listed in Table 5.1. After the homogenization treatment at 1,200 °C for 12 hours, not only the homogeneous distribution of constituent elements but also elemental distribution as a nearly-equi-atomic percentage along a 67-nm cylindrical region are achieved as shown in Figure 5.3(b). The chemical composition was found to be 19.786 at. % for Nb, 18.327 at. % for Ta, 20.267 at. % for Ti, 19.809 at. % for V and 20.670 at. % for Zr, respectively. With these results of nano-scale atomic distributions, the further quantitative measurement of randomness of atoms arrangement was evaluated by

the chi-squared statistics with a frequency distribution analysis (FDA), as shown in right-hand side of Figure 5.3(b). The FDA were obtained from comparison between measured data and binomial distribution, which represents a random elemental distribution [28, 59, 151]. The results of FDA analysis reveal that the experimentally observed data (dots) significantly overlapped with theoretical binomial distribution (solid line), implying the excellent homogeneity of elemental distribution. Furthermore, the randomness of atoms arrangement can also be quantitatively evaluated by the values of μ or χ^2, as described below.

The theoretical distribution function, $f(n)$, describes the distribution of elements, which assumed that A atoms are randomly distributed throughout the dataset, as expressed below:

$$f(n) = Np_{\mathrm{B}}(n) = N\frac{n_{\mathrm{b}}!}{n!(n_{\mathrm{b}}-n)!}c_{\mathrm{A}}^{n}(1-c_{\mathrm{A}})^{(n_b-n)} \tag{5.1}$$

where n is the number of solute atoms, N is the total number of fixed size blocks, n_{b} is an equal number of atoms, and c_{A} is the bulk concentration. The deviation of an observed experimental data with theoretical binomial distribution data can be quantified by means of χ^2 statistics,

$$\chi^2 = \sum_{n=0}^{N}\frac{\left(e(n)-f(n)\right)^2}{f(n)} \tag{5.2}$$

where, e(n) is the experimentally measured number of blocks containing n solute atoms, N is a number of discrete rectangular blocks. In order to evade the dependence of sample size and volume for all the data sets, the normalization of χ^2 is necessary to gain the comparable values. The normalized χ^2 returns a value of μ, independent of the sample size, and it can be expressed as follows:

$$\mu = \sqrt{\frac{\chi^2}{N+\chi^2}} \tag{5.3}$$

The μ value, as a normalized auto-correlation parameter of χ^2, ranges between 0 and 1, where 0 indicates the solid solution with perfect random elemental distribution, whereas 1 represents a complete association of the elements, such as intermetallic compounds. Based on these fundamental understanding of analysis, the μ values of homogenized NbTaTiVZr sample are close to value of 0 for all constituent elements, as listed in Table 5.1, indicating a significant random elemental distribution in single BCC solid-solution phase.

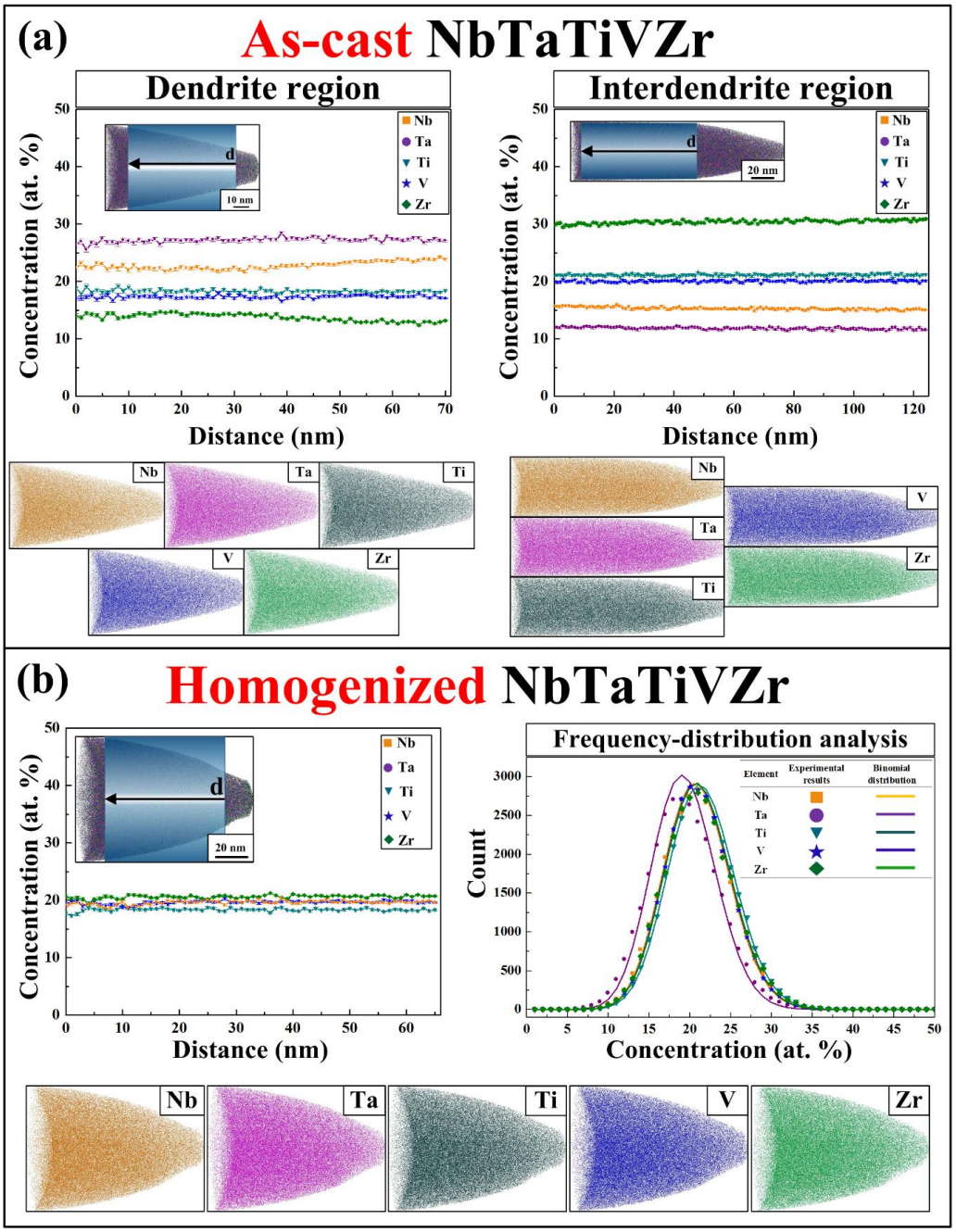

Figure 5.3 Atomic-scale elemental distribution of as-cast and homogenized NbTaTiVZr alloys alloy (a) Concentration-depth profile of all alloying elements taken along the black arrow (top), three-dimensional atom maps of individual elements (middle) and frequent-distribution histograms (bottom), for the dendritic region, Interdendritic region in the as-cast and (b) homogenized NbTaTiVZr alloy. The frequency-distribution histograms of constituent elements were calculated with a block size of 100 atoms with the solid lines showing the binomial-distribution curves, and the dots are the observed experimental results.

5.3.4 Comparison of the Mechanical Properties and Strengthening Mechanism between NbTaTiV and NbTaTiVZr HEAs

The compressive engineering stress-strain curves for as-cast and homogenization-treated NbTaTiVZr HEAs at RT with a strain rate of $1 \times 10^{-3} s^{-1}$ are shown in Figure 5.4. The as-cast alloy reveals high yield strength (σ_y) of 1,352 MPa with comparable compressive plastic strain (ε_p) of 19.8 %. Similar with the mechanical properties of NbTaTiV refractory alloy (the inset in Figure 5.4), there is no significant change of yield strength and ductility between as-cast and homogenization treated NbTaTiVZr samples. These results of mechanical tests imply that the chemical homogeneity does not strongly effect on mechanical properties. The detail values of mechanical properties are summarized in Figure 5.4. With addition of Zr element in the NbTaTiV alloy, however, there is pronounced enhancement of yield strength from 1,239 MPa to 1,518 MPa. In fact, both alloy systems show the single solid-solution phase formation, simple feature of microstructure, and random atomic distribution, hence, the solid-solution strengthening can be the considerable strengthening mechanism. Thus, it is clearly concluded that the addition of equi-atomic percentage of Zr element remarkably extends the solid-solution strengthening, compared to NbTaTiV alloy.

Typically, the metallic solid-solutions are strengthened by the elastic interactions between local stress field, which is induced by solute atoms, and dislocations [70]. However, all constituent atoms in HEAs, which are consisted of equi-atomic percentage of multi principal elements with homogeneous elemental distribution,

can be regarded as the solute atoms of solvent atoms. This feature of atomic distribution efferently improves the degree of strengthening.

With the fundamental understanding of solid-solution strengthening mechanism, the strengthening theories have developed by Toda-caraballo et al. to quantitatively assess the solid-solution strengthening for compositional complex alloys, such as HEAs, considering two major strengthening components, such as elastic-modulus and atomic-size mismatches, as expressed by the following equation:

$$\Delta\sigma_s = \Delta\sigma_G\ (elastic\ modulus\ mismatch) + \Delta\sigma_a\ (atomic\ size\ mismatch) =$$

$$AG\left(\frac{9}{8}\sum c_j\delta_{Gij}\right)^{\frac{4}{3}} c_i^{\frac{2}{3}} + AG\beta\left(\frac{9}{8}\sum c_j\delta_{aij}\right)^{\frac{4}{3}} c_i^{\frac{2}{3}} \quad (5.4)$$

where A is a dimensionless material constant (0.04), G is the shear modulus of alloy, which is estimated by rule of mixtures (49.5 GPa for NbTaTiV and 46.2 GPa for NbTaTiVZr), $\boldsymbol{\beta}$ is the dislocation type-dependent constant (9), c_j is the atomic fraction of jth element in the alloy, δ_{aij} and δ_{Gij} are an atomic-size and modulus differences, $\delta_{aij} = 2(r_i - r_j)/(r_i + r_j)$, $\delta_{Gij} = 2(G_i - G_j)/(G_i + G_j)$, and c_i is a solute concentration. The estimated elastic modulus mismatches (modulus distortions) in NbTaTiV and NbTaTiVZr alloys are to be $\Delta\sigma_G$ ≈ 227.0 MPa and 233.6 MPa, respectively, indicating almost same amount of contributions for solid-solution strengthening after addition of Zr element. On the other hands, the value of strengthening by atomic size mismatch (lattice distortions, $\Delta\sigma_a$) is drastically improved from ≈ 431.5 MPa (NbTaTiV) to 906.8 MPa (NbTaTiVZr). These results

of calculations of solid-solution strengthening, considering two different strengthening components suggest that the principal strengthening mechanism for both alloys was determined to be solid-solution hardening, which majorly accounts for lattice distortions rather than modulus distortions. Moreover, the distorted lattice was significantly improved by addition of Zr element, resulting in substantial enhancement of yield strength.

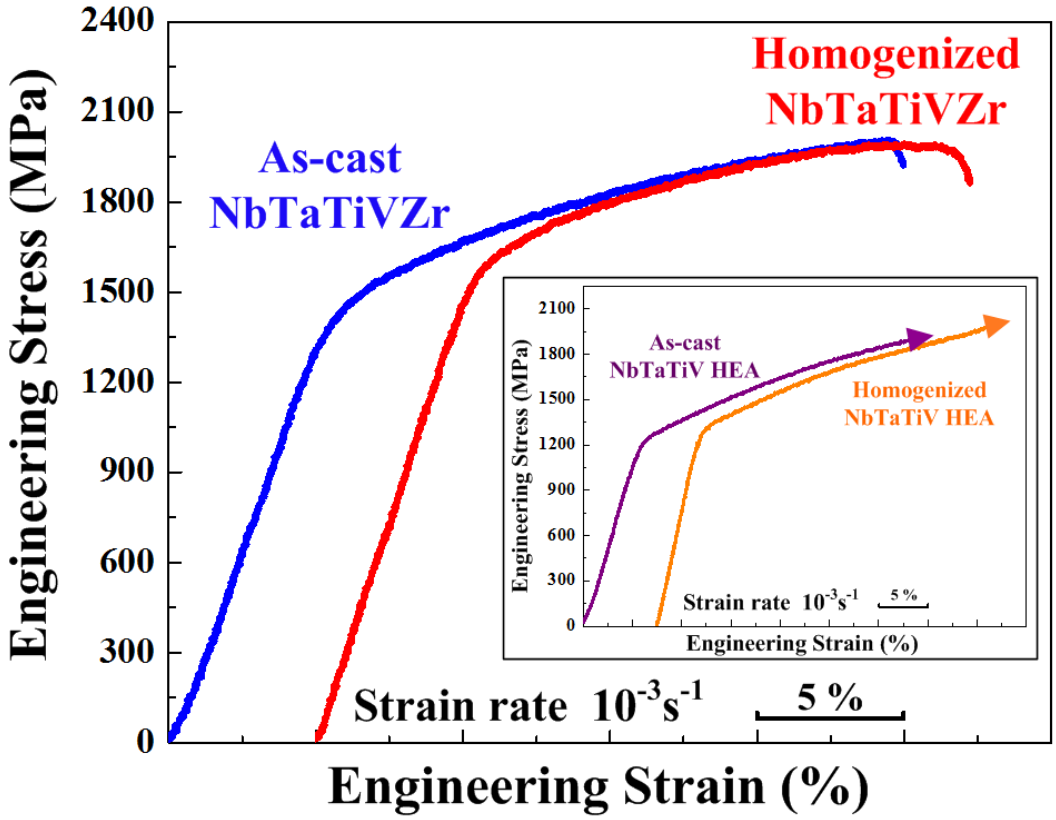

Alloys	Conditions	Yield strength, σ_y (MPa)	Plastic strain, ε_p (%)
NbTaTiVZr	As-cast	1,352	19.8
	Homogenized	1,518	16.7
NbTaTiV	As-cast	1,196	> 30
	Homogenized	1,239	> 30

Figure 5.4 Comparison of mechanical properties of the as-cast and homogenization-treated NbTaTiV and NbTaTiVZr. Engineering compressive stress-strain curves of the as-cast and homogenization-treated NbTaTiV and NbTaTiVZr alloys at room temperature.

5.3.5 Predictions of Interatomic Distances Distribution for NbTaTiV and NbTaTiVZr HEAs via First-principles Calculations

The enhancement of solid-solution strengthening by lattice distortion is significantly associated with variation of atomic sizes as well as bond lengths of the HEA, which stems from the chemical interactions among the composed multi-principal elements. Figure 5.5(a) shows the distribution of first through fifth nearest neighbor atomic distances, which were analyzed by a relaxed 64-atom NbTaTiV and 75-atom NbTaTiVZr HEAs SQS. The blue regions represent the distribution of the quaternary (NbTaTiV) nearest neighbor distances, and the red regions refers to the distribution of the quinary (NbTaTiVZr) nearest neighbor distances. The average first, second, third, fourth, and fifth nearest neighbor distances are to be 2.80, 3.23, 4.74, 5.36 and 5.58 for quaternary system and 2.87, 3.31, 4.68, 5.47, and 5.73 for quinary system, respectively, which are marked by the blue and red dashed lines in Figure 5.5(a). It is worth nothing that an increase in the spread of the distributions is noticeable with the addition of the Zr element to the quaternary system, which indicates an increase in lattice distortion. The atomic specie pairs in Figure 5.5(b) show the distribution of first nearest neighbor (1NN) bond lengths ordered by increasing average atomic radii (except for those involving Zr which are grouped at right side of the figure). The prominent tendencies relating atomic sizes and the range of 1NN bond lengths are clearly found. Regardless of type of atomic pairs (homo/heteroatomic pairs), when the atomic pairs contained smaller atoms such as V-V, Ti-V, Nb-V, and Ta-V exhibit very short minimum 1NN bond lengths.

Moreover, these group of atomic specie pairs also have a very large range of calculated 1NN bond lengths with addition of Zr element in NbTaTiV alloy. An explanation for this is that the smaller atoms can form shorter bonds with each other, but the larger spaces around the lattice points in which they occupy allows for a much larger range of bond lengths depending on the local environment.

The atomic species pairs containing Zr, and Ta-Ta, Nb-Ta which have larger atomic radii show larger average 1NN bond lengths and the smallest range of 1NN bond lengths. The addition of Zr, an element with a larger atomic radius than all the other constituent elements results in an increase of the range of 1NN bond lengths for all the atomic specie pairs in the NbTaTiVZr system, except for Nb-Ta, and Nb-Nb. These results indicate that the addition of Zr increases the lattice distortion which is reflected in the increase of the range of 1NN bond lengths. Furthermore, the atomic pairs involving V are most affected from the Zr addition, in that the minimum bond lengths go down and the range of bond lengths go up.

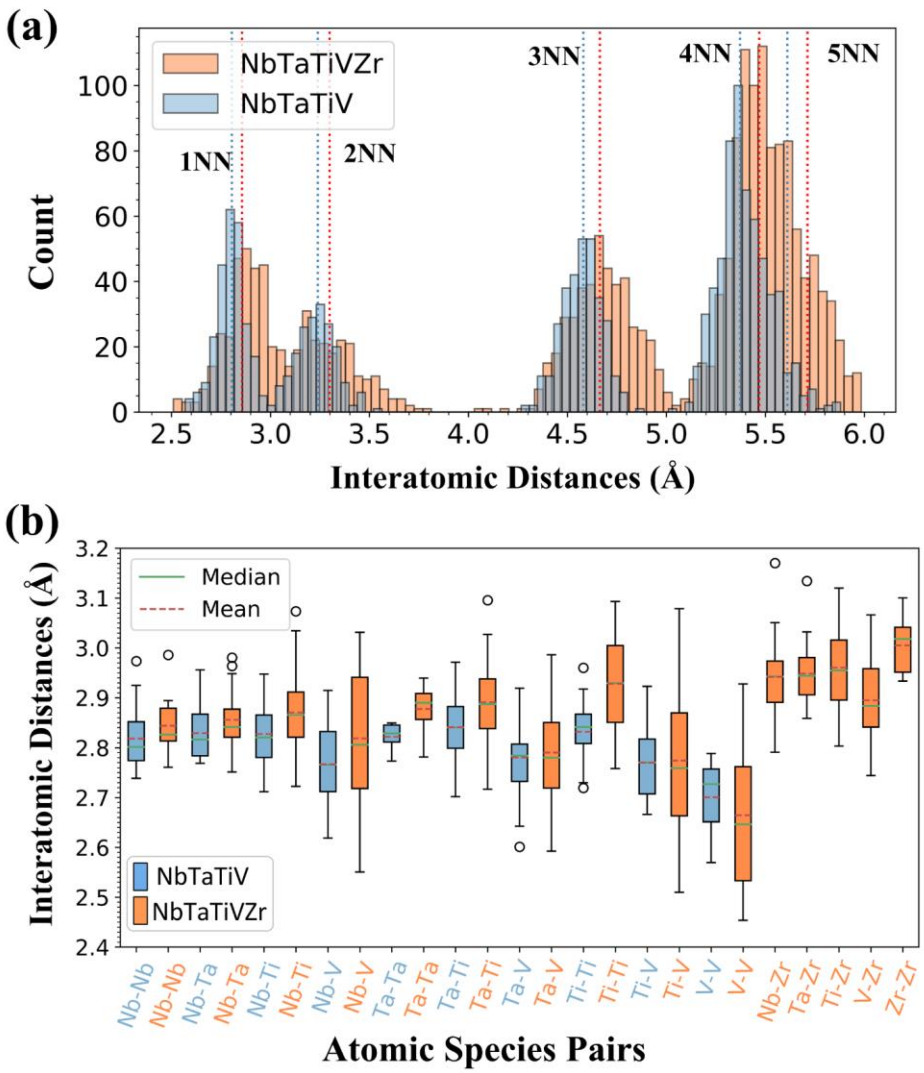

Figure 5.5 First-principles calculation data. (a) Distribution of the interatomic distances for the first to fifth nearest neighbors (NN) of the BCC NbTaTiV and NbTaTiVZr alloys calculated from the optimized SQS. The blue dashed lines show the average interatomic distances for the first to fifth NNs, and (b) Box plot presenting the distribution of interatomic distances of 1NN bonds in the SQS for the BCC NbTaTiV and NbTaTiVZr alloys. The box presents the first and third quartiles of the bond lengths for a type of atomic bonds. The whisker extends to either the 1.5 interquartile ranges or the maximum and minimum values. The median and mean for each type of atomic bonds exhibit as the green solid line and red dashed line, respectively. The reference bond lengths, calculated from comparable BCC structures for the homoatomic pairs and B2 structures for the heteroatomic pairs, are shown in blue squares.

5.4 Discussion

5.4.1 Selection of Additional Element to Induce the Severe Lattice Distortion

Lattice distortion is a one of the core effects in HEAs due to their multi-principal constituent elements with various atomic sizes. The crystal lattice in equiatomic HEAs, which have large deviation of atomic size differences is expected to be more severely distorted than conventional solid-solution strengthened alloys, so that its effect on strength enhancement can be significant. Thus, the numerous efforts have been reported to suggest design strategy of high strength HEAs, considering lattice distortion with atomic radius difference. However, it is still difficult to establish the concrete correlation between lattice distortion and solid-solution strengthening due to the similarity of atomic radius among the transition metal elements. Moreover, when the value of atomic-size difference (δ) exceeds the certain number ($\delta \leq 6.6$ %), the alloy systems tend to form the intermetallics rather than single solid-solution phase, according to empirical rules of HEAs.

Hence, Feng et al. have suggested the new alloy design strategy for BCC refractory HEAs to perform the high strength, which is efficiently promoted by the lattice distortion, considering the structure of constituent elements. Usually, the 9 refractory elements, which are located in columns 2-4 (starting with Ti, V and Cr) of the transition metal in periodic table can be majorly composed in refractory HEAs. These refractory elements can be categorized as two groups, according to their temperature dependent phase stability. The 6 elements (V, Nb, Ta, Cr, Mo, and W) in columns 3 and 4 have a BCC structure at all range of temperatures,

whereas, those in column 2 show martensitic phase transformation from BCC to HCP at low temperature due to Burgers distortion. Although, the refractory HEAs contain HCP structure elements in column 2 (Ti, Zr, and Hf) these alloys still form the single BCC structure instead of HCP structure at various temperatures with inharmonic vibrational entropy. This energetic instability of structure is significantly reduced the shear moduli, causing improved dynamic contributions to severe lattice distortions.

Based on the new alloy design strategy above, the Zr and Hf can be potential candidates as an additional element in NbTaTiV alloy to efficiently induce large amounts of lattice distortions. According to estimate of solid-solution strengthening effects in Eq. (5.4), the quantitatively calculated values of lattice distortions and modulus distortions for NbTaTiVHf alloy are to be $\Delta\sigma_a \approx$ 781.2 MPa and $\Delta\sigma_G \approx$ 385.2 MPa, respectively. These results indicate that the values of improvement of strength by lattice distortion is smaller than Zr element containing and the modulus distortion is also significantly effects on strengthening. Hence, the composition of NbTaTiVZr was chosen in order to ensure the contributions of only lattice distortions to strength enhancement in NbTaTiV alloy.

5.4.2 Comparison of Quantitatively Determined Average Lattice Distortion between NbTaTiV and NbTaTiVZr HEAs via Mathematical Calculation with Synchrotron and Neutron Diffractions

The experimental results of phase and microstructural evolutions (synchrotron diffraction, SEM, EBSD, and APT), mechanical properties and theoretical

calculation of strengthening for NbTaTiV and NbTaTiVZr alloys could concretely characterize not only the single BCC phase formation with homogeneous elemental distribution of both alloys but also the enhancement of yield strength by lattice distortions dominantly after addition of equi-atomic percentage of Zr element. However, it is still necessary to quantitatively and qualitatively estimate the lattice distortions for clear validation of strength enhancement.

Previously, the total lattice distortion for homogenized NbTaTiV alloy was quantitatively determined by mathematical and experimental approaches. The lattice distortion factor $M^D = 8\pi^2(\bar{u}^2)^D\left(\frac{sin\,\theta}{\lambda}\right)^2$ is simply formulated from Debye-Waller temperature factor, $M^T = 8\pi^2(\bar{u}^2)^T\left(\frac{sin\,\theta}{\lambda}\right)^2$, substituting the amplitude of deviation displacement of atoms ($\bar{u}^D$) instead of thermal vibrational amplitude ($\bar{u}^T$). In this case, the $\bar{u}^D$ is a dominant effective term to determine the lattice distortion factor, M^D, which is expressed as

$$\bar{u}^D = \sqrt{\sum_i^n \left(d_i^{eff} - \bar{d}\right)^2 / n} \tag{5.5}$$

where d_i^{eff} is the effective interatomic distance of the *i*th element, and $\bar{d}$ is the average lattice constant of *n* elements, *n* is the number of constituent elements, which are obtained from the lattice constant of the incorporated elements associated to their crystal structure. The detail descriptions of quantitative estimation of lattice distortion, $\bar{u}^D$, are schematically illustrated in Figure 5.6. When the metallic materials are structured by a perfect BCC unit cells, which is made up of the identical interatomic distances around center of atom, the effective

interatomic distance, d_i^{eff}, in each of constituent elements can be same with the average lattice constant, $\bar{d}$, as illustrated in Figure 5.6(a). This consistent elemental arrangement in corresponding unit cells implies the no inherence of distorted lattices, resulting in 0 value of $\bar{u}^D$ according to Eq. (5.5). On the contrary, the BCC HEAs, which are consisted of equi-atomic percentage of multi principal elements with homogeneous elemental distribution, the crystalline lattice in the corresponding BCC unit cells could be severely distorted by various interatomic distances, which is originated from their inter-atomic interaction, as presented in Figure 5.6(b). In this unique case of crystal structures, the deviations between d_i^{eff} and $\bar{d}$ indicate the certain values, which can quantitatively represent of the average lattice distortion in BCC alloy systems.

According to mathematical understanding on determination of lattice distortions above, the d_i^{eff} for NbTaTiV and NbTaTiVZr HEAs were theoretically obtained, considering change of atomic volume of ith element dissolving into the jth element, ΔV_{ij}, by following equation:

$$d_i^{eff} = \sum_j^n f_j \left(1 + \frac{\Delta V_{ij}}{V_i}\right)^{1/3} d_i \quad (5.6)$$

where f_j is the atomic fraction of *j*th element (0.25 and 0.2 for NbTaTiV and NbTaTiVZr), V_i is the atomic volume and d_i is the lattice constant of the ith element. In accordance with the Eq. (5.5), the mathematically calculated values of lattice distortion, $\bar{u}^D$, which were derived from deviation displacements of atoms are to be 0.1186 Å and 0.1832 Å for NbTaTiV and NbTaTiVZr alloys, respectively.

The detailed constituent terms in Eq. (5.5) are summarized in Table 5.2. With this mathematical approach for determination of lattice distortions, the values of $\bar{u}^D$ were experimentally verified from measured chemical compositions and lattice constants, substituting the atomic fractions, which are obtain from APT data and the average lattice constants, which are acquired from synchrotron/neutron-diffractions in f_j and $\bar{d}$ terms, respectively. Note that the lattice constants, measured by synchrotron diffractions, provide locally measured lattice constants (beam size of 600 μm × 600 μm) with high resolution, whereas the neutron diffractions are appropriate method to obtain lattice constants that covers the larger area of sample (beam size of 3.5 mm × 3.5 mm). The experimentally determined values of average lattice distortions, $\bar{u}^D$, for NbTaTiV and NbTaTiVZr HEAs, are in excellent agreement with mathematical calculated parameters as summarized in Table 5.3. These quantitative calculations and measurements of lattice distortions manifest that the addition of Zr elements in NbTaTiV HEA efficiently promotes large variation of interatomic distances, and it results in the significant increase of average distorted lattices about 54 %.

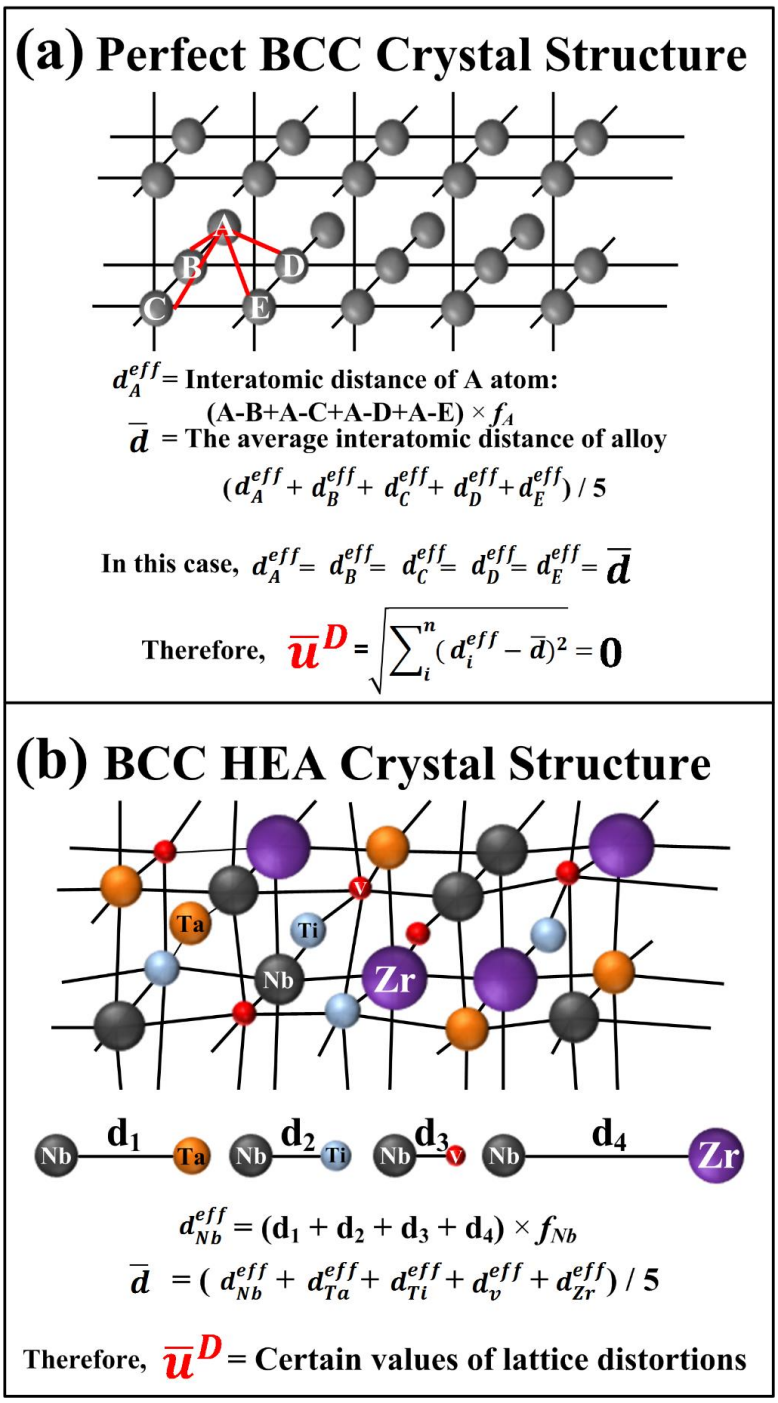

Figure 5.6 Schematic description of (a) perfect BCC crystal structure and (b) HEA crystal structure, showing detailed process of mathematic calculation of lattice distortion.

Table 5.2 Theoretical calculations and experimental results of lattice distortions. Effective lattice constant (d_i^{eff}) of each element, lattice constant ($\bar{d}$) of theoretically-calculated results in comparison to the experimental data. Note that the experimental results are calculated, based on the chemical composition, which is obtained from the lattice constants that are obtained through synchrotron XRD, neutron diffraction, and HRTEM image.

Parameters / Materials	d_{Nb}^{eff}	d_{Ta}^{eff}	d_{Ti}^{eff}	d_{V}^{eff}	d_{Zr}^{eff}	$\bar{d}_{Theo}$	$\bar{d}_{Sync}$	$\bar{d}_{Neut}$	$\bar{d}_{HRTEM}$
NbTaTiV	**2.8558**	**2.8578**	**2.5863**	**2.6193**	**-**	**2.7973**	**2.8052**	**2.7988**	**2.7825**
NbTaTiVZr	**2.8488**	**2.8508**	**2.8559**	**2.6087**	**3.1110**	**2.8551**	**2.8658**	**2.8633**	**2.8388**

Table 5.3 The average lattice distortions for NbTaTiV and NbTaTiVZr alloys which are obtained from theoretical calculations, synchrotron diffractions, neutron diffractions, HRTEM image, and STEM-HAADF images.

Parameters / Alloys	Average Lattice Distortion $\bar{\mu}^D$(Å)				
	Theoretical Calculations	**Synchrotron Diffractions**	**Neutron Diffractions**	**HRTEM**	**STEM-HAADF**
NbTaTiV	**0.1186**	**0.1190**	**0.1187**	**0.1199**	**0.1140**
NbTaTiVZr	**0.1832**	**0.1839**	**0.1837**	**0.1844**	**0.1546**

5.4.3 Visualization and Measurements of Average Lattice Distortion for NbTaTiV and NbTaTiVZr HEAs via HRTEM and STEM-HAADF Techniques

Based on the macro-scale measurements of values of mean-field lattice distortion, employing synchrotron and neutron diffractions, the locally distorted lattice was physically visualized and quantitatively assessed by TEM. Figure 5.7(a) and (d) show the HRTEM images and its corresponding fast-Fourier-Transformation (FFT) patterns [the inset in Figure 5.7(a) and (b)] of homogenized NbTaTiV and NbTaTiVZr HEAs, which were acquired along the [110] and [100] zone axis, respectively. As consistent with the results of phase and microstructure identification, there is no specific feature of locally formed secondary phase, besides FFT patterns are clearly indexed as a BCC solid-solution phase in both alloy systems. In order to verify the variation of atomic arrangements, leading to a locally distorted crystalline lattices, the nearest-neighbor interatomic distances were measured from high magnification HRTEM image as shown in Figure 5.7(c) and (d). It is found that the ranges of nearest-neighbor interatomic distances along [110] for NbTaTiV and NbTaTiVZr are 0.1833 Å and 0.3307 Å, respectively, indicating that addition of equi-atomic percentage Zr element efficiently induces the larger deviation of atomic displacements. The detailed measured nearest-neighbor interatomic distances through HRTEM images are listed in Figure 5.7(c) and (d).

The values of local lattice distortion ($\bar{u}^D$) for NbTaTiV and NbTaTiVZr HEAs have been calculated, substituting the lattice constant $\bar{d}$, which are obtained from FFT

patterns, into the Eq. 5.5. Note that the lattice constants of present two alloys are measured by averaging the inner diffraction spots, which is marked with the yellow rectangular in Figure 5.7(b) and (d) and the obtained lattice constants are 3.216 Å (NbTaTiV), and 3.278 Å (NbTaTiVZr), respectively. The calculated local lattice distortions, $\bar{u}^D$, are 0.1195 Å and 0.1844 Å, indicating considerably close to the theoretically- and experimentally (neutron/synchrotron diffractions)-determined values of average lattice distortion.

To accurately obtain the actual position of atoms in each atomic column, high angle annular dark field (HAADF) technique is adopted. Unlike the conventional TEM, which provides a coherent image with phase contrast, HAADF use a focused electron beam with small convergent angle and spot size for scanning the specimen and collecting the thermal diffuse electron to construct an intuitive image with actual atomic position. The visible atomic location for NbTaTiV and NbTaTiVZr were illustrated by HAADF techniques in Figure 5.7(e) and (f), showing the random atomic distribution in BCC structure, which can be distinguished by contrasts in both HEAs. To precisely measure the interatomic distances along certain [hkl] direction ([110] directions for both alloys), two-dimensional (2D) Gaussian fitting methods were implemented, describing exact positions of individual atoms, as shown in Figure 5.7(g) and (h). With measured interatomic distances (d_{hkl}^i) and average of d_{hkl}^i from 2D Gaussian fitting, the values of lattice distortion for present two HEAs were calculated by following equation, which is formulated from Eq. 5.5.

$$\bar{u}_{hkl}^{D} \equiv \sqrt{\sum_{i}^{n}(d_{hkl}^{i} - \bar{d}_{hkl})^{2}/n} \quad (5.7)$$

where, d_{hkl}^{i} is the atomic distance of *i*th pair along the [hkl] direction, as marked in Figure 5.7(f), and $\bar{d}_{hkl}$ is the average interatomic distances. The values of lattice distortion for NbTaTiV and NbTaTiVZr HEAs along the [110] direction calculated by Eq. 5.7, are 0.1140 Å and 0.1546 Å, respectively, which is in good agreement with other measurement approaches. Note that the top right and the bottom left atoms were neglected due to incomplete atoms affect the fitting. The detailed values of lattice distortions, which are calculated and measured by various ways are summarized in Table 5.3. From the consistent calculated/measured results above, it is clearly concluded that distorted lattices are not localized but uniformly distributed in both alloy systems. Hence, the solid-solution strengthening, which stems from the distorted lattices plays critical rules in significant improvement of yield strength after addition of Zr elements.

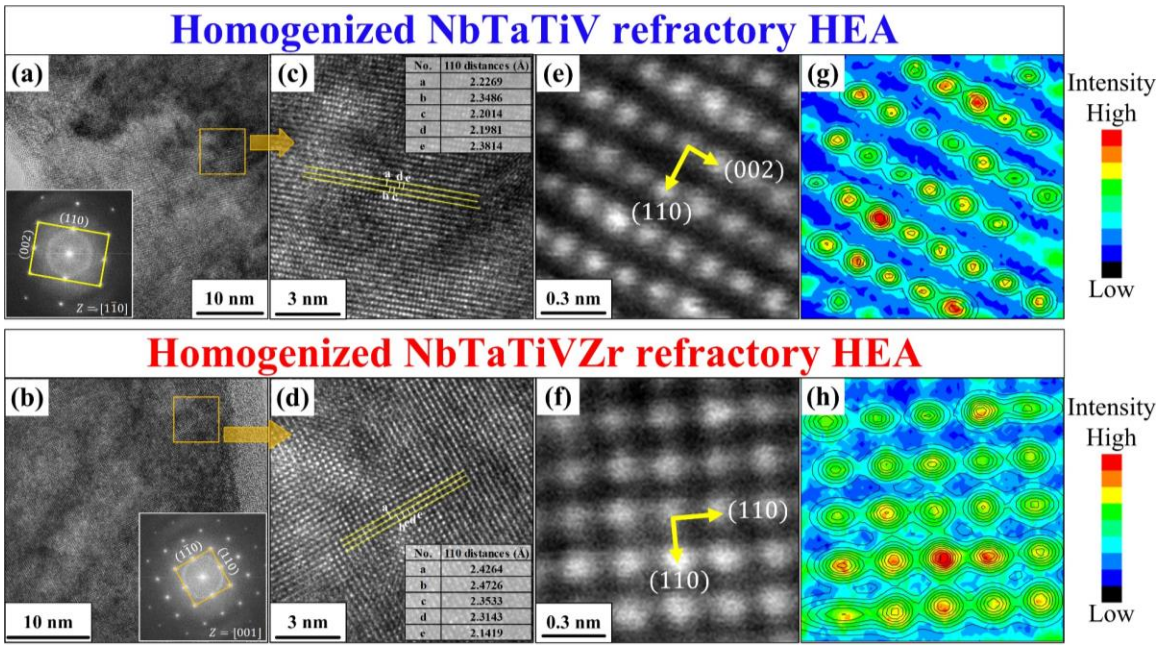

Figure 5.7 (a) (b) the HRTEM image and Fourier transformation of NbTaTiV and NbTaTiVZr alloys. It shows that NbTaTiV is of BCC structure and the lattice constant is 3.278 Å. (c) (d) the high magnitude HRTEM image for NbTaTiV and NbTaTiVZr, calculating the interatomic distances (e) (f) the HAADF images of NbTaTiV with $[1\bar{1}0]$ zone axis and NbTaTiVZr with $[001]$ zone axis. (g) (h) the 2D Gauss fitted images of (e) (f). It provides the atomic position on HAADF of NbTaTiV NbTaTiVZr alloys.

5.5 Conclusion

Overall, the Zr element is selected as an additional element in the NbTaTiV alloy to improve the lattice distortion. The NbTaTiVZr refractory HEA with a single BCC structure has been developed using integrated experimental and computational approaches. As predicted by CALPHAD simulation, a stable single BCC phase was achieved by the systematic thermal treatment. The NbTaTiV and NbTaTiVZr HEAs show similar trends of the phase formation and microstructures with different mechanical properties, which is mainly originated from the enhancement of lattice distortion. The distorted lattice was quantitatively calculated by theoretical calculations, synchrotron diffraction, TEM and STEM approaches. The calculated lattice distortions were in good agreement with the experimentally-measured results. The NbTaTiVZr HEA show higher lattice distortion than the NbTaTiV HEA, which plays a critical role in the improvement strength of the refractory HEAs.

CHAPTER SIX CONCLUSION

Overall, this comprehensive study provides a method of the design and development of the single-phase BCC solid-solution phase refractory HEA, using an integrated experimental and theoretical thermodynamic-calculation approach. The results of the APT measurement and the neutron-diffraction patterns indicate that the structure is composed of a single-phase BCC solid solution as well as a homogeneous elemental distribution with equimolar ratios. Furthermore, the mechanical-test results of the homogenization-treated sample show the excellent yield strength and plasticity at RT as well as elevated temperatures. The dominant strengthening mechanism was found to be solid-solution hardening, which stems from the distortion of the crystalline lattice during deformation. It is thought that this strengthening mechanism induces slow elemental diffusion at high temperatures, which, consequently, leads to the strong resistance of high-temperature softening. The distorted lattice for this alloy system was quantitatively calculated by the mathematical computation and theoretical modeling, such as first-principles calculations. The results of the above modeling and analysis indicate that the local severe lattice distortions are induced, due to the atomic-size mismatch and local atomic interactions in the homogenization-treated NbTaTiV refractory HEA.

Furthermore the unique elastic and plastic deformation behavior of the single BCC solid-solution phase refractory HEA at elevated temperatures, using in-situ neutron experiments coupled with theoretical calculations. The results of the microstructure and the neutron-diffraction patterns exhibit the excellent BCC single-phase stability

up to 900 °C. Furthermore, the present alloy possesses the high yield strength and excellent ductility at RT as well as softening resistance at elevated temperatures. The lattice-strain-evolution results show the distinctive elastic-deformation behavior as an elastic isotropy at RT, and the elastic isotropic-anisotropic transition appeared at about 700 °C.

The single-crystal elastic moduli are obtained from the in-situ neutron-diffraction data coupled with the Kroner model approach, showing the great agreement with first-principles calculations. Moreover, this alloy followed the criteria for the prediction of the ductility, such as the Cauchy pressure, Pugh ratio, and Poisson's ratio. The evolution of the dislocation density and verification of mobile dislocation type was quantitatively investigated by the Williamson-hall plot profile. The dislocation density during the 15 % plastic deformation is significantly decreased at high temperatures due to the strong structural-relaxation effects, and the dominant mobile dislocation can be edge dislocations. It is though that the severely-distorted lattice induces the deviation of the formation of dislocations from their neutral dislocation planes, which, consequently, leads to the significant difficulty of the movement of edge dislocations during plastic deformation. Thus, the edge dislocations can be the dominant dislocation type for the BCC refractory HEA, which is atypical, as compared to the conventional BCC metals and alloys.
Moreover, the Zr element is selected as an additional element in the NbTaTiV alloy to improve the lattice distortion. The NbTaTiVZr refractory HEA with a single BCC structure has been developed using integrated experimental and computational

approaches. As predicted by CALPHAD simulation, a stable single BCC phase was achieved by the systematic thermal treatment. The NbTaTiV and NbTaTiVZr HEAs show similar trends of the phase formation and microstructures with different mechanical properties, which is mainly originated from the enhancement of lattice distortion. The distorted lattice was quantitatively calculated by theoretical calculations, synchrotron diffraction, TEM and STEM approaches. The calculated lattice distortions were in good agreement with the experimentally-measured results. The NbTaTiVZr HEA show higher lattice distortion than the NbTaTiV HEA, which plays a critical role in the improvement strength of the refractory HEAs.

These new discoveries of the unique elastic and plastic deformation behaviors of the NbTaTiV refractory HEA may lead to the overall excellent mechanical performance and provide a road map to produce newly-designed polycrystalline materials for high-temperature applications.

LIST OF REFERENCES

[1] Z. Li, K.G. Pradeep, Y. Deng, D. Raabe, C.C. Tasan, Metastable high-entropy dual-phase alloys overcome the strength–ductility trade-off, Nature (2016).
[2] L.J. Santodonato, Y. Zhang, M. Feygenson, C.M. Parish, M.C. Gao, R.J. Weber, J.C. Neuefeind, Z. Tang, P.K. Liaw, Deviation from high-entropy configurations in the atomic distributions of a multi-principal-element alloy, Natuture Communications 6 (2015) 5964.
[3] Y. Zhang, Y.J. Zhou, J.P. Lin, G.L. Chen, P.K. Liaw, Solid-solution phase formation rules for multi-component alloys, Advanced Engineering Materials 10(6) (2008) 534-538.
[4] Y. Zhang, T.T. Zuo, Z. Tang, M.C. Gao, K.A. Dahmen, P.K. Liaw, Z.P. Lu, Microstructures and properties of high-entropy alloys, Progress in Materials Science 61 (2014) 1-93.
[5] B. Gludovatz, A. Hohenwarter, D. Catoor, E.H. Chang, E.P. George, R.O. Ritchie, A fracture-resistant high-entropy alloy for cryogenic applications, Science 345(6201) (2014) 1153-1158.
[6] F. Otto, Y. Yang, H. Bei, E.P. George, Relative effects of enthalpy and entropy on the phase stability of equiatomic high-entropy alloys, Acta Materialia 61(7) (2013) 2628-2638.
[7] O. Senkov, J. Miller, D. Miracle, C. Woodward, Accelerated exploration of multi-principal element alloys for structural applications, Calphad 50 (2015) 32-48.
[8] B. Cantor, I. Chang, P. Knight, A. Vincent, Microstructural development in equiatomic multicomponent alloys, Materials Science and Engineering: A 375 (2004) 213-218.
[9] O. Senkov, G. Wilks, D. Miracle, C. Chuang, P. Liaw, Refractory high-entropy alloys, Intermetallics 18(9) (2010) 1758-1765.
[10] O. Senkov, G. Wilks, J. Scott, D. Miracle, Mechanical properties of Nb 25 Mo 25 Ta 25 W 25 and V 20 Nb 20 Mo 20 Ta 20 W 20 refractory high entropy alloys, Intermetallics 19(5) (2011) 698-706.

[11] O. Senkov, J. Scott, S. Senkova, F. Meisenkothen, D. Miracle, C. Woodward, Microstructure and elevated temperature properties of a refractory TaNbHfZrTi alloy, Journal of Materials Science 47(9) (2012) 4062-4074.
[12] O. Senkov, J. Scott, S. Senkova, D. Miracle, C. Woodward, Microstructure and room temperature properties of a high-entropy TaNbHfZrTi alloy, Journal of alloys and compounds 509(20) (2011) 6043-6048.
[13] K.M. Youssef, A.J. Zaddach, C. Niu, D.L. Irving, C.C. Koch, A novel low-density, high-hardness, high-entropy alloy with close-packed single-phase nanocrystalline structures, Materials Research Letters 3(2) (2015) 95-99.
[14] M.C. Gao, B. Zhang, S. Guo, J. Qiao, J. Hawk, High-entropy alloys in hexagonal close-packed structure, Metallurgical and Materials Transactions A 47(7) (2016) 3322-3332.
[15] Z. Zhang, M. Mao, J. Wang, B. Gludovatz, Z. Zhang, S.X. Mao, E.P. George, Q. Yu, R.O. Ritchie, Nanoscale origins of the damage tolerance of the high-entropy alloy CrMnFeCoNi, Nature communications 6 (2015) 10143.
[16] B. Gludovatz, A. Hohenwarter, K.V. Thurston, H. Bei, Z. Wu, E.P. George, R.O. Ritchie, Exceptional damage-tolerance of a medium-entropy alloy CrCoNi at cryogenic temperatures, Nature communications 7 (2016) 10602.
[17] Y. Jo, S. Jung, W. Choi, S. Sohn, H. Kim, B. Lee, N. Kim, S. Lee, Cryogenic strength improvement by utilizing room-temperature deformation twinning in a partially recrystallized VCrMnFeCoNi high-entropy alloy, Nature Communications 8 (2017) ncomms15719.
[18] H. Huang, X. Li, Z. Dong, W. Li, S. Huang, D. Meng, X. Lai, T. Liu, S. Zhu, L. Vitos, Critical stress for twinning nucleation in CrCoNi-based medium and high entropy alloys, Acta Materialia 149 (2018) 388-396.
[19] L.-Y. Tian, G. Wang, J.S. Harris, D.L. Irving, J. Zhao, L. Vitos, Alloying effect on the elastic properties of refractory high-entropy alloys, Materials & Design 114 (2017) 243-252.

[20] H. Zhang, X. Sun, S. Lu, Z. Dong, X. Ding, Y. Wang, L. Vitos, Elastic properties of Al x CrMnFeCoNi (0≤ x≤ 5) high-entropy alloys from ab initio theory, Acta Materialia (2018).
[21] O. Senkov, S. Senkova, D. Miracle, C. Woodward, Mechanical properties of low-density, refractory multi-principal element alloys of the Cr–Nb–Ti–V–Zr system, Materials Science and Engineering: A 565 (2013) 51-62.
[22] O. Senkov, S. Senkova, C. Woodward, Effect of aluminum on the microstructure and properties of two refractory high-entropy alloys, Acta Materialia 68 (2014) 214-228.
[23] Y. Zou, H. Ma, R. Spolenak, Ultrastrong ductile and stable high-entropy alloys at small scales, Nature communications 6 (2015) 7748.
[24] J.-W. Yeh, S.-J. Lin, T.-S. Chin, J.-Y. Gan, S.-K. Chen, T.-T. Shun, C.-H. Tsau, S.-Y. Chou, Formation of simple crystal structures in Cu-Co-Ni-Cr-Al-Fe-Ti-V alloys with multiprincipal metallic elements, Metallurgical and Materials Transactions A 35(8) (2004) 2533-2536.
[25] W. Guo, W. Dmowski, J.-Y. Noh, P. Rack, P.K. Liaw, T. Egami, Local atomic structure of a high-entropy alloy: an x-ray and neutron scattering study, Metallurgical and Materials Transactions A 44(5) (2013) 1994-1997.
[26] J.-W. Yeh, S.-Y. Chang, Y.-D. Hong, S.-K. Chen, S.-J. Lin, Anomalous decrease in X-ray diffraction intensities of Cu–Ni–Al–Co–Cr–Fe–Si alloy systems with multi-principal elements, Materials chemistry and physics 103(1) (2007) 41-46.
[27] Y. Wu, Y. Cai, T. Wang, J. Si, J. Zhu, Y. Wang, X. Hui, A refractory Hf 25 Nb 25 Ti 25 Zr 25 high-entropy alloy with excellent structural stability and tensile properties, Materials Letters 130 (2014) 277-280.
[28] M. Yao, K. Pradeep, C. Tasan, D. Raabe, A novel, single phase, non-equiatomic FeMnNiCoCr high-entropy alloy with exceptional phase stability and tensile ductility, Scripta Materialia 72 (2014) 5-8.

[29] N. Stepanov, N.Y. Yurchenko, V. Sokolovsky, M. Tikhonovsky, G. Salishchev, An AlNbTiVZr 0.5 high-entropy alloy combining high specific strength and good ductility, Materials Letters 161 (2015) 136-139.
[30] N. Stepanov, N.Y. Yurchenko, D. Shaysultanov, G. Salishchev, M. Tikhonovsky, Effect of Al on structure and mechanical properties of AlxNbTiVZr (x= 0, 0.5, 1, 1.5) high entropy alloys, Materials Science and Technology 31(10) (2015) 1184-1193.
[31] S. Maiti, W. Steurer, Structural-disorder and its effect on mechanical properties in single-phase TaNbHfZr high-entropy alloy, Acta Materialia 106 (2016) 87-97.
[32] J.W. Yeh, S.K. Chen, S.J. Lin, J.Y. Gan, T.S. Chin, T.T. Shun, C.H. Tsau, S.Y. Chang, Nanostructured high-entropy alloys with multiple principal elements: novel alloy design concepts and outcomes, Advanced Engineering Materials 6(5) (2004) 299-303.
[33] Z. Tang, T. Yuan, C.-W. Tsai, J.-W. Yeh, C.D. Lundin, P.K. Liaw, Fatigue behavior of a wrought Al 0.5 CoCrCuFeNi two-phase high-entropy alloy, Acta Materialia 99 (2015) 247-258.
[34] M.A. Hemphill, T. Yuan, G. Wang, J. Yeh, C. Tsai, A. Chuang, P. Liaw, Fatigue behavior of Al 0.5 CoCrCuFeNi high entropy alloys, Acta Materialia 60(16) (2012) 5723-5734.
[35] C.-J. Tong, M.-R. Chen, J.-W. Yeh, S.-J. Lin, S.-K. Chen, T.-T. Shun, S.-Y. Chang, Mechanical performance of the Al x CoCrCuFeNi high-entropy alloy system with multiprincipal elements, Metallurgical and Materials Transactions A 36(5) (2005) 1263-1271.
[36] F. Otto, A. Dlouhý, C. Somsen, H. Bei, G. Eggeler, E.P. George, The influences of temperature and microstructure on the tensile properties of a CoCrFeMnNi high-entropy alloy, Acta Materialia 61(15) (2013) 5743-5755.
[37] L. Li, T. Ungar, Y. Wang, J.R. Morris, G. Tichy, J. Lendvai, Y. Yang, Y. Ren, H. Choo, P.K. Liaw, Microstructure evolution during cold rolling in a nanocrystalline

Ni–Fe alloy determined by synchrotron X-ray diffraction, Acta Materialia 57(17) (2009) 4988-5000.
[38] O. Senkov, C. Woodward, Microstructure and properties of a refractory NbCrMo0. 5Ta0. 5TiZr alloy, Materials Science and Engineering: A 529 (2011) 311-320.
[39] O. Senkov, J. Miller, D. Miracle, C. Woodward, Accelerated exploration of multi-principal element alloys with solid solution phases, Nature communications 6 (2015).
[40] M.C. Gao, D.E. Alman, Searching for next single-phase high-entropy alloy compositions, Entropy 15(10) (2013) 4504-4519.
[41] F. Zhang, C. Zhang, S. Chen, J. Zhu, W. Cao, U. Kattner, An understanding of high entropy alloys from phase diagram calculations, Calphad 45 (2014) 1-10.
[42] R. Feng, M.C. Gao, C. Lee, M. Mathes, T. Zuo, S. Chen, J.A. Hawk, Y. Zhang, P.K. Liaw, Design of light-weight high-entropy alloys, Entropy 18(9) (2016) 333.
[43] A. Zunger, S.-H. Wei, L. Ferreira, J.E. Bernard, Special quasirandom structures, Physical Review Letters 65(3) (1990) 353.
[44] B. Sundman, B. Jansson, J.-O. Andersson, The thermo-calc databank system, Calphad 9(2) (1985) 153-190.
[45] K. Thompson, D. Lawrence, D. Larson, J. Olson, T. Kelly, B. Gorman, In situ site-specific specimen preparation for atom probe tomography, Ultramicroscopy 107(2) (2007) 131-139.
[46] M.C. Gao, J.-W. Yeh, P.K. Liaw, Y. Zhang, High-entropy alloys: fundamentals and applications, Springer2016.
[47] C.A. Schneider, W.S. Rasband, K.W. Eliceiri, NIH Image to ImageJ: 25 years of image analysis, Nature methods 9(7) (2012) 671.
[48] D.J. Larson, T.J. Prosa, R.M. Ulfig, B.P. Geiser, T.F. Kelly, Local electrode atom probe tomography, New York, US: Springer Science (2013).
[49] K. An, H.D. Skorpenske, A.D. Stoica, D. Ma, X.-L. Wang, E. Cakmak, First in situ lattice strains measurements under load at VULCAN, Metallurgical and Materials Transactions A 42(1) (2011) 95-99.

[50] X.-L. Wang, T. Holden, G.Q. Rennich, A. Stoica, P.K. Liaw, H. Choo, C.R. Hubbard, VULCAN—The engineering diffractometer at the SNS, Physica B: Condensed Matter 385 (2006) 673-675.
[51] K. An, VDRIVE-Data reduction and interactive visualization software for event mode neutron diffraction, ORNL Report No. ORNL-TM-2012-621 Oak Ridge National Laboratory, Oak Ridge, TN (2012).
[52] G. Kresse, J. Furthmüller, Efficient iterative schemes for ab initio total-energy calculations using a plane-wave basis set, Physical review B 54(16) (1996) 11169.
[53] P.E. Blöchl, O. Jepsen, O.K. Andersen, Improved tetrahedron method for Brillouin-zone integrations, Physical Review B 49(23) (1994) 16223.
[54] G. Kresse, D. Joubert, From ultrasoft pseudopotentials to the projector augmented-wave method, Physical Review B 59(3) (1999) 1758.
[55] J.P. Perdew, K. Burke, M. Ernzerhof, Generalized gradient approximation made simple, Physical review letters 77(18) (1996) 3865.
[56] H.J. Monkhorst, J.D. Pack, Special points for Brillouin-zone integrations, Physical review B 13(12) (1976) 5188.
[57] M. Gao, C. Carney, Ö. Doğan, P. Jablonksi, J. Hawk, D. Alman, Design of refractory high-entropy alloys, JOM 67(11) (2015) 2653-2669.
[58] M.K. Miller, Atom probe tomography: analysis at the atomic level, Springer Science & Business Media2012.
[59] M.P. Moody, L.T. Stephenson, A.V. Ceguerra, S.P. Ringer, Quantitative binomial distribution analyses of nanoscale like-solute atom clustering and segregation in atom probe tomography data, Microscopy research and technique 71(7) (2008) 542-550.
[60] F. Otto, A. Dlouhý, K. Pradeep, M. Kuběnová, D. Raabe, G. Eggeler, E. George, Decomposition of the single-phase high-entropy alloy CrMnFeCoNi after prolonged anneals at intermediate temperatures, Acta Materialia 112 (2016) 40-52.

[61] S. Huang, D.W. Brown, B. Clausen, Z. Teng, Y. Gao, P.K. Liaw, In situ neutron-diffraction studies on the creep behavior of a ferritic superalloy, Metallurgical and Materials Transactions A 43(5) (2012) 1497-1508.
[62] T. Ungár, J. Gubicza, G. Ribárik, A. Borbély, Crystallite size distribution and dislocation structure determined by diffraction profile analysis: principles and practical application to cubic and hexagonal crystals, Journal of Applied Crystallography 34(3) (2001) 298-310.
[63] E. Francis, B. Grant, J.Q. da Fonseca, P. Phillips, M. Mills, M. Daymond, M. Preuss, High-temperature deformation mechanisms in a polycrystalline nickel-base superalloy studied by neutron diffraction and electron microscopy, Acta Materialia 74 (2014) 18-29.
[64] N. Guo, L. Wang, L. Luo, X. Li, R. Chen, Y. Su, J. Guo, H. Fu, Effect of composing element on microstructure and mechanical properties in Mo–Nb–Hf–Zr–Ti multi-principle component alloys, Intermetallics 69 (2016) 13-20.
[65] A. Larson, R. Von Dreele, GSAS General Structure Analysis System, LANSCE, MS-H805, Los Alamos: Los Alamos National Laboratory (1998).
[66] D. Miracle, O. Senkov, A critical review of high entropy alloys and related concepts, Acta Materialia 122 (2017) 448-511.
[67] R. Labusch, A statistical theory of solid solution hardening, physica status solidi (b) 41(2) (1970) 659-669.
[68] Y. Ye, C. Liu, Y. Yang, A geometric model for intrinsic residual strain and phase stability in high entropy alloys, Acta Materialia 94 (2015) 152-161.
[69] G. Sheng, C.T. Liu, Phase stability in high entropy alloys: formation of solid-solution phase or amorphous phase, Progress in Natural Science: Materials International 21(6) (2011) 433-446.
[70] Y. Zhang, X. Yang, P. Liaw, Alloy design and properties optimization of high-entropy alloys, Jom 64(7) (2012) 830-838.
[71] I. Toda-Caraballo, P.E. Rivera-Díaz-del-Castillo, Modelling solid solution hardening in high entropy alloys, Acta Materialia 85 (2015) 14-23.

[72] R. Fleischer, Substitutional solution hardening, Acta metallurgica 11(3) (1963) 203-209.
[73] L. Gypen, A. Deruyttere, Multi-component solid solution hardening, Journal of Materials Science 12(5) (1977) 1028-1033.
[74] H. Yao, J. Qiao, J. Hawk, H. Zhou, M. Chen, M. Gao, Mechanical properties of refractory high-entropy alloys: Experiments and modeling, Journal of Alloys and Compounds 696 (2017) 1139-1150.
[75] R. Arsenault, Treatise on materials science and technology. Volume VI. Plastic deformation of materials, (1975).
[76] A. Van de Walle, P. Tiwary, M. De Jong, D. Olmsted, M. Asta, A. Dick, D. Shin, Y. Wang, L.-Q. Chen, Z.-K. Liu, Efficient stochastic generation of special quasirandom structures, Calphad 42 (2013) 13-18.
[77] S. Zherebtsov, G. Salishchev, R. Galeyev, K. Maekawa, Mechanical properties of Ti–6Al–4V titanium alloy with submicrocrystalline structure produced by severe plastic deformation, Materials Transactions 46(9) (2005) 2020-2025.
[78] K.-Y. Tsai, M.-H. Tsai, J.-W. Yeh, Sluggish diffusion in Co–Cr–Fe–Mn–Ni high-entropy alloys, Acta Materialia 61(13) (2013) 4887-4897.
[79] M.C. Troparevsky, J.R. Morris, P.R. Kent, A.R. Lupini, G.M. Stocks, Criteria for predicting the formation of single-phase high-entropy alloys, Physical Review X 5(1) (2015) 011041.
[80] C.L. Tracy, S. Park, D.R. Rittman, S.J. Zinkle, H. Bei, M. Lang, R.C. Ewing, W.L. Mao, High pressure synthesis of a hexagonal close-packed phase of the high-entropy alloy CrMnFeCoNi, Nature Communications 8 (2017).
[81] Y. Zhou, Y. Zhang, F. Wang, G. Chen, Phase transformation induced by lattice distortion in multiprincipal component Co Cr Fe Ni Cu x Al 1− x solid-solution alloys, Applied Physics Letters 92(24) (2008) 241917.
[82] C. Lee, G. Song, M.C. Gao, R. Feng, P. Chen, J. Brechtl, Y. Chen, K. An, W. Guo, J.D. Poplawsky, Lattice Distortion in a Strong and Ductile Refractory High-entropy Alloy, Acta Materialia (2018).

[83] L.R. Owen, N.G. Jones, Lattice distortions in high-entropy alloys, Journal of Materials Research 33(19) (2018) 2954-2969.
[84] F. Tian, L.K. Varga, N. Chen, J. Shen, L. Vitos, Ab initio design of elastically isotropic TiZrNbMoVx high-entropy alloys, Journal of Alloys and Compounds 599 (2014) 19-25.
[85] F. Tian, L.K. Varga, N. Chen, J. Shen, L. Vitos, Empirical design of single phase high-entropy alloys with high hardness, Intermetallics 58 (2015) 1-6.
[86] S. Guo, C. Ng, J. Lu, C. Liu, Effect of valence electron concentration on stability of fcc or bcc phase in high entropy alloys, Journal of applied physics 109(10) (2011) 103505.
[87] (!!! INVALID CITATION !!! []).
[88] S. Pugh, XCII. Relations between the elastic moduli and the plastic properties of polycrystalline pure metals, The London, Edinburgh, and Dublin Philosophical Magazine and Journal of Science 45(367) (1954) 823-843.
[89] D.G. Pettifor, Theoretical predictions of structure and related properties of intermetallics, Materials Science and Technology 8(4) (1992) 345-349.
[90] X. Gu, A. McDermott, S.J. Poon, G.J. Shiflet, Critical Poisson's ratio for plasticity in Fe–Mo–C–B–Ln bulk amorphous steel, Applied Physics Letters 88(21) (2006) 211905.
[91] H. Niu, X.-Q. Chen, P. Liu, W. Xing, X. Cheng, D. Li, Y. Li, Extra-electron induced covalent strengthening and generalization of intrinsic ductile-to-brittle criterion, Scientific reports 2 (2012) 718.
[92] M. Daymond, H. Priesmeyer, Elastoplastic deformation of ferritic steel and cementite studied by neutron diffraction and self-consistent modelling, Acta materialia 50(6) (2002) 1613-1626.
[93] T. Ungár, I. Dragomir, Á. Révész, A. Borbély, The contrast factors of dislocations in cubic crystals: the dislocation model of strain anisotropy in practice, Journal of applied crystallography 32(5) (1999) 992-1002.
[94] B. Warren, BE Warren and BL Averbach, J. Appl. Phys. 21, 595 (1950), J. Appl. Phys. 21 (1950) 595.

[95] G. Williamson, W. Hall, X-ray line broadening from filed aluminium and wolfram, Acta metallurgica 1(1) (1953) 22-31.
[96] G. Kresse, J. Furthmüller, Efficiency of ab-initio total energy calculations for metals and semiconductors using a plane-wave basis set, Computational Materials Science 6(1) (1996) 15-50.
[97] P.E. Blöchl, Projector augmented-wave method, Physical review B 50(24) (1994) 17953.
[98] M. De Jong, W. Chen, T. Angsten, A. Jain, R. Notestine, A. Gamst, M. Sluiter, C.K. Ande, S. Van Der Zwaag, J.J. Plata, Charting the complete elastic properties of inorganic crystalline compounds, Scientific data 2 (2015) 150009.
[99] F. Tasnádi, M. Odén, I.A. Abrikosov, Ab initio elastic tensor of cubic Ti 0.5 Al 0.5 N alloys: dependence of elastic constants on size and shape of the supercell model and their convergence, Physical Review B 85(14) (2012) 144112.
[100] J.H. Hollomon, Tensile deformation, Aime Trans 12(4) (1945) 1-22.
[101] Y. Tomota, P. Lukas, S. Harjo, J. Park, N. Tsuchida, D. Neov, In situ neutron diffraction study of IF and ultra low carbon steels upon tensile deformation, Acta materialia 51(3) (2003) 819-830.
[102] E. Kröner, Berechnung der elastischen Konstanten des Vielkristalls aus den Konstanten des Einkristalls, Zeitschrift für Physik 151(4) (1958) 504-518.
[103] E. KRÖNER, Statistical Modeling, w" Modeling Small Deformations of Polycrystal", chap. 8, J. GITTUS, J. ZARKA ed, Elsevier Appl Sci. Publ., London, 1986.
[104] R. De Wit, Diffraction elastic constants of a cubic polycrystal, Journal of applied crystallography 30(4) (1997) 510-511.
[105] T. GnaÈupel-Herold, P.C. Brand, H.J. Prask, Calculation of single-crystal elastic constants for cubic crystal symmetry from powder diffraction data, Journal of applied crystallography 31(6) (1998) 929-935.
[106] A. Haglund, M. Koehler, D. Catoor, E.P. George, V. Keppens, Polycrystalline elastic moduli of a high-entropy alloy at cryogenic temperatures, intermetallics 58 (2015) 62-64.

[107] G. Laplanche, P. Gadaud, O. Horst, F. Otto, G. Eggeler, E. George, Temperature dependencies of the elastic moduli and thermal expansion coefficient of an equiatomic, single-phase CoCrFeMnNi high-entropy alloy, Journal of Alloys and Compounds 623(25) (2015) 348-353.
[108] D. Iotova, N. Kioussis, S.P. Lim, Electronic structure and elastic properties of the Ni 3 X (X= Mn, Al, Ga, Si, Ge) intermetallics, Physical Review B 54(20) (1996) 14413.
[109] A. Marmier, Z.A. Lethbridge, R.I. Walton, C.W. Smith, S.C. Parker, K.E. Evans, ElAM: A computer program for the analysis and representation of anisotropic elastic properties, Computer Physics Communications 181(12) (2010) 2102-2115.
[110] R. Gaillac, P. Pullumbi, F.-X. Coudert, ELATE: an open-source online application for analysis and visualization of elastic tensors, Journal of Physics: Condensed Matter 28(27) (2016) 275201.
[111] S.I. Ranganathan, M. Ostoja-Starzewski, Universal elastic anisotropy index, Physical Review Letters 101(5) (2008) 055504.
[112] W. Woo, E.-W. Huang, J.-W. Yeh, H. Choo, C. Lee, S.-Y. Tu, In-situ neutron diffraction studies on high-temperature deformation behavior in a CoCrFeMnNi high entropy alloy, Intermetallics 62 (2015) 1-6.
[113] Y. Wei, A.F. Bower, H. Gao, Recoverable creep deformation due to heterogeneous grain-boundary diffusion and sliding, Scripta Materialia 57(10) (2007) 933-936.
[114] Y. Wei, A.F. Bower, H. Gao, Enhanced strain-rate sensitivity in fcc nanocrystals due to grain-boundary diffusion and sliding, Acta Materialia 56(8) (2008) 1741-1752.
[115] Z. Wang, A.D. Stoica, D. Ma, A.M. Beese, Diffraction and single-crystal elastic constants of Inconel 625 at room and elevated temperatures determined by neutron diffraction, Materials Science and Engineering: A 674 (2016) 406-412.
[116] D. Chung, W. Buessem, The elastic anisotropy of crystals, Journal of Applied Physics 38(5) (1967) 2010-2012.

[117] J. Hutchinson, Elastic-plastic behaviour of polycrystalline metals and composites, Proc. R. Soc. Lond. A 319(1537) (1970) 247-272.
[118] M. Daymond, M. Bourke, R. Von Dreele, B. Clausen, T. Lorentzen, Use of Rietveld refinement for elastic macrostrain determination and for evaluation of plastic strain history from diffraction spectra, Journal of Applied Physics 82(4) (1997) 1554-1562.
[119] G. Stoica, A. Stoica, M. Miller, D. Ma, Temperature-dependent elastic anisotropy and mesoscale deformation in a nanostructured ferritic alloy, Nature communications 5 (2014) 5178.
[120] Y. Wu, W. Liu, X. Wang, D. Ma, A.D. Stoica, T. Nieh, Z. He, Z. Lu, In-situ neutron diffraction study of deformation behavior of a multi-component high-entropy alloy, Applied Physics Letters 104(5) (2014) 051910.
[121] E. Oliver, M. Daymond, P. Withers, Interphase and intergranular stress generation in carbon steels, Acta Materialia 52(7) (2004) 1937-1951.
[122] L. Vitos, The EMTO method and applications in computational quantum mechanics for materials engineers, Springer-Verlag, London) Gyorffy BL, Stocks GM (1983) Concentration waves and fermi surfaces in random metallic alloys. Phys Rev Lett 50(5) (2007) 374-377.
[123] A. Sumer, J. Smith, A Comparison of the Elastic Constants of Chromium as Determined from Diffuse X-Ray and Ultrasonic Techniques, Journal of Applied Physics 34(9) (1963) 2691-2694.
[124] G. Simmons, Single crystal elastic constants and calculated aggregate properties, SOUTHERN METHODIST UNIV DALLAS TEX, 1965.
[125] D.E. Gray, H. Wise, American institute of physics handbook, Physics Today 10 (1957) 36.
[126] G.E. Dieter, Elements of the theory of plasticity, Mechanical metallurgy (1988) 76-79.
[127] T. Li, J. Morris Jr, N. Nagasako, S. Kuramoto, D. Chrzan, “Ideal” engineering alloys, Physical review letters 98(10) (2007) 105503.

[128] T. Gniiupel-HeroldlJ, P.C. Brand, H.J. Prask, Accessing the elastic properties of cubic materials with diffraction methods, (1998).
[129] M. Born, K. Huang, Dynamical theory of crystal lattices, Clarendon press1954.
[130] G. Alers, J. Neighbours, Crystal stability and elastic constants, Journal of Applied Physics 28(12) (1957) 1514-1514.
[131] K. Gschneidner Jr, A. Russell, A. Pecharsky, J. Morris, Z. Zhang, T. Lograsso, D. Hsu, C.C. Lo, Y. Ye, A. Slager, A family of ductile intermetallic compounds, Nature Materials 2(9) (2003) 587.
[132] J. Schroers, W.L. Johnson, Ductile bulk metallic glass, Physical Review Letters 93(25) (2004) 255506.
[133] R. Barabash, G. Ice, F. Walker, Quantitative microdiffraction from deformed crystals with unpaired dislocations and dislocation walls, Journal of applied physics 93(3) (2003) 1457-1464.
[134] X.-L. Wang, Y. Wang, A. Stoica, D. Horton, H. Tian, P. Liaw, H. Choo, J. Richardson, E. Maxey, Inter-and intragranular stresses in cyclically-deformed 316 stainless steel, Materials Science and Engineering: A 399(1-2) (2005) 114-119.
[135] T. Ungár, A. Borbély, The effect of dislocation contrast on x-ray line broadening: A new approach to line profile analysis, Applied Physics Letters 69(21) (1996) 3173-3175.
[136] G. Ribárik, T. Ungár, J. Gubicza, MWP-fit: a program for multiple whole-profile fitting of diffraction peak profiles by ab initio theoretical functions, Journal of Applied Crystallography 34(5) (2001) 669-676.
[137] A. Borbély, J. Dragomir-Cernatescu, G. Ribárik, T. Ungár, Computer program ANIZC for the calculation of diffraction contrast factors of dislocations in elastically anisotropic cubic, hexagonal and trigonal crystals, Journal of applied crystallography 36(1) (2003) 160-162.
[138] G. Dirras, J. Gubicza, A. Heczel, L. Lilensten, J.-P. Couzinié, L. Perrière, I. Guillot, A. Hocini, Microstructural investigation of plastically deformed

Ti20Zr20Hf20Nb20Ta20 high entropy alloy by X-ray diffraction and transmission electron microscopy, Materials Characterization 108 (2015) 1-7.
[139] J. Gubicza, N. Nam, L. Balogh, R. Hellmig, V. Stolyarov, Y. Estrin, T. Ungár, Microstructure of severely deformed metals determined by X-ray peak profile analysis, Journal of alloys and compounds 378(1-2) (2004) 248-252.
[140] D. Caillard, Kinetics of dislocations in pure Fe. Part I. In situ straining experiments at room temperature, Acta Materialia 58(9) (2010) 3493-3503.
[141] S. Rao, C. Varvenne, C. Woodward, T. Parthasarathy, D. Miracle, O. Senkov, W. Curtin, Atomistic simulations of dislocations in a model BCC multicomponent concentrated solid solution alloy, Acta Materialia 125 (2017) 311-320.
[142] W. Woo, T. Ungár, Z. Feng, E. Kenik, B. Clausen, X-ray and neutron diffraction measurements of dislocation density and subgrain size in a friction-stir-welded aluminum alloy, Metallurgical and Materials Transactions A 41(5) (2010) 1210-1216.
[143] E. Scheil, Comments on the layer crystal formation, Z. Metallkd 34 (1942) 70-72.
[144] G. Gulliver, The quantitative effect of rapid cooling upon the constitution of binary alloys, J. Inst. Met 9(1) (1913) 120-157.
[145] H. Yao, J. Qiao, M. Gao, J. Hawk, S. Ma, H. Zhou, Y. Zhang, NbTaV-(Ti, W) refractory high-entropy alloys: Experiments and modeling, Materials Science and Engineering: A 674 (2016) 203-211.
[146] M.G. Poletti, G. Fiore, B.A. Szost, L. Battezzati, Search for high entropy alloys in the X-NbTaTiZr systems (X= Al, Cr, V, Sn), Journal of Alloys and Compounds 620 (2015) 283-288.
[147] B. Zhang, M. Gao, Y. Zhang, S. Yang, S. Guo, Senary refractory high entropy alloy MoNbTaTiVW, Materials Science and Technology 31(10) (2015) 1207-1213.
[148] M. Gao, B. Zhang, S. Yang, S. Guo, Senary refractory high-entropy alloy HfNbTaTiVZr, Metallurgical and Materials Transactions A (2016) 1-13.

[149] C.-C. Juan, K.-K. Tseng, W.-L. Hsu, M.-H. Tsai, C.-W. Tsai, C.-M. Lin, S.-K. Chen, S.-J. Lin, J.-W. Yeh, Solution strengthening of ductile refractory HfMo x NbTaTiZr high-entropy alloys, Materials Letters 175 (2016) 284-287.

[150] A. Larson, R. Von Dreele, Generalized structure analysis system (GSAS), Los Alamos National Laborator Report LAUR

(1994) 86-748.

[151] A. Marshal, K. Pradeep, D. Music, S. Zaefferer, P. De, J. Schneider, Combinatorial synthesis of high entropy alloys: Introduction of a novel, single phase, body-centered-cubic FeMnCoCrAl solid solution, Journal of Alloys and Compounds 691 (2017) 683-689.

VITA

Chanho Lee was born in the city of Seoul, Korea, on September 12, 1984. He graduated with a Bachelor and Master degree from the Department of Materials Science and Engineering at Sejong University, Seoul in 2011 and 2013. He subsequently joined the Department of Materials Science and Engineering at The University of Tennessee, Knoxville for his Ph.D. track on August 2014. In August 2020, he graduated from the University of Tennessee, Knoxville with Doctor of Philosophy degree in Materials Science & Engineering.